School of Physics, University of the Witwatersrand

A First Principles Study of Structural stabilities and Electronic, Optical and Photocatalytic properties of Seleno-Germanates A_2GeSe_4 (A = Mg, Ca, γ-Sr and Ba) compounds.

Abdu Barde
1260593@students.wits.ac.za

Supervisor Professor Daniel P. Joubert
daniel.joubert2@wits.ac.za

A thesis submitted for the degree of Doctor of Philosophy (PhD) at the School of Physics.

Johannesburg, 2020

Declaration

I, the undersigned, hereby declare that the work contained in this PhD thesis is my original work, and that any work done by others or by myself previously has been acknowledged and referenced accordingly. This thesis is submitted to the University of the Witwatersrand, Johannesburg, in fulfillment of the requirements for the degree of Doctor of Philosophy (PhD) at the School of Physics. It has not been submitted before for any degree or examination in any other university.

Abdu Barde, 03 February 2020

Abstract

In this work, we systematically investigated the structural, mechanical, dynamic, electronic, optical and photocatalytic properties of A_2GeSe_4 (A = Mg, Ca, γ-Sr and Ba) seleno-germanate compounds by density functional calculations. Synthesis of Mg_2GeSe_4, γ-Sr_2GeSe_4 and Ba_2GeSe_4 have been reported, while Ca_2GeSe_4 is a hypothetical compound. Good structural chemistry and physical properties of seleno-germanates compounds have been reported, their tetrahedral $GeSe_4$ and polyhedral A_2Se_n coordinations (A = Alkaline earth metals; $n = 6$ - 9 fold coordination) have a significant role in shaping their physical properties.

Density functional theory (DFT) and many-body perturbation theory (MBPT) were used in our theoretical calculation of structural, mechanical, dynamic, electronic, optical and photocatalytic properties. The ground-state properties i.e. equilibrium volume, lattice constants, cohesive and formation energies and bulk moduli were calculated. Our calculated lattice parameters and equilibrium volumes are in reasonable agreement with available experimental data. Elastic constants satisfy the Born stability criteria, confirming mechanical stability of all four compounds and the calculated cohesive and formation energies also confirm that Ca_2GeSe_4 can be formed. Vibrational properties, studied using a finite displacement method, revealed no negative phonon frequencies across the Brillouin zone and therefore the compounds are dynamically stable. Hybrid functional and many-body perturbation theory was employed for the study of the electronic band structure and optical properties. Band structure results suggest that Mg_2GeSe_4 and Ca_2GeSe_2 are indirect band gap whereas γ-Sr_2GeSe_4 and Ba_2GeSe_4 are direct band gap semiconductor respectively. For the study of optical spectra, Bethe-Salpeter equation (BSE) was solved to include excitonic effect for an accurate descrip-

tion of optical properties. Optical absorption spectra show significant optical anisotropy. Band gaps estimated from BSE onset absorption spectra are 2.58, 2.30, 2.86 and 2.05 eV for Mg_2GeSe_4, Ca_2GeSe_4, γ-Sr_2GeSe_4 and Ba_2GeSe_4 respectively. The calculated band gaps suggests that Mg_2GeSe_4, Ca_2GeSe_4, γ-Sr_2GeSe_4 and Ba_2GeSe_4 are semiconductors with potential to absorb light in the ultra-violet and upper visible regions and are suitable for applications as non-linear optics, photovoltaic (multi-junction solar cell) and photocatalytic materials.

Surface energy and electronic properties of 100, 101, 110 and 111 periodic supercell surfaces of A_2GeSe_4 is calculated using the Generalized Gradient Approximation (GGA) the PBEsol, based on the calculated surface energies; a Wulff plot is constructed to analyzed the surface stability. From surface energy calculations and Wulff plot, Mg_2GeSe_4(101) and (110), Ca_2GeSe_4(100), γ-Sr_2GeSe_4(111) and Ba_2GeSe_4(111) surfaces are identified as the most stable surfaces. Surface charge density distribution analysis using Bader charge analysis reveals the presence of charge accumulation at isosurface of A_2GeSe_2. This change is likely to decrease charge recombination, facilitate easy charge transfer to adsorbate and enhance photocatalytic activities. Comparison of total and projected density of states (TPDOS) from the electronic structure of surface and crystal bulk reveal additional electronic surface state near the valence band and reduced band gap in surface structure with shifting of conduction band minimum towards the valence band maximum. Band edge positions, the valence band maximum (E_{VBM}) and conduction band minimum (E_{CBM}) are calculated on the most stable surface using band gap center (BGC) technique from periodic supercell GGA framework and crystal bulk quasiparticle G_0W_0+BSE band gap. Our calculated E_{VBM} and E_{CBM} for Mg_2GeSe_4(101) and (110), Ca_2GeSe_4(100), γ-Sr_2GeSe_4(111) and Ba_2GeSe_4(111) are -6.017, -6.480, -5.794, -6.009, -4.736 and -3.437, -3.90, -3.824, -3.149 and -2.689 eV respectively. Band edge positions in comparison to redox potential both at pH = 0 and 7 show that A_2GeSe_4 (A = Mg, Ca and γ-Sr) thermodynamically have the ability to photocatalytically oxidise and reduce water while Ba_2GeSe_4 is capable of photocatalytically reduction of water.

The absolute Mulliken's electronegativity, the so-called EN-model analysis of E_{VBM} and E_{CBM} compared to redox potential of water versus the normal hydrogen electrode (NHE) shows that the A_2GeSe_4 (A = Mg, Ca, γ-Sr and Ba) compound can straddle redox potential of water at pH = 7. Finally, the calculated ground-state properties, electronic and optical properties, the E_{VBM} and E_{CBM} positions in comparison to re-

dox potentials of water revealed that A_2GeSe_4 (A = Mg, Ca, γ-Sr and Ba) are stable compounds and suitable candidates that can be exploited for applications in non-linear optics, photovoltaic (multi-junction solar cells) and visible response photocatalytic materials.

Publications

1. Abdu Barde and Daniel P. Joubert. Investigation of structural, mechanical, dynamic, electronic and optical properties of seleno-germanates A_2GeSe_4 (A=Mg, Ca and γ-Sr) from first principles. *Materials Today Communications*, 22 (2020) 100785. Ref. [1].

2. Abdu Barde and Daniel P. Joubert. First principles investigation of structural, elastic, electronic and optical properties of Barium seleno-germanate, Ba_2GeSe_4. In South African Institute of Physics 63rd Annual Conference (SAIP 2018), edited by Prof. Japie Engelbrecht, pp. 14 - 19. ISBN: 978-0-620-85406-1, Proceedings of SAIP2018. Available online at http://events.saip.org.za/getFile.py/access?resId=53&materialId=3&confId=100.

3. Abdu Barde and Daniel P. Joubert. Structural, electronic and optical properties of rare-earth copper chalcogenides LaCuX2 (X = S, Se): A first principles study poster presentation. *Under review*.

Presentations and Workshops

1. 3 - 8 July 2017 CHPC HPC winter school, High Performance Computing School 2017. Hosted by Stellenbosch University (SU) and the Centre for High Performance Computing (CHPC) of the Council for Scientific and Industrial Research (CSIR) and funded by the Department of Science and Technology (DST), **South Africa**.

2. 25 - 29 June 2018, 63^{rd} Annual Conference of the South African Institute of physics (SAIP2018), University of Free state, Bloemfontein, **South Africa**. First principles investigation of structural, dynamic, electronic and optical properties of Barium seleno-germanate Ba_2GeSe_4 poster presentation.

3. 10 -20 June 2019, South Africa School of Elecronic Structure Method and Application Winter School (SASESMA 2019), University of Pretoria, **South Africa**.

4. 8 - 12 July 2019, 64^{th} Annual Conference of the South African Institute of physics (SAIP2019), University of Venda, host at the Protea Ranch Hotel, Polokwane, **South Africa**. Structural, electronic and optical properties of rare-earth copper chalcogenides LaCuX2 (X = S, Se): A first principles study poster presentation.

DEDICATION

I would like to deducate this work to the soul of my beloved late parents, my wives and children.

ACKNOWLEDGEMENTS

All thanks be Allah the most high, beneficient and merciful, peace be upon his messenger. I would like to extend my profound gratitude to my supervisor Daniel P. Joubert for his assitance and guidance throughout the period of this work.

I woud also like to thanks the group members for their support and guidance at all the time.

I would like to appreciate the patience, perseverance and support shown by my wives, children and family members throughout the period of this study.

The funding support of Tertiary Education Trust Fund (TETfund), Nigeria and Jigawa state polytechnic, Dutse, Nigeria is hereby acknowledged.

The Centre for High Performance Computing (CHPC), Cape Town (South Africa) is acknowledged for providing computational resources.

LIST OF ABBREVIATIONS

AFLOW - Automatic Flow

A^u - Universal Anisotropy

B - Bulk Modulus

BGC - Band Gap Center

β - Beta

CB - Conduction Band

CBM - Conduction Band Minimun

CN - Coordination Unit

CN7 - Sevenfold Coordination units

CN8 - Eightfold Coordination units

CN9 - Ninefold Coordination units

DFT - Density Functional Theory

2D - Two Dimensional

E - Young Modulus

E_{coh} - Cohesive Energy

E_{form} - Formation Energy

E_g - Energy Band Gap

EN - Electronegetivity model

E_{CBM} - Absolute conduction Band Edge

E_{VBM} - Absolute valence Band Edge

EOS - Equation of State

G - Shear Modulus

GGA - Generalized Gradient Approximation

ΔG^0 - Gibb's Free Energy

GSR-2019 - Global Status Report (2019)

HF - Hartree-Fock

HK - Hohenberg-Kohn

HSE - Heyd-Scuseria-Ernzerhof

IUPAC - International Union of Pure and Applied Chemistry

$K_C T$ - Rate of Charge Transfer

K_R - Electron-hole Recombination

KS - Kohn-Sham

LDA - Local Density Approximation

LSD - Local Spin Density

LSDA - Local Spin Density Approximation

MBJ - Modified Becker Johnson potential

MBPT - Many Body Perturbation Theory

MCS - Multinary Chalcogenides

$n(\mathbf{r})$ - Electronic Density

NBANDS - Number of Bands

NHE - Normal Hydrogen Electrode

NLO - Non-linear Optics

N_b - Number of atoms in a Bulk structure

N_s - Number of atoms in a supercell surface structure

PAW - Projected-Augmented Waves

PEC - Photoelectro Chemical

PBE - Perdew-Burke-Ernzerhof

PBEsol - Revised Perdew-Burke-Ernzerhof

PDOS - Projected/Partial Density of State

PVT - Pressure Volume Temperature

RPA - Random Phase Approximation

RTPSS - Revised-Tao-Perdew-Staroverov-Scuseria

SHE - Standard Hydrogen Electrode

TFD - Thomas-Fermi-Dirac

TDOS - Total Density of States

TPDOS - Total Projected/Partial Density of States

TPSS - Tao-Perdew-Staroverov-Scuseria

US PP - Ultra-soft Vanderbilt Pseudopotentials

VASP - Vienna *ab initio* Simulation Package

VB - Valence Band

VBM - Valence Band Maximum

VRH - Voight-Reuss-Hill

ω (eV) - Photon energy

ω_p - Plasma Resonance Frequency

χ - Electronegetivity

γ - Gamma

Contents

List of Figures

List of Tables

1

Introduction

1.1 Motivations and Overview

The need for a search of alternative, renewable, cheap, safe and environmentally friendly energy sources for the realization of a green and sustainable society and for the improvement of social and economic development is a concern of the 21^{st}-century scientific community. There are several examples of alternative energy materials and green technology that can be used to achieve the green, sustainable and economically viable society from natural resources such as wind, solar power, fuel cell, biomass, hydro power etc. [2]. In comparison to the traditional carbon-based energy, according to Murdock et al. [3] in the renewable Global Status Report 2019 (GSR2019). They reported that renewable source of energy account only for 26.2% of global energy consumptions in the year 2018. This is expected to reach 45% by the year 2040, expecting most likely increase from solar, wind and hydropower. Therefore, there is a call for accelerated research in this direction. For the solar renewable sources the photovoltaic, photoelectrochemical and photocatalysis have from their initial stage similar energy conversion mechanism. These mechanism involves photon absorption by semiconducting materials and converted them to photo excited charge carriers that are transported and utilized to produce electrical power or chemical fuel [4]. But some of the solar renewable systems like photovoltaic systems are characterised with the diurnal cycle, intermittency of terrestrial solar resource and cost effective storage system [5]. It is argued that the most attractive and easy solar energy conversion and storage is in the form of a chemical bond, by producing

the cheap solar fuel, from the photoelectro chemical (PEC) and photocatalytic process [5, 6].

Photocatalysis is a potential means of renewable energy production from water splitting to produce hydrogen fuel to replace fossil fuel and reduce carbon dioxide emission. There are two approaches to a successful photocatalytic water splitting, the one-step and two-step water splitting [7]. In the one-step process, where the overall water splitting is achieved with a single semiconductor photocatalyst. These semiconductors must satisfy the conditions of sufficient vacuum potential, thermodynamic potential and suitable band gap to harvest visible-light and stability to photo corrosion [7, 8]. These conditions limit the number of the reliable and reproducible semiconductor one-step water splitting compounds. The two-step approach is a photocatalytic process that is achieved with combination of two semiconductors. In this process a semiconductor with only capable reduction potential is combined with another semiconductor with oxidation potential to achieve overall water splitting. The two-step approach is usually called the Z-Scheme or heterojunction. Its advantage is that it greatly improves the light absorption and charge transfer. With Z-Scheme approach many successful visible-light photocatalysts were reported [9, 10, 11].

Since the 1972 pioneering discovery work of photoelectrochemical water splitting on a TiO_2 photoanode [12], a large number of semiconductor-based materials have been developed as active photocatalysts in the ultraviolet radiation and visible light range [13]. Metal oxides are the most extensively researched semiconductors for photocatalytic applications, among which TiO_2 to date, is a material for industrial use due to its efficient photoactivity, high stability and low-cost [14, 15]. The Compoud $BiVO_4$, Fe_2O_3 and WO_3 were also well studied [16, 17, 18]. The drawback of metal oxides is mostly due to their redox potential, which is suitable for oxygen O_2 evolutions [17]. Thier unfavourable electronic properties with large energy gaps >3 eV which falls in the ultra-violet and hence can not be used as visible light absorbers. Photocatalysts like Fe_2O_3 have an appropiate band gap for water-spliting, but it have photo-generated carrier and transport problems. These are most of the time are accompanied by poor photo efficiency to be active visible light photocatalysts [19, 20].

Metal chalcogenides are also not left out in the search of semiconductor for one-step photocatalytic applications. In pioneering work, Helmut [21] and Kline [22] reported that $MoSe_2$ and WSe_2 can be efficient photoanodes for stable photoelectrochemical cells.

Thus their findings reveal that metal chalcogenides can be developed as photoelectrochemical and photocatalyst materials. Recently, bulk binary and monolayers metal chalcogenides MX (M = Ge, Si, Sn and X = S, Se) [23, 24], WS_2 [25] and cadmium chalcogenides CdX (X = S, Se and Te) [8] have recieved attention for photocatalytic applications. They have been reported to possess favourable photocatalytic potentials for water splitting. Although some of the drawbacks associated with metal chalcogenides are related to over potential [23]; for hydrogen production and the sulphur based compounds also turned out to have large band gaps [26] which is not suitable for visible solar energy conversion. These problems are addressed sometimes using a two-step excitation Z-Scheme/heterojunctions and monolayer approach are employed [24, 25] to improve photocatalyst activities of binary metal chalcogenides compounds.

Basically, there are at least two fundamental functions required for a good one-step semiconductor photocatalyst for water splitting: to harvest maximum part of the solar spectrum and perform the catalytic function of efficient water reduction and oxidation. Therefore, for an ideal semiconductor to perform this functions, it must possess an appropriate band gap for solar energy absorption, proper band edges positions for reduction and oxidation and good stability under required reaction condition. Recently, ternary and multinary chalcogenides (MCS) were reported to exhibit these characteristics and are regarded as promising candidates for photocatalytic hydrogen H_2 production [27]. Among these are the 1_2-111-$V1_4$ and 1_2-11-1V-$V1_4$ group semiconductors [27, 28]. Compounds such as Cu_2WS_2 [29] Ba_2ZnSe_3 [30] and $BaAu_2S_2$ [31] were found to exhibit excellent visible-light response photocatalytic and thermal stability, and in addition posses band gaps between 2.0 - 2.75 eV with suitable band structure that can be modified by alloying and stability under the reaction condition. These recent studies [27, 30, 31, 28] have demonstrated that some ternary and multinary chalcogenides semiconductors are suitable potential candidates for visible light harvesting photocatalysts due to their: i) appropriate band gap positions, ii) tunable band structures, shapes, size and crystal structures, iii) excellent thermal stability and iv) possess good electron-hole-generating centers and are possible future excellent visible-light photocatalysts.

The chalcogenidometalates, the seleno-germanates and thio-stannates with formula A_2MQ_4 (A = Alkaline-earth metal; M = Si, Ge and Sn; Q = chalcogenides) have not been investigated for water splitting. Although their counterpart (metal chalcogenide) were reported as promising one-step photocatalytic water splitting material due their physical properties and band gap position [32, 33, 34]. In comparison to the metal

chalcogenide, the chalcogenidometalates, the seleno-germanates and thio-stannates compounds [35, 36, 37, 38] were also reported to possess interesting structures and turnable physical properties with optical band gaps between 2 - 3 eV [34, 37, 38, 39, 40]. Hence, chalcogenidometalates compounds can also be promising photocatalytic materials.

1.2 Photocatalysis

There is no clear cut definition of photocatalysis agreed within the scientific community. According to IUPAC, photocatalysis is defined as the reactions carried out in the presence of a semiconductor and light or a photoinduced reaction which is accelerated in the presence of semiconductor as a catalyst [15, 41]. There are two major types of photocatalysis processes: the homogeneous type where the reactant and photocatalytic exist in the same phase, for example; coordination compounds, dye sensitizers and natural figments. Heterogeneous photocatalysis is when the reactant and photocatalyst exist in different phases, for example; the semiconductor metal oxide.

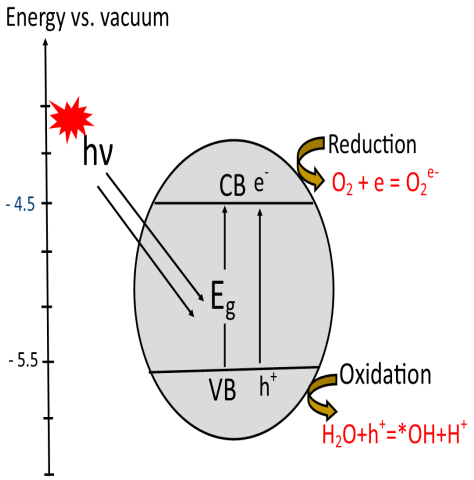

Figure 1.1: Schematic diagram of the photocatalytic process on the semiconductor photocatalyst.

As illustrated in Figure 1.1, the process of photocatalysis is a two-half reaction process involving three steps: the absorption of light by photocatalyst, generation and separation of electron-hole pairs and redox reaction at the surface of photocatalyst [11]. The process is initiated by the reaction, when photocatalyst absorbs a photon with

appropriate energy equal to or greater than its band gap energy. The absorbed photon creates electron-hole pairs charge separation from the valence band (VB) of semiconductor to the conduction band (CB), leaving a hole-pair charge in the valence band as the excited electron migrates to the surface. This excited electron is transferred to a semiconductor surface and reduce any substrate or react with any acceptor like O_2 present while the hole-pair left in the valence band is utilized to oxidize water. The major challenge after electron excitations is the electron-hole charge separation and transfer to the semiconductor surface, which is a critical step in photocatalytic reaction and its efficiency in semiconductor base photocatalyst, because of the effects of charge recombination and the lifetimes of photogenerated charge carriers [13]. A severe recombination of photogenerated electron-hole pairs on the surface results in poor performance of photocatalyst which can be mitigated by an in-built electric field and the use of high photoconductive semiconductor materials [11, 13]. The efficiency of a photocatalyst depend on the positions of VB and CB in semiconductor materials. The top valence band must be more positive than the oxidation potential of H_2O (1.23 V) and the bottom of conduction band must be more negative than the reduction potential of H^+ (0.0 V), or with respect to band edge position derived from flat band potential to the normal hydrogen electrode (NHE) of vacuum level reduction redox potential of (- 4.44 eV) and oxidation redox potential (-5.67 eV) [42].

The efficiency or quantum yield of the photocatalytic process is a combination of all the pathway probabilities for electron and hole. For an ideal photocatalytic system, efficiency is given by the proportionality relation [42]

$$\phi \propto \frac{k_{CT}}{k_{CT} - k_R}, \tag{1.2.1}$$

which is proportional to the rate of charge transfer processes (k_{CT}) and inversely proportional to the sum of charge transfer rate (k_{CT}) and the electron-hole recombination rate (k_R) at bulk and surface. For $k_R = 0$ (no recombination), the quantum yield take the ideal value of one and k_{CT} depends on the diffusion of charge carrier to the surface in absence of excess surface charge. But in real system recombination can occur because the concentration of electrons and holes at the surface are not equal. For more detail reader is invited to read reference [43].

The processes in water splitting to H_2 and O_2 is an uphill reaction which can be sum-

marized using the relations [13, 44]

$$\begin{aligned} &\text{Semiconductor} + 2h\nu \rightarrow 2\text{h}^+ + 2\text{e}^-, \\ &\qquad\qquad \text{H}_2\text{O} + 2\text{h}^+ \rightarrow \frac{1}{2}\text{O}_2 + 2\text{H}^+(E_{\text{O}_2/\text{H}_2\text{O}}), \\ &\qquad\qquad 2\text{H}^+ + 2\text{e}^- \rightarrow \text{H}_2(E_{\text{H}_2\text{O}/\text{H}_2}), \\ &\qquad\qquad \text{H}_2O \xrightarrow{h\nu} \frac{1}{2}\text{O}_2(\text{g}) + \text{H}_2(\text{g}). \end{aligned} \tag{1.2.2}$$

hence, the last equation requires the standard Gibb's free energy charge ΔG^0 of 237 kJ/mol or 1.23 eV. Therefore, to achieve water splitting the photocatalyst must have energy band gap of $>$ 1.23 ($<$ 1000 nm) and to harvest visible light E_g should be $<$3 eV ($>$400 nm) [13, 44, 45].

1.3 Metal chalcogenides (chalcogenidometalates)

Ternary and quaternary metal chalcogenides, the chalcogenidometalates compounds, with structural complexes A[M_yQ] and A[M_xM_yQ] (A = Alkaline, earth-alkaline; M_y = main group of element of group 13 - 15, Q = chalcogenides and M_x = transition metals) were subject of inorganic materials research since 1970 [32, 46, 47]. The technological importance of this class of compounds was first made clear in an article by Bedard et al. [48], where they reported the unprecedented structural chemistry of germanium sulfide having substantially more pore volume to incorporate many transition metal elements than most of the microporous oxides. Structural diversity of chalcogenidometalates anionic $[M_yQ]^{n-}$, $[M_xQ]^{n-}$ structure is important in the construction of different phases using different synthetic method [32] and usually exhibits good physical properties when semi-metals (Si, Ge, Sn, Sb and Se etc.) ions are present in the anions coordinations [46]. Some of the ternary chalcogenidometalates reported in the literature are the thio-germanates (Argyrodites), seleno-germanates, thio-(silicates, borates, gallates and Indates) and halides of silicon and germanium [46, 49] and their potential application of magnetic, optoelectronics, nonlinear optical (NLO) has been proven [32, 37, 38].

1.3.1 Seleno-germanates

Krebs and co-workers pioneered the preparation of thio- and seleno-germanates and the stannates from the reaction of alkaline metal chalcogenides with MQ_2 coordination (M = Ge, Sn; and Q = S, Se) [49]. The crystal chemistry of ternary seleno-germanates and stannates with alkaline or earth-alkaline metals were extensively investigated. The reported crystal structures of the A_2MQ_4 compounds (A = alkaline or earth-alkaline metals; M = group 14 elements and Q = chalcogenides) depend strongly on the ratio of the ionic radii $r_A/(r_M + r_Q)$ [35, 50]. The smaller values of the cation A radius mostly crystallize in an olivine structure and the larger values take $\beta - K_2SO_4$ structures. Most of thio- seleno-germanates and stannates are usually built with an isolated anionic block with the cation M atom in a tetrahedral coordination $[MQ_4]^{4-}$ and the cation A atom are in distorted octahedral coordinations $[AQ_6]$ [38, 51]. Many novel compounds with structural coordinations $[M_2Q_6]^{6-}$ and $[M_2Q_7]$ have also been discovered [38]. These compounds have received attention in recent years because of their structural diversity, interesting physical properties and potential technological applications [37]. Amongst these are the ternary seleno-germanate Mg_2GeSe_4, γ-Sr_2GeSe_4 and Ba_2GeSe_4 [38, 35, 36] for which synthesis, characterization and their applications has been reported.

Mg_2GeSe_4

Kui et al. [38] investigated and reported the synthesis and characterization of seleno-germanates Mg_2GeSe_4 with an olivine Mg_2SiO_4 structure type [52]. They reported that Mg_2GeSe_4 has an orthorhombic structure (space group pnma at room temperature). The compound has the usual characteristic of isolated tetrahedral $[GeSe_4]^{4-}$ units and the octahedral $[MgSe_6]$ coordinations of the chalcogenidometalates, which are connected together to form the structure. In their experimental measurement, an optical band gap of 2.02 eV was measured using diffuse reflectance spectra and a 1.57 eV indirect band gap from a theoretical calculation using density functional theory (DFT). However, to the best of our knowledge in the literature there is no reported mechanical and dynamical properties for Mg_2GeSe_4 nor a careful theoretical investigation of the gap energy.

γ-Sr_2GeSe_4

The Sr_2SnSe_4 and γ-polymorph Sr_2GeSe_4 are isostructural. These compounds were synthesized using similar methods [35] and are found to crystallize in an orthorhombic Ama2 space group. The γ-Sr_2GeSe_4 polymorph does not behave as a high-temperature phase, therefore, it cannot be synthesized by quenching of the monoclinic α-Sr_2GeSe_4 from 1073 K to room temperature. The γ-Sr_2GeSe_4 has regular tetra of the A_2MQ_4 compound, but because of the co-existant of eightfold coordination (CN8) and sevenfold coordination (CN7) with the packing of the tetrahedral it forms a new variant in the A_2MQ_4 structure family. Only the synthesis and characterization of γ-Sr_2GeSe_4 were reported, while other properties like electronics, mechanical and dynamical stabilities and optical properties are missing in the literature.

Ba_2GeSe_4

Assoud et al. [36] reported the synthesis and characterization of single-crystal Ba_2GeSe_4. Ba_2GeSe_4 is reported with Sr_2GeS_4 structure type in monoclinic space group $P2_1/m$ at room temperature. Its yellow appearance suggests a material with a band gap between 2.60 - 3.00 eV. Physical properties of Ba_2GeSe_4 can be fine-tuned by substituting the two to three selenium (Se) atom sites with tellurium (Te) to form its isotypic quaternary ordered variants $Ba_2GeSe_2Te_2$ and $Ba_2GeSe_{1.5}Te_{2.5}$ with calculated narrowed band gaps respectively. Ba_2GeSe_4 can be classified as ortho-germanate with existence of discrete $GeSe_4$ tetrahedral in the structure. Ba_2GeSe_4 like γ-Sr_2GeSe_4 also have two co-existent polyhedral coordinations, the ninefold (CN9) and eightfold (CN8) selenium to barium atom. The ninefold (CN9) a tri-prism and eightfold (CN8) a bi-capped prism coordinations together with tetrahedral $GeSe_4$ form the Ba_2GeSe_4 structure. Co-existence of 2 types of coordination in this compound and γ-Sr_2GeSe_4 cannot be unconnected with slightly larger ionic radii of the cation atoms Ba^{2+} and Sr^{2+} which require higher coordination units (CN) [35] and the balance between the packing of tetrahedral and the optimal coordination of the large cation within this parking to form the structure. To our knowledge, the mechanical, dynamic and optical properties of Ba_2GeSe_4 have not been discussed elsewhere.

Ca_2GeSe_4

Ca_2GeSe_4 is a hypothetical compound, its synthesis and characterization have not been reported, but formally, the compound can be formed by substituting Si with Ge in the Ca_2SiSe_4 configuration, an olivine Mg_2SiO_4 structure type [53]. In our recent work [1], we investigated the structural, mechanical, dynamical stabilities and optical properties of this compound. The relative stability of Ca_2GeSe_4 calculated from the formation and cohesive energies is negative, indicating that it is energetically favourable for given constituents to mix and form a stable Ca_2GeSe_4 phase. Similarly, the calculated mechanical and dynamical properties show that Ca_2GeSe_4 is mechanically and dynamically stable. Our calculations confirm that Ca_2GeSe_4 is stable in an orthorhombic structure, pnma space group.

1.4 Aim and Objectives

We are motivated by the reported good physical properties and structural chemistry of the chalcogenidomatalates from the group of thio- and seleno-germanates discussed in Section (1.3) to carry out this study. The aim of this research is to investigate the structural stabilities, electronic and optical properties, as well as the photocatalytic properties of a group of compounds known as seleno-germanates.

The objectives of this research are enumerated below:

1. To carry out the structural and electronic properties investigation within density functional theory.
2. To calculate elastic constants and phonon band structures in order to investigate the mechanical and dynamical stabilities.
3. To compute the fundamental gap within hybrid functional and many-body perturbation theory and optical properties from BSE approximations such as the real and imaginary parts of the dielectric constant, refractive index, reflectivity, energy loss, extinction and absorption coefficients.
4. Construct periodic supercell slab two-dimensional (2D) structures of low index 100, 101, 110 and 111 surface facets using the slab-approach in order to perform the test of convergence to determine the required periodic supercell slab thickness,

vacuum size and compute surface energy to determine surface facet stability.

5. From the stable surface facet to calculate the surface properties like average electrostatic potential, band gap center (BGC) and work function (Φ).
6. To calculate the electronic structure of the stable surface using density functional theory in order to determine surface electronic properties.
7. To perform Bader charge analysis, for the assessment of charge depletion and accumulation on the isosurface.
8. To calculate band edge positions using band gap center (BGC) and crystal bulk quasiparticle G_0W_0+BSE band gap.
9. To aligned band edge position the valence band maximum and conduction band minimum energy with respect to standard hydrogen electrode (SHE) for bulk using Mulliken analysis and for the surface band-edge alignment with respect to vacuum potential versus NHE both at pH = 0 and 7. In order to determine their suitability for photocatalytic applications.

1.5 Thesis structure

The rest of the thesis is structured as follows. In Chapter 2, we introduce the relevant theoretical background, including the solution to the quantum many-body problem and density functional theory. In chapter 3, the computational techniques are discussed. How the relevant theoretical background will be implemented and applicable to computational scheme to study, the ground-state and excited-state properties of bulk, as well as, the surface properties of extended two-dimensional (2D) structures. In Chapter 4, our calculated results and findings are dicussed. In Chapter 5, we summarize our findings and give future outlook.

2

Theoretical Background

The outline of the quantum mechanical simulations used in this thesis is presented in this chapter. The theoretical predictions of material properties are important aspects of physics and chemistry of materials. In the past few decades, significant advancements have been recorded in the calculations of complex systems that are experimentally costly and can be achieved using simulation methods. Some quantities like surface energy, surface facets stability, making interpretation of complex data and predictions of structures and properties yet inaccessible by experiments or are difficult to quantify experimentally are relatively made possible theoretically. Furthermore, theory predicts the properties of a system and explains experimental findings; more importantly the electronic structure of the system. Density Functional Theory (DFT) plays an important role in this regard. Exchange-correlation functionals such as the local density approximation (LDA) and generalized gradient approximation (GGA) provide reasonable explanations of electronic structure of matter. Many-Body Perturbation Theory (MBPT) in the Green's Function with screened coulomb interaction approximation (GW) attain substantial accuracy in describing the electronic excitations in solids and their surfaces. These are discussed underneath.

2.1 Density Functional Theory

In calculating the properties of matter (molecules and solids), Density Functional Theory (DFT), recorded tremendous impacts and applications to different problems and

provide the near realistic results, while the field continues to expand [54]. The basic idea of DFT stem from Hohenberg-Kohn and Kohn-Sham theories [55, 56]; the simplification of understanding behaviour of a system with the formulation of the problem that involves the total density of electrons $n(\mathbf{r})$. The aim of DFT, which is a quantum mechanical theory is to find an approximate solution to the many-body system with the structure and dynamic of many-electrons systems. These systems comprise of a single atom, molecules, mesomorphic, solids, layered structure and surfaces. Solving the problem of these structured systems is an area of concern in Condensed Matter Physics, Chemistry and Computational Materials Science. From the first principle approach (DFT), the starting point in the analysis of the electronic structure of matter is to derive the approximate solution to fundamental time-independent many-body Schrödinger equation with the form of the many-body wave function:

$$\hat{H}\Psi(\mathbf{R}_I;\mathbf{r}_i;t) = i\hbar\frac{\partial}{\partial t}\Psi(\mathbf{R}_I;\mathbf{r}_i;t); \tag{2.1.1}$$

where $\Psi(\mathbf{R}_I;\mathbf{r}_i;t)$ is the wave function of a many-body system which describes the quantum mechanical behaviour of the system; $\mathbf{R}_I$ (I= 1,2,3,...,K) is the position of the I^{th} nucleus, $\mathbf{r}_i$ (i= 1,2,3,...,N) is the position of the i^{th} electron, K are the number of nuclei and N are the number of electrons. In Equation 2.1.1 spin dependance has been suppressed for simplicity of notation.

2.1.1 Many-body problem

In describing the properties of matter from the first principle approach, the starting point is non-relativistic Scrödinger equation, Hamiltonian of a coupled electron-nucleus system [57]. The Hamiltonian discussed here is strictly non-relativistic and the nuclei are point particles characterised by mass, charge and magnetic moment only. Thus, discussion on spin is left out. Interactions between the charged particles are given by instantaneous and spin-independent coulomb interaction of the form:

$$\begin{aligned}\hat{H} = &-\frac{\hbar^2}{2m_e}\sum_{i=1}^{N}\nabla_i^2 - \sum_{I=1}^{P}\sum_{i=1}^{N}\frac{Z_I e^2}{|\mathbf{R}_I-\mathbf{r}_i|} + \frac{1}{2}\sum_{j\neq i}^{N}\sum_{i=1}^{N}\frac{e^2}{|\mathbf{r}_i-\mathbf{r}_j|} - \sum_{I=1}^{N}\frac{\hbar^2}{2M_I}\nabla_I^2 \\ &+ \frac{1}{2}\sum_{I=1}^{P}\sum_{J\neq I}^{N}\frac{Z_I Z_J e^2}{|\mathbf{R}_I-\mathbf{R}_J|},\end{aligned} \tag{2.1.2}$$

With the general form of the Hamiltonian given as:

$$\hat{H} = \hat{T}_n + \hat{V}_{nn} + \hat{T}_e + \hat{V}_{en} + \hat{V}_{ee}. \tag{2.1.3}$$

Where $\hat{T}_n$ is the kinetic energy of K nuclei of the system, $\hat{V}_{nn}$ the repulsion interaction among nuclei, $\hat{T}_e$ kinetic energy of the electron, $\hat{V}_{en}$ interaction between nuclei and electron and $\hat{V}_{ee}$ the interaction between electrons.

The analytical solution of the time-independent schrödinger equation (2.1.1) for an interacting system of (m+M) particles is difficult even for a small system. Several approximations are required for a solution to be attained. Born-Oppenheimer Approximation [58] de-coupled the time-independent schrödinger equation and the simplified Hamiltonian. In Born-Oppenheimer approximation the ion core is so massive than the electrons, its characteristic velocity is much slower. The electrons generally react so quickly that the ion cores can be considered stationary. This allows to separate the degree of freedom of the electron and nuclei [59] and allows the electronic part of the Hamiltonian to be de-coupled:

$$\hat{H} = -\frac{\hbar^2}{2m_e}\sum_{i}^{N}\nabla_i^2 - \sum_i V_{ext}(\mathbf{r}_i) + \frac{1}{2}\sum_{i=j}\frac{e^2}{|\mathbf{r}_i - \mathbf{r}_j|}. \tag{2.1.4}$$

The external potential $V_{ext}(\mathbf{r})$ in equation (2.1.4) is the attractive potential exerted on the electrons due to the nuclei and account for the electron-nuclei interaction. The validity of Born-Oppenheimer approximation is based on the huge difference of mass between ions and electrons (three to five orders of magnitude), making the former behave like classical particles [54]. The only exception to this are the lightest elements (especially hydrogen H), where the ions have to be treated as quantum mechanical particles. Since the theory merely considers only the classical point charges and masses exerting a potential on the fully quantum mechanically treated electrons, it therefore fails to account for electron-phonon interaction in solids.

2.1.2 Thomas-Fermi Model

In an attempt to calculate the energy of an electronic system quantitevely in terms of its density. Thomas-Fermi [60, 61] proposed that many-electron wave function can be replaced by non-interacting quatinty, such as the electron density $n(\mathbf{r})$ as a fundemental

quantity. They proposed an expression for total energy of an electronic system as a function of density, where, electron is considered as non-interacting particle in a homogeneous gas whose density is equal to the local density at any given point.

They arrived at a simple expression of the kinetic energy:

$$T_{\mathrm{TF}}[n(\mathbf{r})] = \frac{3}{10}(3\pi^2)\int n^{\frac{5}{3}}(\mathbf{r})dr, \tag{2.1.5}$$

and energy is derived from the combination of $T_{TF}[n(\mathbf{r})]$ with classical approximations of nuclear-electron attraction and electron-electron repulsion respectively

$$E_{\mathrm{TF}}[n(\mathbf{r})] = T_{\mathrm{TF}}[n(\mathbf{r})] - \mathbf{Z}\int \frac{n(\mathbf{r})}{r}dr + \frac{1}{2}\iint \frac{n(\mathbf{r}_1)n(\mathbf{r}_2)}{r_{1,2}}dr_1dr_2. \tag{2.1.6}$$

In the Thomas-Fermi model, the exchange and correlations are neglected. Dirac [62] introduces the exchange into Thomas-Fermi model and formulated a local approximation for exchange electron energy functional Thomas-Fermi-Dirac ($E_{\mathrm{TF}D}$) in an external potential V_{ext} as:

$$\begin{aligned} E_{\mathrm{TF}D}[n] = C_k\int d^3r n(\mathbf{r})^{\frac{5}{3}} + \int d^3r V_{ext}(\mathbf{r})n(\mathbf{r}) + C_X\int d^3r n(\mathbf{r})^{\frac{4}{3}} \\ + \frac{1}{2}\iint d^3r dr' \frac{n(\mathbf{r})n(\mathbf{r}')}{|\mathbf{r}-\mathbf{r}'|}. \end{aligned} \tag{2.1.7}$$

where $C_k = \frac{3}{10}(3\pi^3)^{\frac{2}{3}}$=2.871 and $C_X = \frac{3}{4}(\frac{3}{\pi})^{\frac{1}{3}} = 0.739$ are Hatree constants [63] with $\int d^3r n(\mathbf{r})^{\frac{5}{3}}$ the local density approximation to kinetic energy, $\int d^3r V_{ext}(\mathbf{r})n(\mathbf{r})$ is exchange terms and $\frac{1}{2}\int d^3r dr' \frac{n(\mathbf{r})n(\mathbf{r}')}{|\mathbf{r}-\mathbf{r}'}$ is classical electronic Hartree energy [57, 62, 63] respectively.

Now that the energy as a function of density $n(\mathbf{r})$ including the exchange is derived in Thomas-Fermi-Dirac (TFD) expression, the correct density needed is determined with help of Variational principles, subject to constraint that the total integrated charge be equal to the number of electrons $\int n(\mathbf{r})d\mathbf{r} = N$ [63]. The ground state energy is obtained from minimized E_{TFD} subject to constraint via the Lagrange multiplier energy μ read as:

$$\frac{\delta}{\delta n\mathbf{r}}\left(E_{\mathrm{TF}D}[n] - \mu\int n(\mathbf{r})d\mathbf{r}\right) = 0. \tag{2.1.8}$$

Although, the Thomas-Fermi and TFD models are remarkable in approximating the kinetic energy of the system of electrons as an explicit functional of the density and

provide for a simple crude description of inhomogeneous systems, they fall short of basic Physics and Chemistry of the shell structure of atoms and binding of molecules; and therefore are not very successful in chemical applications. Hohenberg and Kohn [55] provides extension of the work of Thomas-Fermi-Dirac method and their limitations.

2.1.3 Hohenberg and Kohn Theorems

The Hohenberg and Kohn theorems generalized the Thomas-Fermi method to any kind of electron system and formulate an exact theory of many-body system that established the basis of DFT. The formulation of N-electron and M-nuclei systems applicable to any system of an interacting particle in an external potential (V_{ext}) and to the system with electrons and fixed nuclei, where the Hamiltonian can be written in the form:

$$\hat{H} = -\frac{\hbar^2}{2m_e}\sum_{i}^{N}\nabla_i^2 - \sum_i V_{ext}(\mathbf{r}_i) + \frac{1}{2}\sum_{i=j} Z\frac{e^2}{|\mathbf{r}_i - \mathbf{r}_j|}. \tag{2.1.9}$$

Hohenberg and Kohn suggested two theorems which are the basis of density functional theory:

Theorem 1 *states that, for any system, the external potential* V_{ext} *is univocally determined by the ground state electronic density* $n_0(\mathbf{r})$ *beside trivial additive constant* [63]. Theorem 2. *states that, for a trial density* $\tilde{n}(\mathbf{r})$ *that is non-negative* $\tilde{n} \geq 0$ *and normalized to* $N = \int \tilde{n}(\mathbf{r})d^3r$ *associated with external potential* $\tilde{V}_{ext}$*, define the minimum variational energy* E_v *which is a functional of density* [55].

The implicaton of the statements above is that, there are no two different external potentials V_{ext} that gives the same ground-state density, hence, associated with the ground-state density $n_0(\mathbf{r})$ there is a one-one mapping of external potential V_{ext} in the Hamiltonian and the non-degenerate ground state wave function. Therefore, $V_{ext}, |\psi_0\rangle$ and $n_0(\mathbf{r})$ determined each other uniquely. The ground-state properties of a system is a unique functional of ground-state density.

Since any of the observable ground state properties are uniquely determined if the density is specified, then such property can be viewed as density functional including the total variational energy functional $E_{\mathrm{HK}}[n]$. Therefore for any given ground state energy $E_{HK}[n_0]$, there exists universal functional $F_{\mathrm{HK}}[n_0]$ which does not depend explicitly on external potential but depend on the electronic density [63]. If this universal functional

is known, minimizing the system of total energy with respect to variation in density will give the exact ground state density and energy [55].

However, the HK theorem does not give an explanation on explicit form $F_{\mathrm{HK}}[n]$ of $E_{HK}[n]$ that gives the ground state energy and moreover, the theorem motivation is for the only non-degenerate system. Levy [64] and Lieb [65] used constraint search method to extend HK theorem reformulation and guarantee the antisymmetry origin of density from non-degenerate cases to degenerate cases. A decent discussion and proof of these theorems is provided therein [55, 64, 57, 63].

2.1.4 Kohn and Sham DFT-Approach

Kohn and Sham (KS) [56] used the HK theorems of interacting electrons and properties of uniform electron density/homogeneous electron density, to study the real (i.e. inhomogeneous) system. KS reformulated the problem and made it more practical by proposing the Ansatz upon two assumptions: (i) that the exact density can be replaced by density from a non-interacting electron system and (ii) the auxiliary Hamiltonian is chosen to have the usual kinetic energy operator and an effective potential V_{eff} acting on an electron at a point $(\mathbf{r})$ [57]. Kohn-Sham replaced the many-body interacting system with the auxiliary non-interacting system having the same density such that properties of the system can be calculated with an independent particle method. Thus in this approach, the total energy can be written in the form:

$$E_{\mathrm{KS}}[n] = T_s[n] + \int d^3r V_{ext}(\mathbf{r})n(\mathbf{r}) + \frac{1}{2}\iint d^3r d^3r' \frac{n(\mathbf{r})n(\mathbf{r}')}{|\mathbf{r}-\mathbf{r}'|} + E_{XC}[n] \qquad (2.1.10)$$

where the first three terms are the independent kinetic energy of non-interacting electron with density, the external potential contribution due to the nuclei and any other external field and the Hartree energy (the Coulomb energy of the density treated by classical charge). The last term $E_{XC}[n]$ is the exchange and correlation energy of the interacting system, which is a functional of the density. The implementation of KS formalizations is to define an acceptable approximation of $E_{XC}[n]$ functional which is unknown.

Accordingly, the KS auxiliary system is solved by minimizing the KS total energy and the product is like Schrödinger's one-particle equation (the Kohn-Sham equation) with an auxiliary wave function $\Psi(\mathbf{r})$ known as Kohn-Sham orbital and potential V_{KS} as effective potential or the Kohn-Sham potential. KS orbital is an auxiliary function

for calculating electron density. The relation between the auxiliary non-interacting system and the real, interacting system is the effective potential. Thus, the V_{KS} is equal to the sum of V_{ext}, V_H and V_{XC} the external, Hartree and exchange-correlation potentials respectively, for the electronic density of two systems to be equal. The unkown $V_{XC} = \frac{\delta E_{XC}}{\delta n(\mathbf{r})}$. Therefore, the KS formalism is exact and would lead to an exact ground state of an interacting many-body system, provided E_{XC} is known by solving KS equation self-consistently.

2.2 Solution of Kohn-Sham equation

2.2.1 Exchange-correlation functional

The KS formalization so far has been exact, the crucial quantity is the exchange functional $E_{XC}[n]$ of density for which the explicit form is unknown. Knowing this quantity is of great importance in DFT calculations of material properties. The need for more accurate calculations led to the developments of the hierarchy of exchange-correlation functional approximations namely, the local density approximation (LDA), Generalized Gradient Approximation (GGA), meta-GGA and hybrid functional (hyper-GGA and RPA) referred to as Jacob ladder constructed by adding the ingredient to KS orbital [66, 67]. For the purpose of this thesis, here we discuss the GGA, meta-GGA and hybrid functional approximations.

2.2.2 Generalized Gradient Approximation (GGA)

The GGA is an extension of Local Density Approximation through the addition of the gradient correction to the local density which would account for non-homogeneity of the true electron density. The scheme is found to be applicable to surface calculations, as well as the extensive self-consistent calculations of energies and densities in atoms [68, 69]. The general form of Generalized Gradient Approximation (GGA) takes the form [69]:

$$E_{XC}^{\mathrm{GGA}}[n_\uparrow, n_\downarrow] = \int d^3r n\varepsilon_{XC}^{\mathrm{GGA}}(n_\uparrow, n_\downarrow, \nabla n_\uparrow, \nabla n_\downarrow). \tag{2.2.1}$$

where $\nabla n_\uparrow$ and $\nabla n_\downarrow$ are the density gradients and $\varepsilon_{XC}^{\mathrm{GGA}}$ is exchange-correlation energy.

Perdew-Burke-Ernzerhof (PBE) [69] and the revised Perdew-Burke-Ernzerhof (PBEsol)

[70] are the most popular used GGA in describing equilibrium properties of solids.

2.2.3 Meta-GGA

Meta-GGA, the third rung of Jacob ladder, takes into consideration all the ingredient of local spin density (LSD) which is exact for uniform electron gas [56, 71] and that of generalized gradient approximation (GGA) exchange-correlation energy [69]. Furthermore in Meta-GGA, the ingredient of semilocal information, the second-order gradient expansion of density or kinetic energy density of occupied Kohn-Sham orbitals are all added. Given in a summarized Equation [72, 73]:

$$E_{XC}[n_\uparrow, n_\downarrow] = \int d^3 r n \varepsilon_{XC}(n_\uparrow, n_\downarrow, \nabla n_\uparrow, \nabla n_\downarrow, \tau_\uparrow, \tau_\downarrow), \tag{2.2.2}$$

where τ is Kohn-Sham orbital kinetic energy.

Some of the prominent meta-GGA functionals are TPSS [74], RTPSS [73], M06L [75] and MBJ, the modified Becker Johnson potential [76] in combination with LSDA [76] yield band gaps similar to hybrid functional and GW. Hence, we employed MBJ in electronic band structure calculations in chapter 4.

2.2.4 Hybrid-functional

The Hartree-Fock (HF), local density approximation (LDA) and the GGA approximations have greatly influenced the study of the many-electron system (atoms, molecules and solids). However, the trend of HF differs with that of LDA and GGA. HF provides a good description of the atomistic core region, whereas the LDA and GGA provide an accurate description of exchange-correlation involving the valence electrons. Hybrid-functional is a unification of the two approaches. A.D Becke [77] derived a new coupling of the two theories using the adiabatic connections. Other early methods were proposed in references [78] and [79]. The general form involved a DFT correlation with a combination of DFT and HF-exchange given in the form [63]:

$$E_X^{hyb}C = \alpha E_X^{HF} + (1+\alpha)E_X^{DFT} + E_C^{DFT} \tag{2.2.3}$$

The most popular hybrid-functionals are B3LYP [80], PBE0 [81] and Heyd-Scuseria-Ernzerhof (HSE) [82] exchange-correlation functional. In chapter 4 of this thesis HSE

is used for the description of electronic properties because, HSE improve computational efficiency using error function to split the coulomb operator into short-range (sr) and long-range (lr); ($\frac{1}{r} = S_w(r) + L_w(r)$).

2.2.5 Planewave basis set

The choice of basis set is a step toward in solving the Kohn-Sham equation. Among the type of basis sets used as a choice are the plane waves, linear augmented plane wave, linear muffin-tin orbitals etc. For the expansion of Kohn-sham orbital, VASP [83, 84] uses plane-wave basis set. Bloch's theorem [85] suggest the plane-wave character of the wave function and set the stage for plane-wave basis set. The theorem states that in a periodic solid, the wave function of an electron can be expressed as the product of plane wave ($e^{i\mathbf{k}.\mathbf{r}}$) and a function with the periodicity of the lattice $u_{\mathbf{k}}(\mathbf{r})$. The KS orbital is expanded and solved in the KS equation to obtain [57]:

$$\sum_{\mathbf{G}}[(\frac{\hbar}{2m}|\mathbf{k}+\mathbf{G}|^2)\delta_{\mathbf{G}\mathbf{G}'} + V_{KS}^{\sigma}(\mathbf{G}-\mathbf{G}')]c_{i,\mathbf{k}+\mathbf{G}'} = \epsilon_i c_{i,\mathbf{k}+\mathbf{G}'} \tag{2.2.4}$$

where $\mathbf{k}$ is the wave vector, $\mathbf{G}$ the so-called reciprocal lattice vector, $\frac{1}{2}|\mathbf{k}+\mathbf{G}|^2$ is truncated for accurate calculation by fixing the energy cut-off; $V_{KS}^{\sigma}(\mathbf{G}-\mathbf{G}')$ is the Fourier transform of the effective KS potential and $c_{i,\mathbf{k}+\mathbf{G}'}$ is coefficient that is set to determine the lowest energy solution.

For the extended system periodic in two dimensional (2D), $e^{i\mathbf{k}\mathbf{r}}$ is a plane wave and $u_{\mathbf{k}}(\mathbf{r})$ is the periodic function of the crystal lattice in the supercell given by $u_{\mathbf{k}}(\mathbf{r}+\mathbf{L})$, $\mathbf{L}$ is one of lattice vectors in periodic crystal, similar to the crystal bulk the solution to KS orbital take the form of equation 2.2.4. The two parameters that determine the accuracy of the calculation in DFT under the periodic boundary condition are the choice of k-point sampling and cutoff energy for expansion of the plane wave. For the extended system, the reciprocal vector depends on the size of the supercell and hence is more convenient to truncate the cutoff energy as:

$$E_{Cut} \leq \frac{1}{2}(|\mathbf{k}+\mathbf{G}|^2) \tag{2.2.5}$$

2.2.6 k-space and Brillouin zone

According to Bloch's theorem, the expression $\Psi_{\mathbf{k}}(\mathbf{r}) = \mathbf{e}^{\mathbf{ik.r}} * \mathbf{u}_{\mathbf{k}}(\mathbf{r})$ is a wave function of an electron in an external periodic potential. From this expression there is a particular class of vector $\mathbf{k}$ such that with phase factor $e^{i\mathbf{k}.\mathbf{a_i}} = 1$ and thus the wave function is in phase in all the periodicity replica of the unit cell. Hence set of three smaller independent vector of such vector are sufficient to determine all the reciprocal lattice vectors, in the same way as with the primitive lattice vectors in real space [63].

The primitive or Wiegner-Seitz cell defined from a reciprocal lattice using the vector $\mathbf{k}$ in reciprocal space is called the Brillouin zone [63].

2.2.7 Pseudopotential

When the choice of basis set is plane wave type, core electron of the atom becomes computationally expensive because they are localized. These means that a large number of the plane-waves are required to expand the wave functions. In order to address this problem, the pseudopotential approximations allow the electronic wave functions to be expanded using a much smaller number of plane-waves basis states [86] and it accounts for the complex nodal character of the valence orbital [87]. Furthermore, it is a well-known fact that most of the physical properties of a solid are dependent on the valence electrons to a much greater extent than the core electrons. The primary role of core electron wave functions is to ensure the proper orthogonality between the valence electrons and core states. Consequently, it is desirable to eliminate the core states altogether by replacing their action with effective potential or pseudopotential [63]. For an accurate description of bonding properties of true potential and to reproduce all-electron calculations, a careful construction of a pseudopotential is required. The origin of pseudopotential approaches can be traced back to Philips and Kleinman [88], while in the pseudopotential used are the norm-conserving pseudopotentials [89, 90] recent time, and Vanderbilt ultra-soft pseudopotential [91, 92] to mention a few. The VASP package used in this calculations uses ultra-soft Vanderbilt pseudopotentials (US PP) or the projector-augmented wave (PAW) method to the basis-set as small as possible.

2.3 Many-body perturbation theory (MBPT)

The Kohn-Sham density functional approach is the method of choice when interested in the ground state properties of many-electron system [56, 93, 94]. It provides the exact structural and some ground state physical properties of many solids. However, some of the drawbacks of KS-approaches are an underestimation of some semiconductors and insulators band gaps and failure to correctly predict excited state energies [94]. Since there is no formal justification to interpret the DFT eigenvalues for unoccupied states in quasiparticle energies [95, 87]. The widely used approach to quasiparticle energies and the spectral wave function is the many-body perturbation calculations based on quasi-approach the GW Green function method [59, 96, 97, 94].

2.3.1 Quasiparticle

Friedrich and Arno [98] illustrate single-particle as a quasiparticle from an experimentally measured indirect or direct photoelectron spectroscopy. Relative to the ground state N-electron system, the addition or removal of an electron in photoelectron spectroscopy creates or annihilates an ensemble consisting of the bare electrons and it's oppositely charged Coulomb hole. This so-called ensemble behaves in many ways like a single-particle and is thus called quasiparticle. The Coulomb hole reduces the total charge of the quasiparticle and hence, the interactions between the particles are screened and considerably weaker and therefore we have a system of the weakly interacting particle (quasiparticle). The idea of this quasiparticle was first introduced by Laudau [54, 59] that the property of strongly interacting system can possibly be treated in terms of constituents of weakly interacting particle. In such a case, one formulates a perturbation theory beginning with non-interacting particles as the unperturbed state, usually, the fictitious non-interacting particles involved in the Kohn-Sham formalization [59]. The difference between quasiparticle and bare particle is described by the quantity self-energy operator Σ, a non-Hermitian, energy-dependent, non-local operator that described the exchange and correlation effects beyond the Hartree approximation [96]. However, the successful approximation of the excited states in semiconductors and insulators is based on evaluation of the quasiparticle equation, and an adequate approximation of the self-energy operator Σ. These require rigorous quasiparticle formulation in a green function approach [97, 96].

2.3.2 GW approximation

The solution for self-energy operator as well as the one-particle Green's function can be obtained from the many-body problem, but their exact expression is not known exactly [99, 100]. The solution requires the two-particles Green's function [101], a method which is complex and not practicable. Hedin [97] proposed the practical solution of self-energy operator from the method of GW approximation, which defined the electronic self-energy as a product of the Green function G and screened interaction W. The method is simply an extension of HF theory by replacing the bare Coulomb interaction with a dynamical screened interaction W. In the formulation Hedin uses one-particle Green's function equation in conjunction with Dyson equation to introduce five set of equations in five variables to get the exchange-correlation, which are the single-particle operator G, self-energy Σ, screen interaction W, polarizability P and vertex function Γ. These set of five equations are solved self-consistently without further approximation. A detailed discussion of the so-called Hedin equations can be found in the references [97, 94, 100, 96, 63].

In the actual calculations, these set of Hedin equations are solved self-consistently [100], the vertex function is set to one (Γ=1) everywhere and thus the screen interaction W is calculated in the random phase approximation. The time-ordered dielectric matrix $\epsilon(\mathbf{r}, \mathbf{r}', w)$ are determined from the irreducible polarizability P using the Hartree or random phase approximation (RPA).

The GW method is still computationally expensive. Only the Green function G in the Hedin's equations exhibits the external potential via the non-interacting G_0. All other equations are universal and can be used to create the quantity of interest with increasing accuracy. The most simpler scheme of GW is the first iterative method G_0W_0 [94, 100] with DFT instead of Hartree as a starting point, where the Green function G is replaced by non-interacting G_0 in the GW approximation energy expression. Thus one calculates the corresponding non-interacting irreducible polarizability $P(12)$ and the corresponding screened interaction W_0 to obtain the self-energy $\Sigma^{xc} = -iG_0W_0$. These methods have become the standard ingredient of condense matter calculations and recorded successes in improving the DFT exchange-correlation energy and description of one-particle excited states [96], the procedure become increasingly too difficult iterating further due to neglect of order contribution in the vertex function (so-called vertex correction).

2.3.3 Bether-Salpeter equation (BSE)

The description of excitation state requires propagation of two particles (electron-hole pair) which is beyond the one-particle Green function GW approach. GW approach required the improvement in the response functions to account for two-particle Green function. The electron-hole pairs interaction can now be included by adding the vertex correction in vertex function which is beyond the RPA. This is done by including the vertex function Γ into polarizability function equation P through the second iteration and solve for polarizability ${}^3P$, four-point screened-interaction function ${}^4W$(1,2,3,4) and four-point Kernal function K(1,2,3,4) [102, 103]. In practice to perform BSE calculations requires one first to determine the static screened electron-hole interaction term W(x,x′;ω=0) and the quasiparticle bandstructure, typically from a GWA calculation [104, 103]. With this the effective two-particle Hamiltanion H^{2P} is built, H^{2P} is diagonalized to derive the expression of macroscopic dielectric function $\epsilon_M(\omega)$ directly related to measurable quantities. If one considers the positive resonance part of H^{2P} the resultant operator is Hermitian and its eigenstate orthogonal [102, 103]. H^{2P} contributes to the bare Coulomb interaction called the electron-hole exchange and contribution due to the screen electron-hole W is responsible for the appearance of bound states, and it can even lead to hydrogen like spectral features in insulators [102].

2.4 Surface properties

2.4.1 Work function and Electrostatic potential

At zero temperature work function Φ illustrated in figure 2.1 is defined as the energy difference between potential energy of an electron in a vacuum and the maximum energy of one-particle states (the Fermi-energy) [105]. For a crystal of N-electron with energy E_N in its ground state at its initial stage and an electron is removed from the crystal and assumed to be at rest, accordingly it has only electrostatic potential energy E_{vac}. At final stage the crystal is $N-1$ electron in its ground state with energy E_{N-1} [106]. Therefore, the work function is the energy required to remove an electron from the crystal and it is evaluated from the relation

$$\Phi = (E_{N-1} + E_{vac}) - E_N = E_{\text{vac}} - E_{\text{F}ermi}. \tag{2.4.1}$$

where in comparison $E_{\mathrm{F}ermi} = E_N - E_{N-1}$ and E_{vac} are the Fermi-energy and electrostatic potential respectively. For the theory of work function we refer reader to references [107, 105]

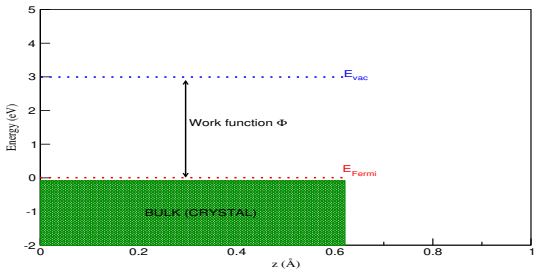

Figure 2.1: The schematic diagram of energy bulk crystal and work function Φ.

2.4.2 Surface dipole moment

The charge imbalance created due to the construction of periodic supercell slab in the presence of surface leads to a formation of surface dipole moment. The surface dipole moment is charge imbalance created, with a slightly positive net charge just below the surface and a slightly negative net negative charge just above the surface [54]. According to Tasker [108] there are three type of surface ionic or partly ionic crystal, the type1 neutral surface with an equal proportion of anion and cation in the plane, type2 charge surface with no dipole in the periodic perpendicular arrangement and type3 charge surface with a dipole in the periodic perpendicular arrangement. We use DFT in the surface calculation with the plane-wave basis set pseudo-potential code and it is necessary to embed a slab with two surfaces in a periodic supercell. Plane-wave method creates an artificial uniform electric field in the supercell vacuum region, in order to cancel the potential jump at the boundary by imposing periodic boundary condition on the electrostatic potential. The macroscopic artificial electrostatic field arising due to the imposed boundary condition can be corrected using the dipole correction which compensates for the artificial field in the vacuum region in the supercell [109, 110]. One of the methods used is to switch on LDIPOL-tag in VASP.

2.4.3 Bader analysis

Bader analysis is a useful tool for calculating the number of valence electrons associated with a particular ion in a periodic solid. An approach proposed by Bader [111], the method involves analysing the topological features of the electron density around an atom (or ion), which is then divided into Bader basins associated with each atom. Inside the Bader basin, the electron density is summed up and the Bader charge for each atom is determined. This technique provides an analysis of charge accumulation and depletion on periodic slab isosurface. Charge density analysis helps to understand the concentration of charge accumulation and depletion on the isosurface which is likely to reduce charge recombination and enhance easy charge transfer that produces a valuable result in assessing photoelectrochemical (PEC) material.

3

Computational Details

In this chapter, we outlined the aspect of density functional theory (DFT); many-body perturbation theory as discussed in chapter 2 and some mathematical aspects and show how these can be utilized in calculating the ground state and optical properties of crystal bulk systems. The chapter continues with surface modelling, where a periodic supercell surface is created with optimized crystal bulk (the extended two-dimensional system) and how the DFT and some mathematical aspect are used for structural optimization; calculations of: surface energy, average electrostatic vacuum potential, work function and band edge positions of the extended system.

3.1 DFT Calculations

All calculations for the bulk unit cells of A_2GeSe_4 (A = Mg, Ca, γ-Sr and Ba) were performed within the framework of density functional theory (DFT) as implemented in the Vienna *ab initio* Simulation Package (VASP) [83, 112]. VASP implements DFT based on pseudopotentials and plane-wave basis set, with projected-augmented-wave (PAW) [113, 114] formulation for the description of electron-ion interactions. The ground state energy was calculated within the Perdew-Burke-Ernzehof generalized gradient approximation (PBE) [69] and its variant optimized for solids, PBEsol [70], for the description of electron exchange-correlation energy and a plane wave cut-off energy of 520 eV. For A_2GeSe_4 (A = Mg, Ca, γ-Sr and Ba), unit cells were sampled with $2 \times 4 \times 6$, $6 \times 4 \times 4$, $8 \times 8 \times 4$ and $6 \times 6 \times 4$ kpoint meshes respectively using the Monkhorst-Pack scheme for

sampling the Brillouin zone. The energy converging criteria for electronic self-consistent iteration and ionic relaxation loop is set to 10^{-8} eV. Equilibrium structural optimizations were performed on the primitive cell of the structure. For the simulation of surface, we have used the periodic slab supercell approach consisting of A_2GeSe_4 (A = Mg, Ca, γ-Sr and Ba) unit cell layer infinite in the x and y direction and separated in z-direction by vacuum layers thick enough to eliminate the surface-surface interaction. Similarly to the bulk, all calculations are performed using the Generalized Gradient Approximation (GGA) variant optimized for solids PBEsol [70] chosen based on its accuracy in calculating the bulk materials ground states properties compared to experiment. Ionic relaxation of slab geometries were performed on a (1×1) supercell of A_2GeSe_4 (A = Mg, Ca, γ-Sr and Ba) cleaved in 100, 101, 110 and 111 low-index surface facets constructed from the optimized bulk unit cells using the automatic flow (AFLOW) package [115]. On the relaxed structure, the test was performed to ensure the convergence of total energy within (1 MeV per atom) with respect to the number of layers in the slab up to 9-15 layers and vacuum size to about 15 - 40 Å. Sufficient kpoints were generated using automatic flow (AFLOW) [115] that automatically generate kpoints and k-path for accurate bandstructure calculations. Gamma-centered kpoint grids sampling of $7\times5\times1$ for Mg_2GeSe_4, $6\times6\times1$ for Ca_2GeSe_4, $7\times7\times1$ for γ-Sr_2GeSe_4 and $5\times5\times1$ for Ba_2GeSe_4 respectively with plane-wave basis cutoff energy of 520 eV were used for ionic relaxation, convergence test, surface energy and bandstructure calculations. From the calculated KS bandstructure eigenvalues of the surface period slab unit cell, we locate the band gap center (BGC) half-way between the KS valence band maximum VBM and KS conduction band minimum CBM using the method of Janak's theorem, an extension of Perdew and Levy's proof for non-metallic systems. This method is used by Toroker et al. [116] in periodic surface calculations. Position of BGC relative to vacuum would be obtained by taking the energy difference of the calculated electrostatic potential in a vacuum region and the energy of the KS-BGC [116]. Band edge position relative to vacuum were computed from the combined bulk and surface calculations, the non-self consistent Green function quasiparticle G_0W_0+BSE band gap calculated from crystal bulk and BGC from surface geometry using the relation

$$E_{VBM} = BGC - \frac{1}{2}E_{\mathrm{g}}, \tag{3.1.1}$$

$$E_{CBM} = BGC + \frac{1}{2}E_{\mathrm{g}}. \tag{3.1.2}$$

where E_{g} is the quasiparticle G_0W_0+BSE band gap calculated from bulk unit cells calculations.

Similarly, the E_{VBM} and E_{CBM} absolute band edges are also calculated using the method of Mulliken's absolute electronegativity of atoms [117], the so-called (EN) model for the bulk semiconductor. Based on EN model, the E_{VBM} and E_{CBM} energy band edges can be calculated using the equations given by

$$E_{\mathrm{V}MB} = \chi - E_e + \frac{1}{2}E_{\mathrm{g}}, \tag{3.1.3}$$

$$E_{CBM} = E_{\mathrm{V}BM} - E_{\mathrm{g}}, \tag{3.1.4}$$

where χ is the Mulliken electronegativity. For ternary $A_xM_yQ_z$ electronegativity χ is geometric mean of electronegativities for constituent atoms [118, 119]. Employing the method used for binary compound, χ is calculated for ternary compound using equation $\chi = \left[\chi^x(\mathrm{A})\chi^y(\mathrm{M})\chi^z(\mathrm{Q})\right]^{\frac{1}{x+y+z}}$ [119], E_e is the energy of free electron hydrogen scale (4.5 eV) and E_{g} is the calculated bulk G_0W_0+BSE band gap.

The calculated valence band maximum and conduction band minimum positions are aligned relative to redox potential of reduction and oxidation of water at pH = 0 and 7 on standard hydrogen electrode (SHE) respectively.

3.2 Electronic structure

From the optimized structures, all electronic structure calculations were performed using four exchange-correlation functionals namely, the PBE-GGA [69], PBEsol [70], MBJ potential [76] and HSE06 [82] hybrid.

3.3 Calculations of structural properties

3.3.1 Cohesive energy and formation energy

The cohesive energy (E_{coh}) referred to as the binding energy, is the negative energy of substance (solid or liquid) evolved when crystalline solid is formed from infinitely separated atoms or energy required to break all the bonds associated with one of its

constituents molecules into neutral free atom at rest and finite separation. The formation energy (E_{form}) provide insight into the material fundamental aspect of phase equilibrium and stability. Within the DFT calculation cohesive energy is computed as the difference between total energy per atom of the bulk of crystal unit cell at equilibrium and energy of a free atom in its ground state [120, 121]

$$E_{\text{coh}} = E_{\text{bulk}} - \sum_{\text{A}}^{\text{N}} E_{\text{A}}, \tag{3.3.1}$$

where E_{A} is the atomic energy for each atom belonging to the bulk unit cell and N is the number of atoms in a bulk unit cell.

Similarly, the formation energy is calculated using the following equation as defined by [122],

$$E_{form}(A_xB_yC_z) = \frac{(A_xB_yC_z) - xE(A) - yE(B) - zE(C)}{x+y+z}, \tag{3.3.2}$$

where x, y z are the number of non or metallic atoms, $\text{A}_x\text{B}_y\text{C}_z$ is a compound total binding energy and E(A, B, C) is the binding energy per non or metallic atom.

The significance of computing the cohesive and formation energy is to determine the structural relative phase stabilities among the structures; the lower the cohesive energy the better the stability [123]. The more negative formation energy, the more energetically favourable stable are the constituent atoms mixed to formed stable compound [124].

3.3.2 Bulk modulus and its pressure derivative B′

In an *ab initio* calculation, the bulk modulus B is usually obtained from fitting the calculated energy-volume data to empirical forms of the equation of state (EOS) and evaluated at minimum [120]. A_2GeSe_4 compounds considered in this thesis are in orthorhombic and monoclinic symmetries, the energy-volume data are generated from full structural relaxation of a set of volume compressed or expanded unit cells [125]. The bulk modulus from standard definition is [120, 125] expressed as;

$$B_0 = -V_0\frac{\partial P}{\partial V} = -V_0\frac{\partial^2 E}{\partial V^2}, \tag{3.3.3}$$

where V_0 is the equilibrium volume obtained from the full structural relaxation, E the binding energy and the pressure $P = -\frac{\partial E}{\partial V}$ is obtained from the calculated energy-volume curve.

The pressure derivatives of bulk modulus theoretically from the equilibrium volume are given by

$$B_0' = \left.\frac{\partial B}{\partial P}\right|_{P=0} = \frac{1}{B_0}\left(V\frac{\partial}{\partial V}(V\frac{\partial^2 E}{\partial V^2})\right)\Big|_{V=0}. \tag{3.3.4}$$

3.3.3 Equation of state and lattice parameters

Using the equation of state (EOS) the relationship between pressure-volume-temperature (P,V,T) is established [126, 127]. EOS provides answers to some fundamental theories of solid state, it helps in evaluating thermodynamical properties of materials. Some empirical and analytical methods of EOS are proposed [126], including the method proposed by Birch-Murnaghan [128] and modelled approach by Born-Mayer and Buckingham. In this work, we used the third-order non-linear Birch-Murnaghan equation of state [128] which is found to be successful in approximating EOS of solid [129]. The Birch-Murnaghan equation of state at zero pressure is expressed as [126, 130].

$$E(V) = E_0 + \frac{9V_0B_0}{16}\left\{\left[\left(\frac{V_0}{V}\right)^{\frac{2}{3}} - 1\right]^3 B_0' + \left[\left(\frac{V_0}{V}\right)^{\frac{2}{3}} - 1\right]^2\left[6 - 4\left(\frac{V_0}{V}\right)^{\frac{2}{3}}\right]\right\}, \tag{3.3.5}$$

Where the E_0, V_0 and B_0 are the equilibrium energy, volume and bulk modulus at zero pressure respectively. Similarly, the volume-dependent pressure equation is given as stated by [126, 130]

$$P(V) = \frac{3B_0}{2}\left[\left(\frac{V_0}{V}\right)^{\frac{7}{3}} - \left(\frac{V_0}{V}\right)^{\frac{5}{3}}\right]\left\{1 + \frac{3}{4}\left(B_0' - 4\right)\left[\left(\frac{V_0}{V}\right)^{\frac{2}{3}} - 1\right]\right\}. \tag{3.3.6}$$

The fully relaxed structure from PBE and PBEsol are used to performed the EOS static calculation using the Blöchl tetrahedron correction to extract energy. From the obtained energy, least-square method with third-order Birch-Murnghan equation of state [128] the curve of energy as a function of volume is fitted, from which the lattice parameter are extracted and B_0, B_0', V_0, E_0 are also the fitting parameters [130].

3.4 Stability properties

Structural stability is studied both theoretically and experimentally, the DFT calculation of elastic constant and phonon dynamics provide a way to study the structural stability of crystalline structures. Stability of a structure can only be guaranteed under the condition satisfying the elastic and dynamical stability under the influence of external force and in the harmonic approximation. The condition that elastic constant satisfies Max Born [131] mathematical sufficient stability conditions and all the phonon modes have only the positive frequencies [132]. Here in this work, we consider an orthorhombic and monoclinic structures as previously stated, thus we discuss the computational detail of elastic and dynamic stabilities for the purpose of establishing or otherwise their structural stability.

3.4.1 Elastic stability

For bulk materials the study of elastic properties of solid matters (the elastic constant) have a great significance in the area of scientific research and technology [133]. The elastic constants describe the mechanical modulus of material, they provide very important information on the nature of forces, stability and stiffness of material. Structural stability or otherwise can be defined from the stability condition, and it is nothing but the positive definiteness of the macroscopic deformation that is expressed in the form of inequalities for the elastic constant [134]. In first principles calculation the single-crystal elastic constants are calculated from the energy-strain and stress-strain approaches. In this work, energy-strain approach: total energy as a function of appropriate lattice deformation is used to calculate the elastic constants $C_{ij}(i,j=1,2,3,4,5,6)$, and elastic constants are extracted from fitted curve of total energy ΔE versus strain δ. The elastic strain energy is given by $U=\frac{\Delta E}{V_0}=\frac{1}{2}\sum_i^6\sum_j^6 C_{ij}e_ie_j$, where ΔE is the energy difference , V_0 is the initial volume of unit cell, C_{ij} is the elastic constants and e_i, e_j is the strain.

Orthorhombic structure have nine independent elastic constant, for stable orthorhombic structure the independent elastic constants should satisfy the Born stability criteria [132, 135]:

$$\begin{aligned} C_{11}>0; & C_{11}C_{22}>C_{12}^2; \\ & C_{11}C_{22}C_{33}+2C_{12}C_{13}C_{23}- \\ & C_{11}C^2{}_{23}-C_{22}C^2{}_{13}-C_{33}C^2{}_{12}>0, \end{aligned} \tag{3.4.1}$$

Similarly, for stable monoclinic [135]

$$\begin{aligned}
&C_{11}>0; C_{22}>0; C_{33}>0; C_{44}>0; C_{55}>0; C_{66}>0;\\
&\quad \big[C_{11}+C_{22}+C_{33}+2(C_{12}+C_{13}+C_{23})\big]>0;\\
&\quad \big(C_{33}C_{55}-C_{35}^2\big)>0; \big(C_{44}C_{66}-C_{46}^2\big)>0;\\
&\quad \big(C_{22}+C_{33}-2C_{23}\big)>0;\\
&\quad \big[C_{22}(C_{33}C_{55}-C_{35}^2)+2C_{23}C_{25}C_{35}-C_{23}^2C_{55}-C_{25}^2C_{33}\big]>0;\\
&\quad \big\{2\big[C_{15}C_{25}(C_{33}C_{12}-C_{13}C_{23})+C_{15}C_{35}(C_{22}C_{13}-C_{12}C_{23})\\
&\quad + C_{25}C_{35}(C_{11}C_{23}-C_{12}C_{13})\big]-\big[C_{15}^2(C_{22}C_{33}-C_{23}^2)\\
&\quad + C_{25}^2(C_{11}C_{33}-C_{13}^2)+C_{35}^2(C_{11}C_{22}-C_{12}^2)\big]+C_{55}\mathrm{g}\big\}>0,
\end{aligned} \tag{3.4.2}$$

where $\mathrm{g}=C_{11}C_{22}C_{33}-C_{11}C_{23}^2-C_{22}C_{13}^2-C_{33}C_{12}^2+2C_{12}C_{13}C_{23}$.

Voigt-Reuss-Hill (VRH) approximation [136, 137, 138] is employed for the calculation of other mechanical parameter, for example, the bulk modulus B, shear modulus G and Young's Modulus E. From VRH approximation, Hill [138] is used in this thesis to extract the B, G and E, from the relations $B_H=\frac{1}{2}(B_R+B_V)$, $G=\frac{1}{2}(G_R+G_V)$ and $E_{\mathrm{H}}=\frac{9B_{\mathrm{H}}G_{\mathrm{H}}}{(3B_{\mathrm{H}}+G_{\mathrm{H}})}$. Poisson's ratio ν is also determined from relation $\nu=\frac{3B_{\mathrm{H}}-2G_H}{2(3B_{\mathrm{H}}+G_{\mathrm{H}})}$ [139, 140]. This relations statisfy the orthorhombic and monoclinic phases [135].

Quantifying the single crystal anisotropy index has very important implications in engineering science and crystal physics [141]. It describe single crystal elasticity behavior of been anisotropic or isotropic. Proper description of such anisotropic behavior has important implication in engineering science and crystal Physics. There are many anisotropy index evaluation approaches for single crystal which include one by Zener [142], Chuang-Buessem [141] and Ranganathan-Martin [143]. We use the universal anisotropy by Ranganathan which is the unification of both Zener and Chuang-Buessem approach given as $A^u=5\frac{G_V}{G_R}+\frac{B_V}{B_R}-6\geq 0$ to evaluate the single crystal anisotropy of A_2GeSe_4.

3.4.2 Dynamical stability

The knowledge of vibrational eigen-frequency (the phonon) of the crystalline lattice is fundamental in understanding the phase stability, phase transition and thermodynamics of crystalline materials [144]. In DFT the linear response and direct approach are the two preferred methods for phonon calculation [144, 145]. In this work, finite

displacement method a linear response approach to determine the force constant as implemented in PHONOPY code [146] were used to compute the phonon properties of A_2GeSe_4 (A = Mg, Ca, γ-Sr and Ba) within the harmonic approximation. All calculations are performed with $2 \times 2 \times 2$ supercell of A_2GeSe_4 containing 224 and 112 atoms for orthorhombic and monoclinic phase respectively using VASP code, the size of the supercell defined the phonon frequecies at k-points Brillouin zones.

In harmonic approximation the dynamic properties of materials are obtained by solving eigen value problem of the dynamic matrix $D(\mathbf{q})$ [145]

$$\sum_{\beta k'} D^{\alpha\beta}_{kk'}(\mathbf{q}) e^{\beta k'}_{\mathbf{q}j} = \omega^2_{\mathbf{q}j} e^{\alpha k}_{\mathbf{q}j}, \tag{3.4.3}$$

$$D^{\alpha\beta}_{kk'}(\mathbf{q}) = \sum_{l'} \frac{\Phi_{\alpha\beta}(0k, l'k')}{\sqrt{m_k m_{k'}}} e^{i\mathbf{q}.[\mathbf{r}(l'k') - \mathbf{r}(0k)]}, \tag{3.4.4}$$

where m_k is the mass of the atom k, $\mathbf{q}$ is the wave vector, and j is the band index. $\omega_{\mathbf{q}j}$ and $e_{\mathbf{q}j}$ give the phonon frequency and polarization vector of the phonon mode labelled by a set $\{\mathbf{q}, j\}$, respectively. Under the harmonic approximation, the structure is said to be dynamically stable if its all phonon modes have positive frequencies for all wave vectors [132].

The atomic contribution to the phonon dispersion total DOS of density of states is defined by $g(\omega) = \frac{1}{N}\sum_{qj} \delta(\omega - \omega_{qj})$, where N is the number of unit cells in the supercell.

3.4.3 Surface energy and stability

In our DFT calculation, the slab geometry is employed. The surface facets are described using the supercell composed of the thick periodic repeated layers of crystals, the so-called slab separated by vacuum layer in z-direction. The surface stabilities are defined relative to different formulated surface facets of crystal materials. This is an amount of energy required to produce a surface from an infinite crystal. In slab geometry surface energies are calculated from the optimized converged layer separated with sufficient vacuum using the relation [147]

$$\gamma = \frac{1}{2A}\left(E_{slab} - \frac{N_s}{N_b} E_{bulk}\right), \tag{3.4.5}$$

where E_{slab} is total energy of the supercell of number $N_{\rm s}$ repeated layers, E_{bulk} the total energy of the bulk unit cell containing the same number $N_{\rm b}$ of atoms, A is the surface area and number 2 account for the two surfaces within the supercell that are symmetric.

In order to compare the stability of different surfaces or different surface terminations, surface energy is considered [108]. Wulff shape construction provide a systematic way to classify mineral crystal characteristic shapes and sizes. In first principle, surface energy calculations are employed to explain experimental findings and the design of a better materials. In Wulff shape the crystalline shapes are polyhedron for which only faces parallel to Miller (hkl) planes are formed, its assumed that faces with relatively low surface energy will dominate the equilibrium shape. [148, 149, 150]. The surface energy of A_2GeSe_4 (A = Mg, Ca, γ-Sr and Ba) surfaces were computed from the slab supercell of 9-15 layer thickness low-index cleaved at (100), (101), (110) and (111) surface facets and their relative surface stability is compared.

3.5 Electronic Density of States (DOS)

The band structure is a useful quantity used in describing the electronic state of materials. The basic features of the band structure are analyzed by the electronic density of states (DOS) as a function of energy [54]. It takes account of all electronic state contribution in band structure for all possible positions in reciprocal space (kpoints) in a simple form [151]. The density of state is defined as the electronic state in a unit volume per unit energy. According to [54] the density of state $g(\varepsilon)$ for a given range of energy $(\varepsilon,\ \varepsilon + d\varepsilon)$ is given by the sum of over all states energy in that range. In the practical calculation for crystal, where the band structure calculations are over all the wave vector ε_k the density of states is computed from the relation given by,

$$g(\varepsilon) = \frac{2}{(2\pi)^3} \sum_n \int_{\varepsilon_{\mathbf{k}}^{(n)}=\varepsilon} \frac{1}{|\bigtriangledown_{\mathbf{k}} \varepsilon_{\mathbf{k}}^{(n)}|} dS_{\mathbf{k}}, \tag{3.5.1}$$

where the integral is over a surface in k-space in the Brillouin zone on which $\varepsilon_{\mathbf{k}}^{(n)}$ is constant and equal to ε and the vector $\bigtriangledown_{\mathbf{k}} \varepsilon_{\mathbf{k}}^{(n)}$ is normal $S_{\mathbf{k}}$ and having a magnitude with respect to change in $\varepsilon_{\mathbf{k}}^{(n)}$ in the normal direction. The root of denominator equation (3.5.1) is of the first order and therefore contribute a finite quantity to the integration over a smooth 2D surface represented by $S_{\mathbf{k}}$; and the roots introduces sharp features in

the function ($g(\varepsilon)$, which are called van Hove singularities [152, 54].

For the extended systems periodic in one or two dimensions, no special features are expected in the function $g(\varepsilon)$ except the widening or closing of band and gaps near the Fermi-level and the volume integral becomes surface integral, while the surface integral becomes the line integral [153].

3.6 Optical properties calculations

With the help of frequency dependent dielectric function, the optical properties of materials are determined. The dielectric function $\varepsilon(\omega) = \varepsilon_1(\omega) + i\varepsilon_2(\omega)$, provides important information about the optical properties of materials, its polarization response to external applied electric field and absorption of photons. The optical absorption spectra is obtained from the Bether-Salpeter Equation on top of the non-self consistent many-body Green's function G_0W_0 [154, 155, 156] calculations. The method includes excitonic effect in addition to the local field effect. For orthorhombic A_2GeSe_4 (A = Mg, Ca and γ-Sr) phase, the energy cutoff of 300 eV and plane-wave basis energy cutoff 180 eV for response function with 6960 number of bands (NBANDS) and 96 frequency grid points for the energy integration were used. For the monoclinic phase of Ba_2GeSe_4, the energy cutoff of 300 eV and plane-wave basis energy cutoff 180 eV for response function with 3480 NBANDS and 96 frequency grid points for the energy integration were used.

The real part $\varepsilon_1(\omega)$ of the dielectric function can be derived from the imaginary part $\varepsilon_2(\omega)$ by Kramers-Kronig transformation [157]. The knowledge of both the real and imaginary parts of the dielectric tensor allows the calculations of other important optical parameters such as the refractive index n(ω), extinction coefficient k(ω), optical reflectively R(ω), absorption coefficient $\alpha(\omega)$ and energy loss functions L(ω) can be calculated from the complex dielectric function $\epsilon(\omega)$ [158]

$$n(\omega) = \left[\frac{\varepsilon_1(\omega)}{2} + \frac{\sqrt{\varepsilon_1^2(\omega) + \varepsilon_2^2(\omega)}}{2}\right]^{\frac{1}{2}}, \tag{3.6.1}$$

$$k(\omega) = \left[\frac{\sqrt{\varepsilon_1^2(\omega) + \varepsilon_2^2(\omega)}}{2} - \frac{\varepsilon_1(\omega)}{2}\right]^{\frac{1}{2}}, \tag{3.6.2}$$

$$R(\omega) = \left|\frac{\varepsilon^{\frac{1}{2}}(\omega) - 1}{\varepsilon^{\frac{1}{2}}(\omega) + 1}\right|^2, \tag{3.6.3}$$

$$\alpha(\omega) = \frac{4\pi}{\lambda(\omega)}\left(\frac{\sqrt{\varepsilon_1^2(\omega) + \varepsilon_2^2(\omega)^2}}{2} - \frac{\varepsilon_1(\omega)}{2}\right)^{\frac{1}{2}}, \tag{3.6.4}$$

$$L(\omega) = \frac{\varepsilon_2(\omega)}{\varepsilon_1^2(\omega) + \varepsilon_2^2(\omega)}, \tag{3.6.5}$$

where $\lambda(\omega)$ in equation (3.6.4) is the free space wave length of light.

4

Results and Discussions

In section 1.3.1, we reviewed the method of synthesis and characterization of seleno-germanate A_2GeSe_4 (A = Mg, Ca, γ-Sr and Ba), here in this chapter we present the results and discussions on the bulk structural, mechanical, dynamical, electronic and optical properties and it's extended 2D structure, electronic, surface and photocatalytic properties based on the theoretical backgrounds (presented in Chapter 2) and computational details (described in Chapter 3)

4.1 Ground state and excited state properties

In this section, we present the results of our investigation of crystal bulk A_2GeSe_4 (A = Mg, Ca, γ-Sr and Ba) compound such as structural, mechanical and dynamical stabilities, electronic and optical properties. Some of the results we discuss here have been published [1]. The structures of orthorhombic A_2GeSe_4 (A = Mg, Ca and γ-Sr) phases and monoclinic phase Ba_2GeSe_4 as well as the Brillouin zones [115] are shown in Figure 4.1.

4.1.1 Structural Properties

The compounds Mg_2GeSe_4, γ-Sr_2GeSe_4, Ba_2GeSe_4 and Ca_2GeSe_2 are members of seleno-germanite A_2MX_4 (A = Earth-alkaline metals, M = group 14 elements and X = chalcogene atom) the chalcogenedometaletes. X-ray diffractometer and single crystal

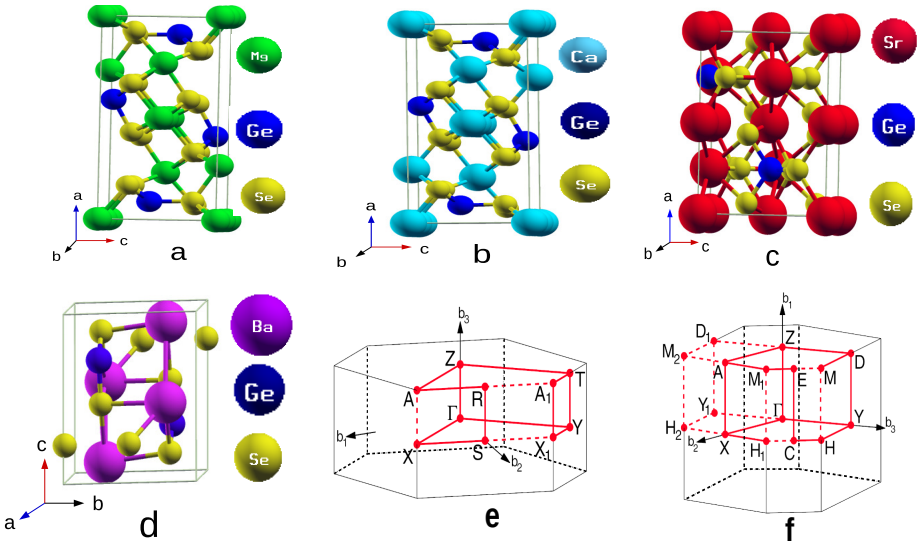

Figure 4.1: From left (a, b, c) the crystal structure of A_2GeSe_4 (A = Mg, Ca and γ-Sr) orthorhombic phase, (d) the Ba_2GeSe_4 monoclinic phase with space group $P2_1/m$ (No. 11) and (e, f) the Brillouin zone of the orthorhombic and monoclinic, lattice respectively.

x-ray structural studies of Mg_2GeSe_4 and γ-Sr_2GeSe_4 reveals that the compounds crystallize into an orthorhombic structures with space group Pnma (no. 64) and Ama2 (no. 40). They structure type of olivine Mg_2SiO_4 and Sr_2SnS_4 structure types respectively, at room temperature [38, 35]. Mg_2GeSe_4 is orthorhombic with experimental lattice parameters ($a = 13.50$ Å, $b = 7.851$ Å, $c = 6.366$ Å and angles α=β=γ=90^0), number of atoms per formular unit is cell $Z = 4$. Similarly, γ-Sr_2GeSe_4 reported to have experimetal lattice parameters ($a = 10.284$ Å, $b = 10.543$ Å, $c = 7.411$ Å and angles α=β=γ=90^0), number of atoms per formular unit cell is $Z = 4$. Mg_2GeSe_4 and Sr_2GeSe_4 each containing 28 atoms per unit cell. An X-ray powdered diffractogram also reveals the formation of stable Ba_2GeSe_4 crystallized in monoclinic structure, space group $P2_1/m$ a Sr_2GeS_4 structure type with experimental lattice parameters given as ($a = 6.9958$ Å, $b = 7.0938$ Å, $c = 9.1738$ Åand angles α=γ=90^0, $\beta = 109.135^0$), number of atoms per formular unit cell is $Z = 2$. [36]. In the case of Ca_2GeSe_4, no experimental synthesis has been reported, but formally the compound can be formed by substituting Si with Ge in the Ca_2SiSe_4 configuration, an olivine Mg_2SiO_4 structure type [53]. Our calculations [1] confirm that Ca_2GeSe_4 is stable in an orthorhombic structure with space group pnma (No. 62) and contains 28 atoms per unit cell. The ratio of the ionic radii r_A/r_M+r_X and types of chalcogen atom plays a role in defining the crystal structure of A_2MX_4 fam-

ily compounds, where small radii cations such as calcium (Ca) with ortho-germanates sulphate (GeS_4) are reported to crystallize mostly in the olivine type structure [35, 50].

In the choice of suitable approximation for the calculations of stuctures under study, we performed first the ground state energy calculation to optimize the structures using the Generalized Gradient Approximation (PBE) and its variants for solids PBEsol to calculate the lattice parameters, equilibrium volumes and binding energy of the structures under study. The obtained results are fitted to a 3^{rd}-order Birch-Murnaghan equation of state (EOS) function [159] to evaluate the values of equilibrium volume V_0 ($Å^3$), cohesion energy, bulk modulus (B_0) and its derivatives (B_0'). The calculated lattice parameters, formation energies, cohesive energies and optimized volumes from the optimized structures are shown in Table 4.1. The available experimental values are also given for comparison. Total energy versus volume curves are presented in Figure 4.2 (a) - (d). The calculated equilibrium volume using PBEsol functional gives values within about 1% less than the experimental values, while PBE overestimates the experimentally reported values by around 5%.

Table 4.1: Lattice constants (a, b and c), equibrium volume V_0, energy of formation E_f and energy of cohension E_{coh} for A_2GeSe_4 (A = Mg, Ca, γ-Sr and Ba), angle between a and b (β) in degree for Ba_2GeSe_4.

(a)Mg_2GeSe_4

Functional	a(Å)	b(Å)	c(Å)	$V_0(Å^3)$	E_f(eV/atom)	E_{coh}(eV/atom)
PBE	13.641	7.937	6.391	691.880	-0.444	-3.289
PBEsol	13.430	7.827	6.316	663.880	-0.411	-3.631
Exp.[a]	13.500	7.851	6.366	657.0	-	-

(b)Ca_2GeSe_4

Functional	a(Å)	b(Å)	c(Å)	$V_0(Å^3)$	E_f(eV/atom)	E_{coh}(eV/atom)
PBE	6.681	8.658	14.458	836.360	-0.864	-3.828
PBEsol	6.546	8.549	14.136	795.200	-0.814	-4.151

(c)γ-Sr_2GeSe_4

Functional	a(Å)	b(Å)	c(Å)	$V_0(Å^3)$	E_f(eV/atom)	E_{coh}(eV/atom)
PBE	10.479	10.756	7.485	843.640	-0.907	-3.787
PBEsol	10.253	10.481	7.374	792.400	-0.874	-4.126
Exp.[b]	10.284	10,543	7.411	803.530	-	-

(d)Ba_2GeSe_4

Functional	a(Å)	b(Å)	c(Å)	$V_0(Å^3)$	$\beta^{(0)}$	E_f(eV/atom)	E_{coh}(eV/atom)
PBE	7.204	7.240	9.292	454.960	108.520	-0.476	-3.610
PBEsol	7.022	6.986	9.150	424.200	109.078	-0.411	-3.95
Exp.[c]	6.996	7.094	9.174	430.110	109.135	-	-

[a]Ref. [38], [b]Ref. [35], [c]Ref. [36]

Calculated lattice parameters are consistent with experimental results. The cohesive energies (E_{coh}) and formation energies (E_{form}) listed in Table 4.1 are negative, which confirms that the compounds under study are energetically stable. Our calculated cohesive and formation energies become more negative with increasing atomic radii of the alkaline earth metals Mg, Ca and Sr for the orthorhombic phases suggesting that the ternary orthorhombic compounds A_2GeSe_4 (A = Mg, Ca and γ-Sr), become structurally more stable as the atomic mass of the alkaline earth atoms increase. To our knowledge, there is no available calculated data in literature found for A_2GeSe_4 (A = Mg, Ca, γ-Sr and Ba) for comparison. In general, the ground state parameters calculated so far with PBEsol are more consistent with experiment compared to results from PBE calculations. This is not surprising since PBEsol [70] was constructed to restore the gradient expansion for the exchange-correlation so as to improve the bulk structural properties of materials.

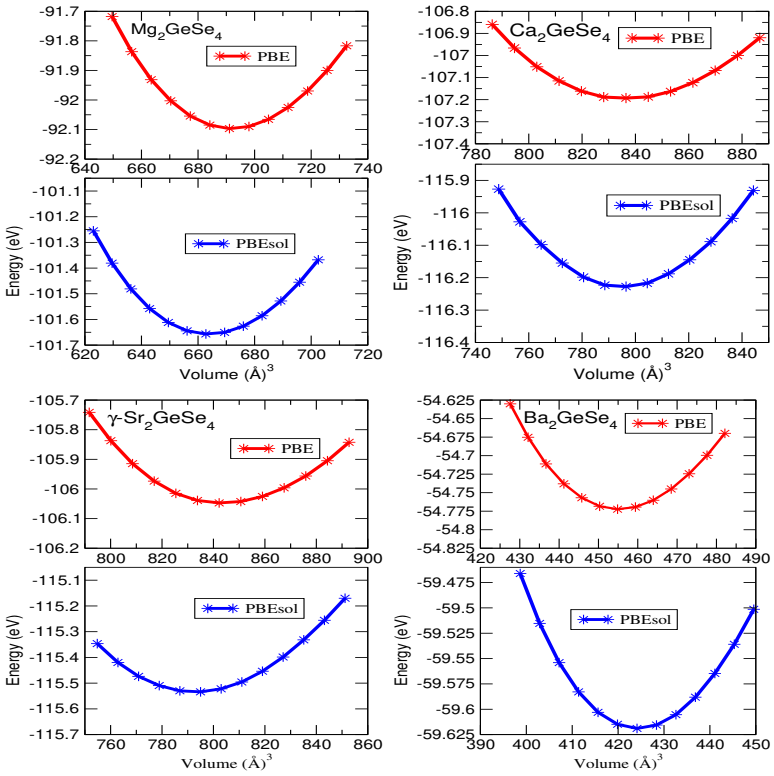

Figure 4.2: Energy versus volume (EOS) calculated using PBEsol and PBE for A_2GeSe_4 (A = Mg, Ca, γ-Sr and Ba) compound.

4.1.2 Mechanical Stability

The elastic constants (C_{ij}) are fundamental constants of solids that provide useful information about the link between mechanical and dynamical properties of crystals [132]. Important properties calculated using the elastic stiffness of materials, such as anisotropy factors, Poissons ratio (ν), bulk moduli (B), Young moduli (E) and shear moduli (G) provide important information on the nature of forces, bonding characteristic, stability and stiffness of a material. The elastic constants of A_2GeSe_4 (A = Mg, Ca, γ-Sr and Ba) are calculated using PBE and PBEsol; the results are depicted in Table 4.2 (a) - (d). Other calculated or experimental results to compare with are not available to our knowledge. The orthorhombic structures A_2GeSe_4 (A = Mg, Ca, γ-Sr) and monoclinic Ba_2GeSe_4 have 9 and 13 independent elastic constants respectively.

The calculated elastic coefficients listed in Table 4.2 (a) - (d) satisfy Equations (3.4.1) and (3.4.2) for orthorhombic structure type Born-Huang stability criteria and that of monoclinic structures discussed in subsection 3.4.1 respectively, indicating that the investigated materials are mechanically stable.

We deduced the order of the elastic constants $C_{11}>C_{33}>C_{22}$ and $C_{11}>C_{22}>C_{33}$ from Table 4.2 (a) - (c) in the orthorhombic phases Mg_2GeSe_4, Ca_2GeSe_4 and γ-Sr_2GeSe_4 respectively along the three principal axes. This order predicts the extent of resistance to linear compression in the $\langle 100\rangle$, $\langle 010\rangle$, $\langle 001\rangle$ directions, respectively. The calculated C_{22} for Mg_2GeSe_4 has a smaller value compared to C_{11} and C_{33}. Similarly, from Table 4.2 (d) for Ca_2GeSe_4 and γ-Sr_2GeSe_4, C_{33} is smaller compared to C_{11} and C_{22}. Thus, in the $\langle 010\rangle$-direction for Mg_2GeSe_4 and $\langle 001\rangle$-direction for Ca_2GeSe_4 and γ-Sr_2GeSe_4 are the most compressible. For monoclinic Ba_2GeSe_4 phase PBE predicted greater values of C_{11} and C_{22} than C_{33}, while PBEsol computed C_{11} and C_{33} greater than C_{22}. In addition, the elastic constants C_{44} and C_{66} provide useful information regarding indentation hardness of materials. High values of C_{44} and C_{66} means material have strong resistance to monoclinic shear distortion in the (100) plane and resistance to shear in $\langle 110\rangle$ direction respectively. The C_{44} and C_{66} values from Table 4.2 (d) for monoclinic Ba_2GeSe_4 are ≤ 9.07 and ≤ 16.36 respectively, similarly, for orthorhombic phases C_{44} and C_{66} listed in Table 4.2 (a) - (c) are ≤ 18.68 (GPa) and ≤ 19.65 (GPa) respectively. The relatively small value of C_{44} and C_{66} shows that both compounds are not very resistive to shear distortion.

It can also be seen from Table 4.2 (a) - (d) that all the calculated elastic constants

Table 4.2: (a) - (d) The calculated elastic constant (C_{ij}) in (GPa) from equation of state for orthorhombic A_2GeSe_4 (A = Mg, Ca, γ-Sr Ba) and monoclinic Ba_2GeSe_4, respectively.

(a)Mg_2GeSe_4

Functional	C_{11}	C_{12}	C_{13}	C_{22}	C_{23}	C_{33}	C_{44}	C_{55}	C_{66}
PBE	101.22	21.07	22.52	62.38	28.46	65.50	19.65	18.38	16.96
PBEsol	111.19	26.26	25.29	69.61	32.33	70.77	19.20	18.77	17.72

(b)Ca_2GeSe_4

Functional	C_{11}	C_{12}	C_{13}	C_{22}	C_{23}	C_{33}	C_{44}	C_{55}	C_{66}
PBE	65.54	25.00	23.89	44.53	27.43	36.88	15.62	9.60	16.37
PBEsol	74.44	31.75	30.21	48.31	33.83	41.23	14.60	10.64	18.68

(c)γ-Sr_2GeSe_4

Functional	C_{11}	C_{12}	C_{13}	C_{22}	C_{23}	C_{33}	C_{44}	C_{55}	C_{66}
PBE	53.34	14.14	25.35	40.36	15.51	40.27	13.23	12.69	10.93
PBEsol	64.47	14.68	26.27	41.68	14.52	41.48	15.19	14.27	12.16

(d)Ba_2GeSe_4

Functional	C_{11}	C_{12}	C_{13}	C_{15}	C_{22}	C_{23}	C_{25}	C_{33}	C_{35}	C_{44}
PBE	48.00	14.23	13.49	-0.70	40.65	19.93	8.75	38.52	0.18	7.93
PBEsol	56.03	13.61	15.07	0.06	40.17	21.72	14.05	50.36	-0.63	9.07

Functional	C_{46}	C_{55}	C_{66}
PBE	2.10	15.62	14.25
PBEsol	3.66	19.35	16.36

sets for othorhombic phases decrease in magnitude from Mg_2GeSe_4 to Ca_2GeSe_4 to γ-Sr_2GeSe_4 and the trend continued with monoclinic Ba_2GeSe_4 phase having the smaller sets elastic constants. This indicates a decrease in stiffness of these materials against external stress with increasing atomic mass (radius) of the earth-alkaline cation atom. For the monoclinic Ba_2GeSe_4, the PBE predicts negative value for C_{15} and PBEsol for C_{35} respectively suggesting that normal or shear stress associates with an opposite shear strain to reduce the total strain energy

The bulk modulus B_0 and its derivative B_0', determined by fitting the total energy Birch-Murnaghan equation of state [159], and the one using Voight-Ruess-Hill (VRH) [136, 137, 138] calculated from C_{ij} for comparison, are depicted in Table 4.3 (a) - (d). Similarly, Young's modulus (E), shear modulus (G) and Possion's ratio (ν) calculated using the (VRH) approximation, B/G ratio and universal anisotropy factor (A^U) are unitless also are listed in Table 4.3 (a) - (d).

The bulk modulus is a measure of resistance to the volume change by applied pressure,

Table 4.3: (a) - (d) The calculated mechanical parameters, the bulk modulus B_0 and its derivative B' from EOS fittings, bulk modulus B_V, B_R, B_H and shear G_H, Young's E_H modulus in (GPa) using VRH-approximations, the Poission's ratio ν, ratio B/G and the universal anisotropy A^u for orthorhombic A_2GeSe_4 (A = Mg, Ca, γ-Sr Ba) and monoclinic Ba_2GeSe_4 respectively.

(a)Mg_2GeSe_4

Functional	B_0	B'_0	B_V	B_R	B_H	G_H	E_H	ν	B/G	A^u
PBE	41.76	4.56	41.47	40.43	40.96	20.72	53.20	0.28	1.98	0.40
PBEsol	45.63	4.60	46.59	45.41	46.00	21.45	55.74	0.30	2.14	0.44

(b)Ca_2GeSe_4

Functional	B_0	B'_0	B_V	B_R	B_H	G_H	E_H	ν	B/G	A^u
PBE	32.31	4.07	33.29	31.83	32.56	12.14	32.39	0.33	2.68	0.83
PBEsol	33.28	1.89	40.55	39.25	39.90	11.43	31.30	0.37	3.37	1.72

(c)γ-Sr_2GeSe_4

Functional	B_0	B'_0	B_V	B_R	B_H	G_H	E_H	ν	B/G	A^u
PBE	26.35	6.36	27.79	26.59	27.19	12.70	32.98	0.30	2.09	0.25
PBEsol	30.78	4.64	28.73	26.89	27.81	14.16	36.38	0.28	1.96	0.29

(d)Ba_2GeSe_4

Functional	B_0	B'_0	B_V	B_R	B_H	G_H	E_H	ν	B/G	A^u
PBE	23.49	6.08	24.72	24.17	24.44	11.89	30.64	0.29	2.06	0.94
PBEsol	28.01	5.16	27.49	24.62	26.05	13.29	34.08	0.28	1.96	1.96

whereas the shear modulus is a measure of resistance to the reversible deformation upon shear stress [135]. Young's modulus is a measure of resistance to linear stress. The ratio B/G evaluates whether the material is ductile or brittle, whereas, the Poisson's ration (ν) provides information on the nature of bonding forces and volume compressibility of material. ν takes values between -1<ν<0.5 [160, 161], although material with negative Poisson's is not known [161]. The values of bulk moduli B_0 from EOS and that calculated using VRH approximations are in good agreement indicating that there are good structural atomic relaxation positions which have an influence on the elastic constant values. The values are also quite small, less than 50 (GPa), indicating that the compounds are relatively soft materials. The values of bulk modulus and Young's moduli are relatively low indicating that the materials under study are soft and flexible respectively.

The elastic anisotropy value is determined using the universal anisotropy (A^u) equation, a generalization of Zener anisotropy index, from Reference [143]. The deviation of A^u from zero defines the extent of elastic anisotropy. The calculated values of A^u are 0.399, 0.834, 0.251 and 1.963 for A_2GeSe_4 (A = Mg, Ca, γ-Sr and Ba) respectively, as listed

in Table 4.3 (a) - (d). All compounds are anisotropic material and the monoclinic Ba_2GeSe_4 phase is more anisotropic in nature. The Poisson's ratio ν calculated from VHR approximation takes a value between 0.28 to 0.37 for A_2GeSe_4 (A = Mg, Ca, γ-Sr and Ba) respectively, indicating that the compounds have central forces and are ionic materials, with dominant ionic contribution to inter-atomic bondings. Our calculated ratio B/G value is $\geq$ 1.976 for Mg_2GeSe_4, Ca_2GeSe_4, Sr_2GeSe_4 and Ba_2GeSe_4 and are greater than 1.75 which is the benchmark value. Therefore, all these compounds are ductile in nature with reference to Pugh's ratio $B/G>$ 1.75 for ductile material [162].

4.1.3 Dynamical Stability

The study of vibrational properties of crystals provides useful information about the macroscopic properties like specific heat, sound velocity and thermal properties. It also determines whether the compounds are dynamically stable. We use a finite displacement method [144, 163] to determine the force constants as implemented in the PHONOPY code [146] to study the dynamic properties. The computed band structure, total and partial density of state (TPDOS) of a phonon dispersion along the high symmetry directions for A_2GeSe_4 (A = Mg, Ca, γ-Sr and Ba) are shown in Figure 4.3 and 4.4. The A_2GeSe_4 (A = Mg, Ca and γ-Sr) orthorhombic phases have twenty-eight atoms per unit cell, which give rise to eighty-four phonon branches of which three are acoustic modes and eighty-one optical modes, which are shown in Figure 4.3 and 4.4. In the monoclinic Ba_2GeSe_4 phase with 14 atoms in a unit cell there are 42 phonon branches, of which 3 are acoustic and 39 are optical modes as presented in Figure 4.4. There are no negative frequencies seen along the high symmetry kpoints of the phonon spectra shown in Figure 4.3 and 4.4, hence A_2GeSe_4 compounds are dynamically stable. From the phonon dispersion curves of Mg_2GeSe_4, γ-Sr_2GeSe_4 and in Ba_2GeSe_4, flat bands are observed along almost the Brillouin zone between 5 to 6 THz. The flat band regions are indicative of localization [164].

In Figure 4.3 and 4.4 (right), is the total and projected density of states (TPDOS) contributions of individual elements to phonon vibrations of A_2GeSe_4 compounds. The projected density of state (PDOS) for Mg_2GeSe_4 and Ca_2GeSe_4 Figure 4.3 the lower modes frequencies from 0 to 5 THz have contributions from Mg, Ca, Ge and Se atoms respectively, with a dominant contribution from Se atom in the acoustic modes. Ca, Ge and Se contributions are seen for Ca_2GeSe_4 with Se giving the dominant contribution in

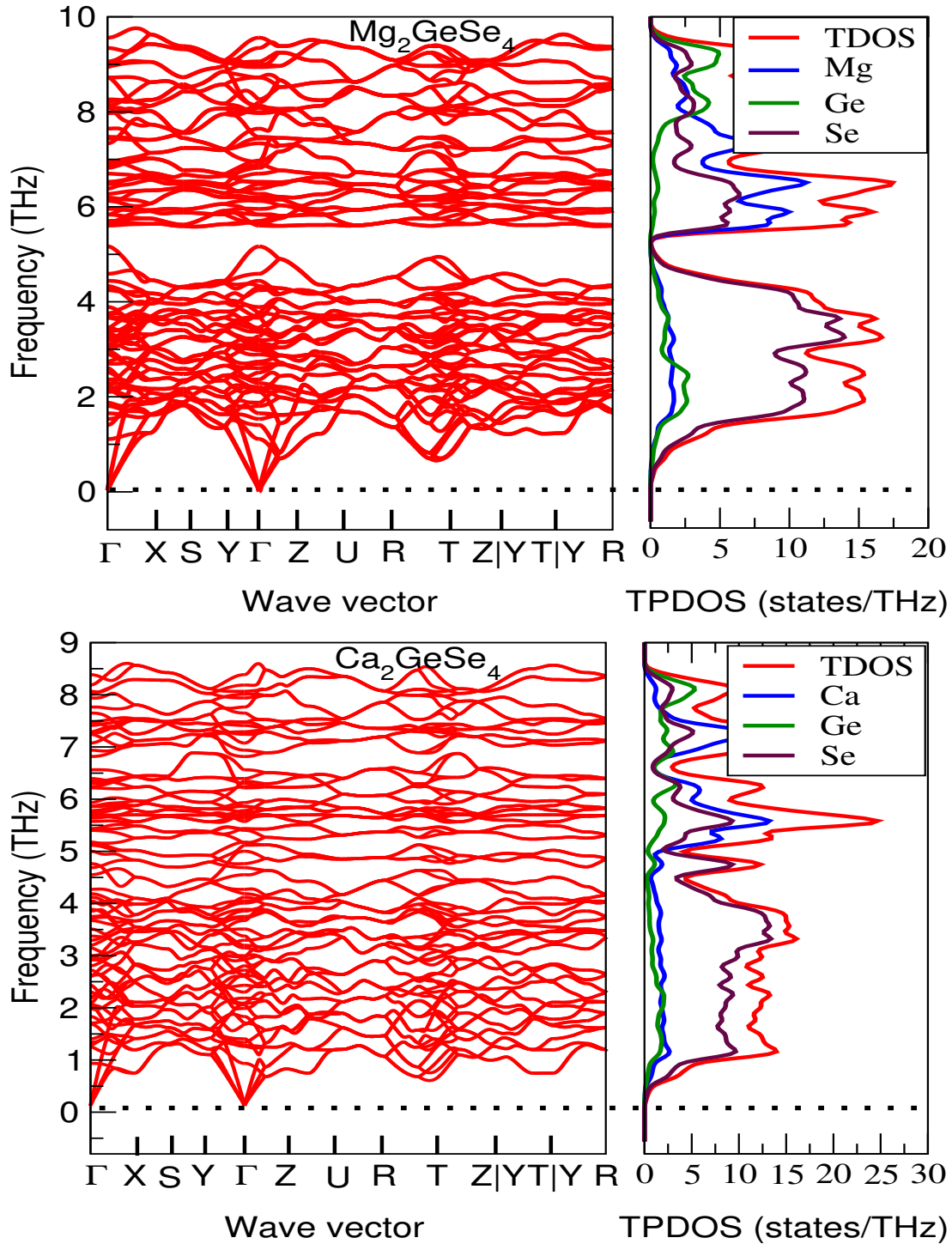

Figure 4.3: Calculated phonon dispersion curve along high symmetry kpoints, total and partial density of states (TPDOS) for A_2GeSe_4 (A = Mg and Ca) compound.

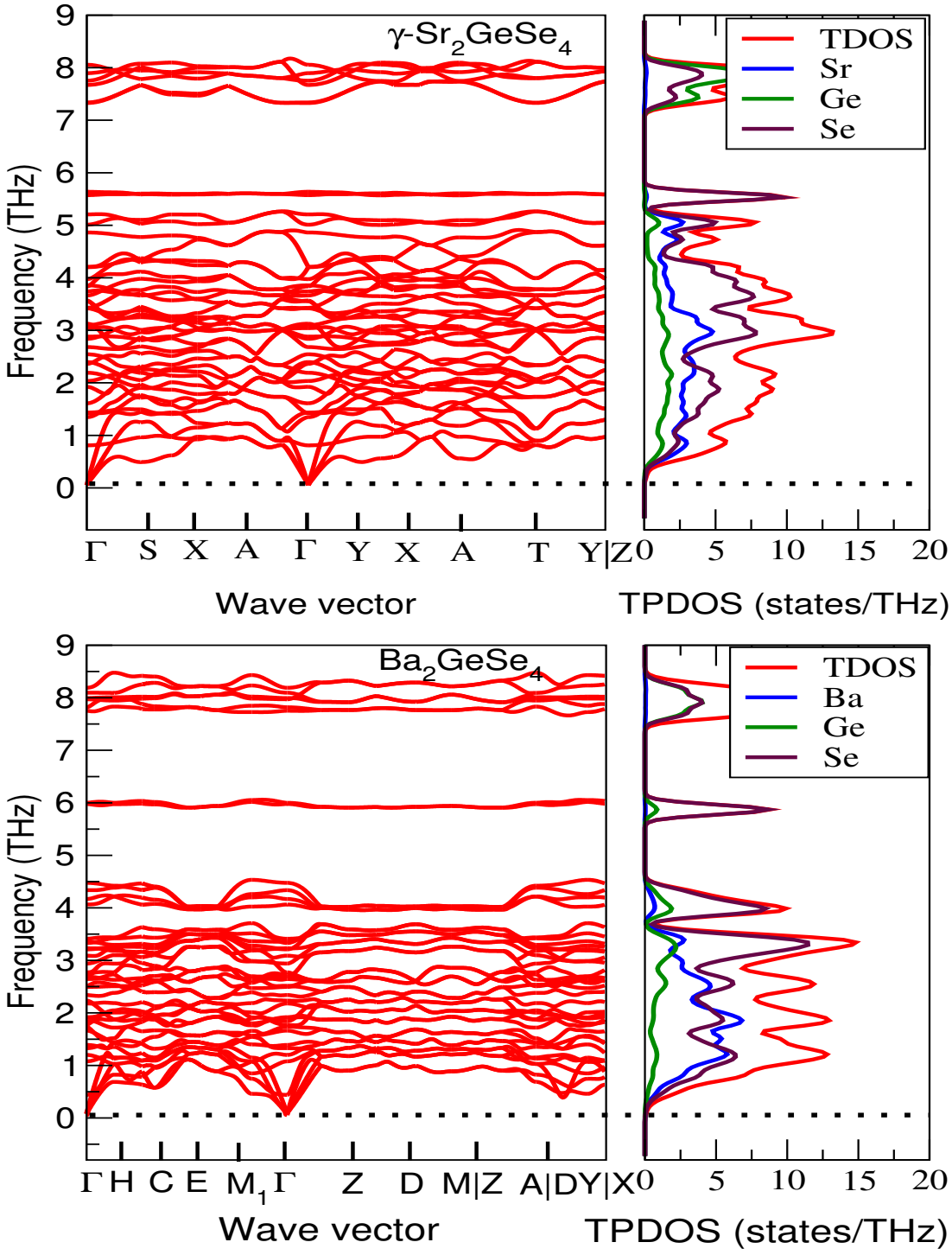

Figure 4.4: Calculated phonon dispersion curve along high symmetry kpoints, total and partial density of states (TPDOS) for A_2GeSe_4 (A = γ-Sr and Ba) compound.

the acoustic modes and some part of optical modes. While for γ-Sr_2GeSe_4 and Ba_2GeSe_4 with heavy alkaline atoms, also presented from right Figure 4.4, the characteristic of phonon dispersion from the projected density of states have Sr, Ba, Ge and Se atoms contributions, with the lower frequencies of acoustic mode from 0 to 2 THz dominated by vibrations of hybridization of Sr, Ba and Se atoms respectively.

4.1.4 Electronic Properties

In this thesis, the DFT electronic properties of A_2GeSe_4 (A Mg, Ca, γ-Sr and Ba) were studied for the PBEsol [70] optimized structures. However, since this approximation is expected to underestimate the band gap [165], we also used the semi-local MBJ potential [76] with basic generalized Kohn-Sham method [166] which approximates the derivative discontinuity of the exact exchange-potential for the bandstructure calculation. MBJ, on average, reproduces band gaps with about 10% error compared to experiment [76]. A drawback of MBJ is that it gives an approximation for the exchange-correlation potential without a corresponding exchange-correlation functional and cannot be used for structural optimization. We also estimated the band gap using the hybrid functional (HSE) and Green's function (G_0W_0) approximation, although it is computationally more demanding to implement than MBJ, but gives better estimates of the band gap than local and semi-local approximations to the exchange-correlation functional. Formally the most promising approach to estimate the fundamental gap with limited computational demand is the non-self consistent quasi-particle approximation, the so-called G_0W_0 approximation, with underlying KS-DFT input, is used [167, 168].

Figure 4.5 and 4.6 shows the combined band structure between -4.0 and 4.0 eV energy range along the high symmetry direction in Brillouin zone for PBEsol and MBJ with total (TDOS) and partial (PDOS) density of state for MBJ for A_2GeSe_4 (A = Mg, Ca, γ-Sr and Ba) compounds. Figure 4.5 and 4.6 (left) shows the band structures calculated using the PBEsol functional and MBJ potential. From the calculated band structures, it is evident that PBEsol functional under-estimation gap, while MBJ potential open the energy gap of the compounds under study. Similarly, from MBJ potential band structure diagrams, Figure 4.5 shows that Mg_2GeSe_4 and Ca_2GeSe_4 have indirect band gaps (E_g) of 2.29 and 2.11 eV, with valence band maximum (VBM) at Γ and conduction band minimum (CBM) between Γ - X, respectively. Also,from Figure 4.6 γ-Sr_2GeSe_4 and Ba_2GeSe_4 are shown to have a direct band gap transition of 2.51 and 2.26 eV at

the Γ point.

Computed band gaps and available experimental values are listed in Table 4.4 (a) - (d) for comparison. The calculated fundamental band gaps from G_0W_0 are 2.95, 2.53, 3.09 and 2.53 eV for orthorhomic Mg_2GeSe_4, Ca_2GeSe_4, Sr_2GeSe_4 and monoclinic Ba_2GeSe_4 respectively. To our knowledge there is no other available theoretical calculation to compare our work with. Compared to the available experimental gap data for Mg_2GeSe_4, our calculated G_0W_0 fundamental gap listed in Table 4.4 (a) is larger than the experimentally estimated optical gap of 2.02 eV [38]. This is consistent with our expectation that the fundamental gap is larger than the optical gap which require for the vertex correction [169, 170]. The MBJ and HSE computed fundamental gaps compare favorably between 11-26% larger; it is traditional with MBJ and HSE computed gaps to underestimate or overestimates relative to experimental gap by 0.1 to 0.2eV or 2% to 10% [76, 171]. However, for Ca_2GeSe_4 and γ-Sr_2GeSe_4 calculated band gaps E_g, there are no reported theoretically calculated and experimentally measured band gaps, for Ba_2GeSe_4 there are no experimental band gap to our knowledge for comparison.

To further explore the physical properties of these class of seleno-germanates compounds. We discuss extensively, the density of state (DOS), the total density of state (TDOS) and projected density of state (PDOS). They provide significant information in addition to the band structures. From the results shown in Figure 4.5 from right is a calculated TDOS and PDOS using MBJ potential. It can be observed that for Mg_2GeSe_4, the valence band maximum (VBM) is dominated by the contribution from Se-4p and the conduction band minimum (CBM) has a contribution from Ge-4s, Se-4p. Similarly, for Ca_2GeSe_4 in Figure 4.5 the VBM has a strong contribution from Se-4p and Ge-4p contribute far away from VBM, while Se-4p and Ge-4s strongly contributed to CBM. Noticeable from seleno-germanate A_2GeSe_4 compounds with one coordination environment unit of polyhedral A_2Se_6 with tetrahedral $GeSe_4$ like Mg_2GeSe_4 and Ca_2GeSe_4 the top of valence band VBM are composed of p orbital of Se which acts as donor atom. While the bottom of conduction bands CBM are composed of the dominant contribution of p and s orbitals of Se and Ge atoms respectively, this contribution are mainly from Ge-Se bonding making the tetrahedral $GeSe_4$ coordination. This tetrahedral $GeSe_4$ is reported to dictate the nature of the band gaps of seleno-germanates compounds [38, 37]. This is consistent with other calculations performed by Wu et al. [38, 37] on Mg_2GeSe_4 and thio-germanates Ba_2GeS_4. They reported that the bottom of CBM is dominated by Se, S and Ge orbitals, and accordingly that tetrahedral $GeSe_4$ and

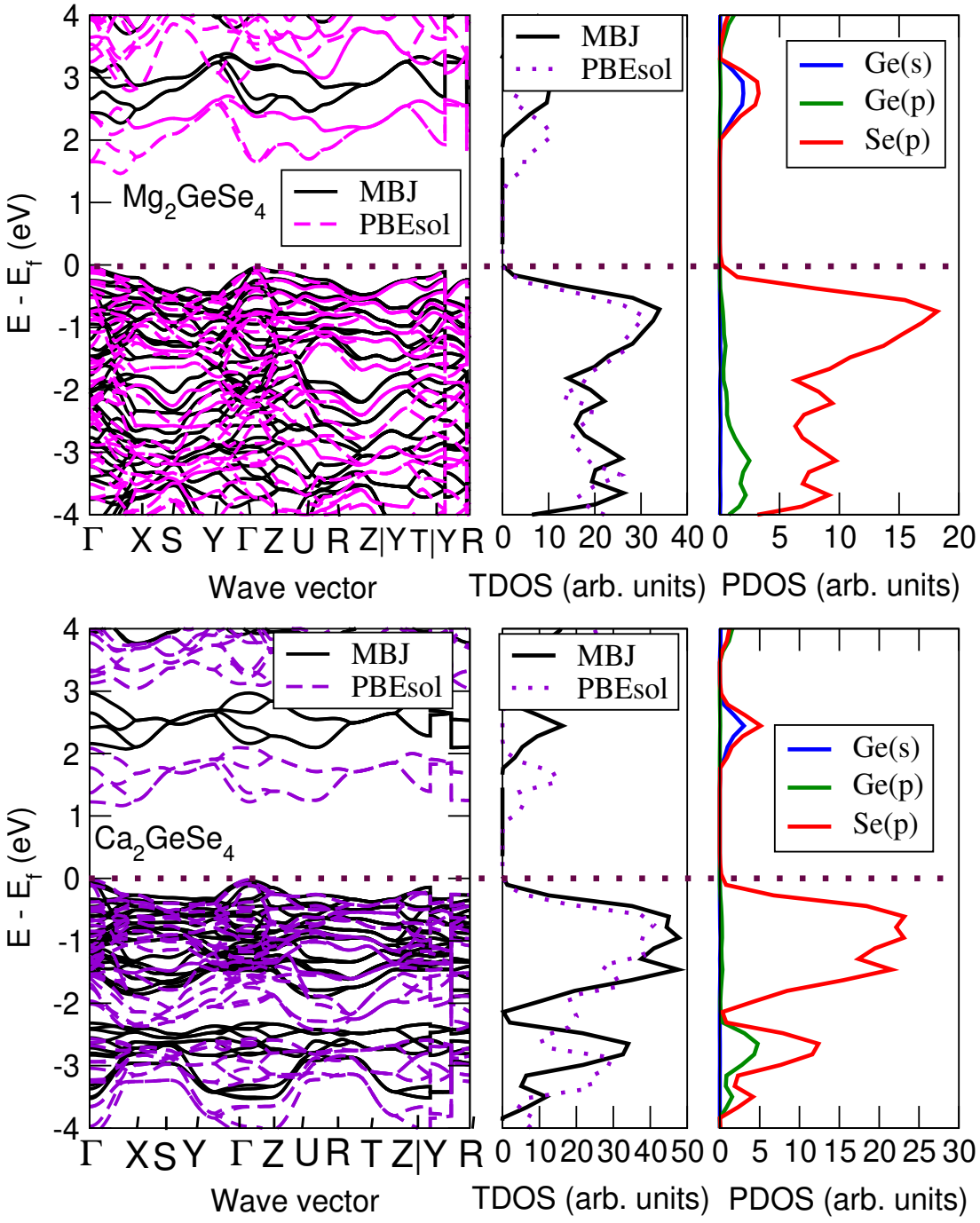

Figure 4.5: Electronic bandstructures calculated using PBEsol and mBJ, total (TDOS) and projected (PDOS) density of state compared along high symmetry points for A_2GeSe_4 (A = Mg and Ca) compounds, black solid line and violet dotted line represent the mBJ and PBEsol band structure respectively.

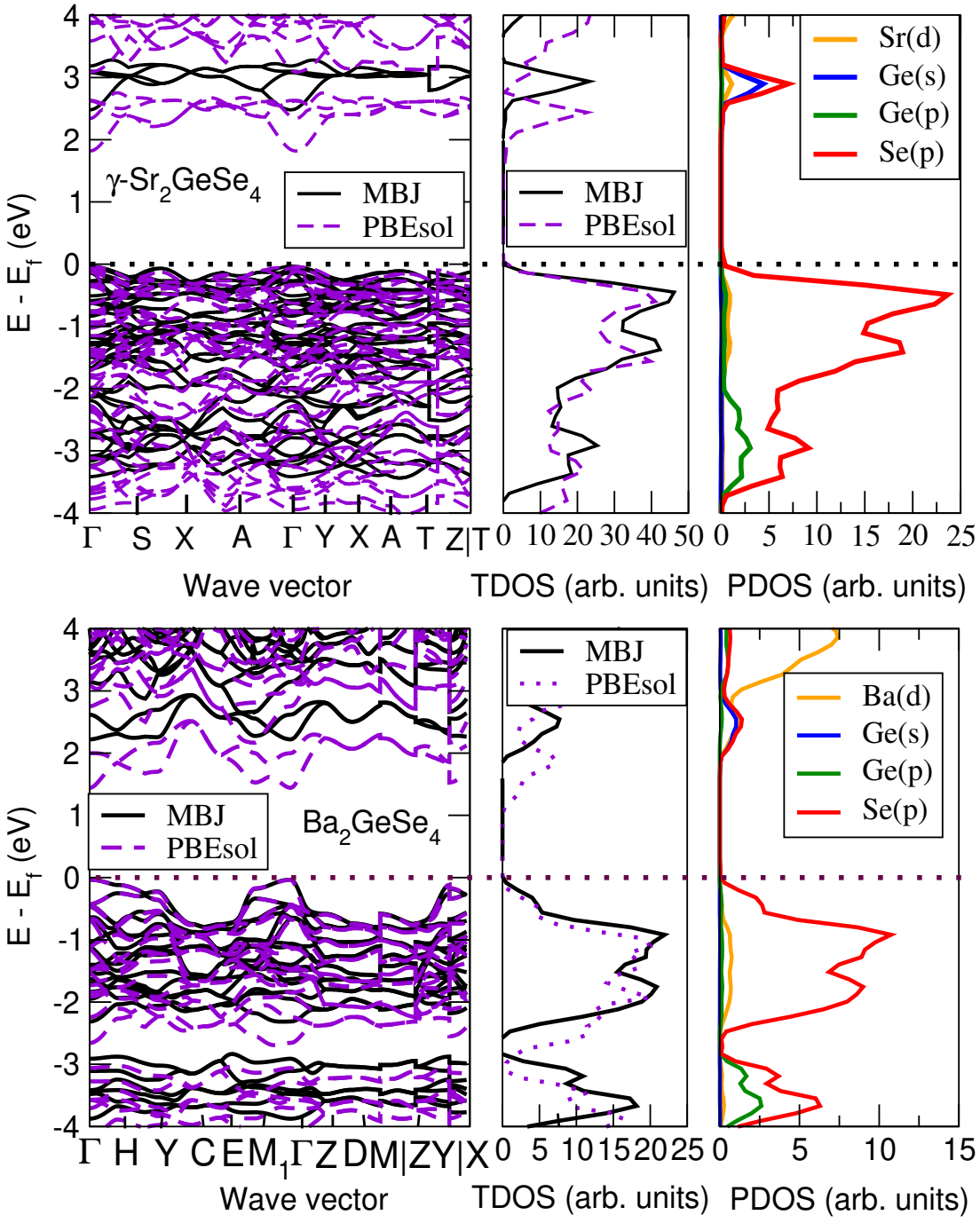

Figure 4.6: Electronic bandstructures calculated using PBEsol and mBJ, total (TDOS) and projected (PDOS) density of state compared along high symmetry points for A_2GeSe_4 (A = γ-Sr and Ba) compounds, black solid line and violet dotted line represent the mBJ and PBEsol band structure respectively.

GeS_4 determines the energy band gap. Furthermore, for the orthorhombic γ-Sr_2GeSe_4 and monoclinic Ba_2GeSe_4 a new variant of seleno-germanate with 2 coordination environment units with tetrahedral $GeSe_4$, the TDOS and PDOS are presented in Figure 4.6 from right.

For γ-Sr_2GeSe_4 with seven and eightfold A_2Se_n coordination with tetrahedral $GeSe_4$, the bottom of conduction band CBM is dominated by contribution of Se-4p, Ge-4s and Sr-3d and the top of valence band VBM is dominated by contribution from Se-4p atom. Similarly, for Ba_2GeSe_4 with eight and ninefold polyhedral A_2Se_n coordination with tetrahedral $GeSe_4$, the bottom of the conduction band CBM is dominated by the hybridization of Ba-3d, Ge-4s and Se4p orbitals, while the VBM is localized by Se-4p orbital. A_2GeSe_4 (γ-Sr and Ba) structures are defined by two coordination environments of mixed seven, eight and nine folds Sr-Se, Ba-Se coordinations with the usual $GeSe_4$ tetrahedral. Their conduction band minimum is defined by the polyhedral coordination environments Sr-Se and Ba-Se together with the tetrahedral $GeSe_4$ coordination. Consequently, the polyhedral Sr-Se, Ba-Se and tetrahedral $GeSe_4$ coordination units determine the band energy of these new variants seleno-germanates compounds. Finally, from our calculation of electronic structure from DFT hybrid functional and optical properties using the G_0W_0+BSE, A_2GeSe_4 (A = Mg, Ca, γ-Sr and Ba) are seen to have indirect and direct band gaps between 2.05 - 2.93 eV.

Table 4.4: (a) - (d) Calculated and reported experimental electronic band gap for A_2GeSe_4 (A= Mg, Ca, γ-Sr and Ba) compound.

(a)Mg_2GeSe_4

Method	PBEsol	MBJ	HSE06	G_0W_0	BSE			Exp.[38]	Theory [38]
					a	b	c		
Band gap (eV	1.50	2.29	2.73	2.95	2.60	2.58	2.82	2.02	1.57

(b)Ca_2GeSe_4

Method	PBEsol	MBJ	HSE06	G_0W_0	BSE			Exp.	Theory
					a	b	c		
Band gap (eV)	1.18	2.11	2.36	2.53	2.30	2.37	2.30	-	-

(c)γ-Sr_2GeSe_4

Method	PBEsol	MBJ	HSE06	G_0W_0	BSE			Exp.	Theory
					a	b	c		
Band gap (eV)	1.86	2.51	2.81	3.09	2.92	2.93	2.86	-	-

(d)Ba_2GeSe_4

Method	PBEsol	MBJ	HSE06	G_0W_0	BSE			Exp.	Theory [36]
					a	b	c		
Band gap (eV)	1.46	2.26	2.66	2.53	2.47	2.05	2.66	-	1.70

4.1.5 Optical properties

The optical properties of the seleno-germanates A_2GeSe_4 (A = Mg, Ca, γ-Sr and Ba) compounds were investigated to further support the electronic band structure data for a clear understanding of their potential applications. The dielectric properties plays roles in providing the actual nature of material and pictures of their uses, which generally described the nature of photon interaction with an electron in a system described by many-body perturbation theory of the ground-state electronic state. The imaginary part $\varepsilon_2(\omega)$ describes the optical coupling between occupied and unoccupied electronic states and the absorption of electromagnetic radiation [172], and the real part $\varepsilon_1(\omega)$ described the dispersion of photon by the material. All the calculation of optical properties in this work are performed with BSE on top of G_0W_0 with starting Kohn-Sham eigenvalues and to the best our knowledge this is the first time A_2GeSe_4 (A = Mg, Ca, γ-Sr and Ba) optical properties calculation performed using G_0W_0+BSE is being reported.

Our computed dielectric constants the real and imaginary, absorption spectra are from the absorption coefficient, and the refractive index, reflectivity and energy loss calculated from the dielectric functions. The DFT calculated optical properties are presented in Figure 4.7 - 4.10. The calculated imaginary ε_2 (ω) spectra in the energy range of 0 - 8 eV are dominated by some resonance exciton states, describing optical transitions integrated over the Brillouin zone. These contributions from each electronic transition from occupied top valance band to the empty bottom conduction band are the origin of different peaks and features shown in spectra. We can see that the imaginary spectra are displayed in 3 diagonal $a-$, $b-$ and $c-$ directions. The onset absorption spectral peaks of imaginary spectra depicted in Figure 4.7 - 4.10, when compared are consistent with our bandstructure calculations. The onset transitions peaks in absorption spectra are seen at 2.68, 2.40, 3.28 and 2.17 eV energies for A_2GeSe_4 (A = Mg, Ca, γ-Sr and Ba) respectively. The computed real dielectric function $\varepsilon_1(\omega)$ dispersion spectra are depicted in Figure 4.7 - 4.10, they show a considerable anisotropy behavior for the A_2GeSe_4 compounds in $a-$, $b-$ and $c-$ directon. Our calculated static real dielectric constant $\varepsilon_1(0)$ which is related to the polarizability of materials, along the crystallograpic direction $\varepsilon_1^a(0)$, $\varepsilon_1^b(0)$ and $\varepsilon_1^c(0)$ for Mg_2GeSe_4, Ca_2GeSe_4, γ-Sr_2GeSe_4 and Ba_2GeSe_4 respectively, are listed in Table 4.5. Our calculated $\varepsilon_1(0)$ values obey the Pen model [173] equation $\varepsilon_1(0) \approx 1 + (\hbar\omega_p/E_g)^2$ which is band gap dependent, where $\varepsilon_1(0)$ is inversily proportional to bang gap E_g. Thus, as band gap increases the $\varepsilon_1(0)$

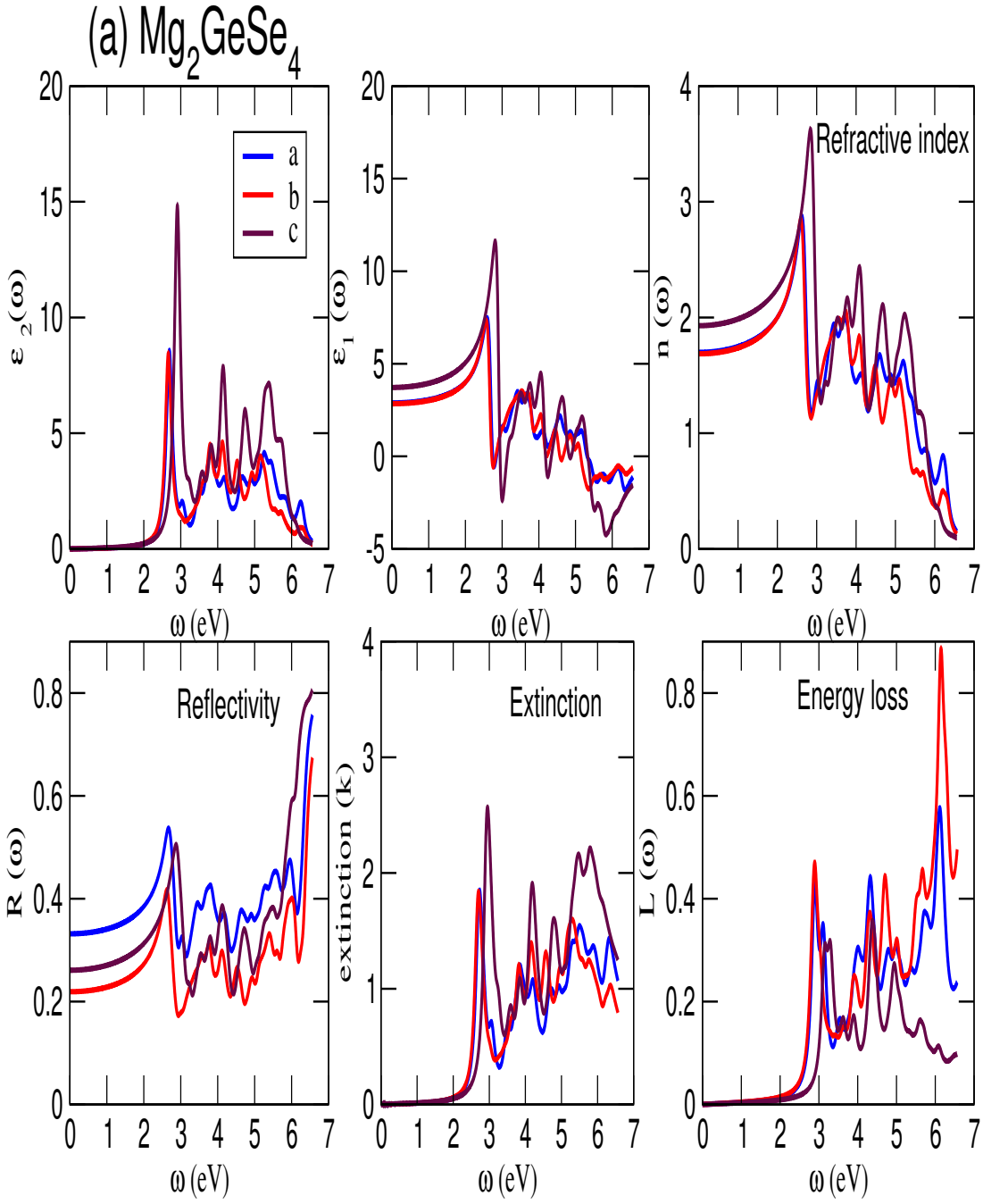

Figure 4.7: Calculated optical functions the imaginary ε_2 (ω) and real ε_1 (ω) dielectric constants, the refractive index, reflectivity, extinction and energy loss for Mg_2GeSe_4 compound.

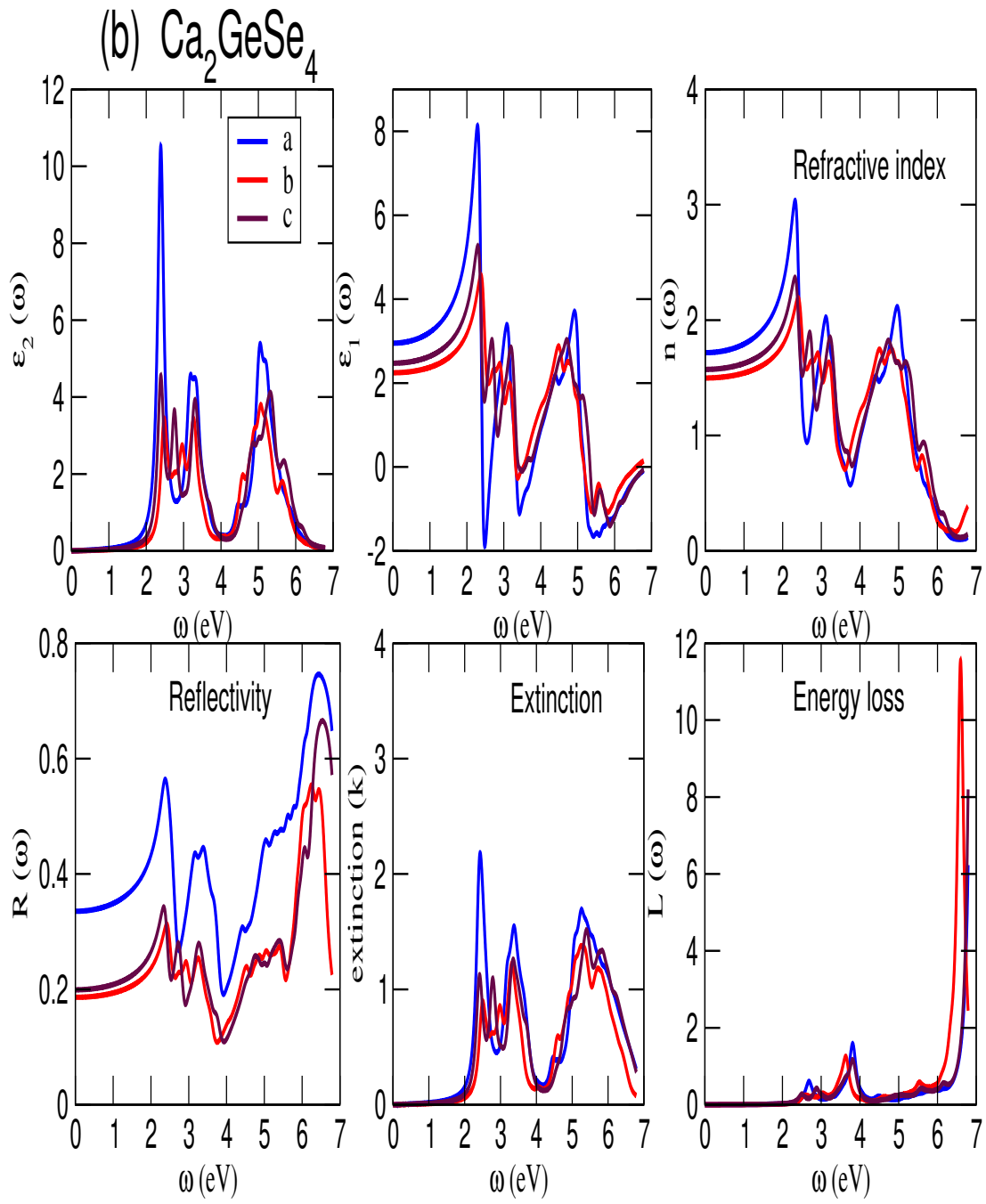

Figure 4.8: Calculated optical functions the imaginary ε_2 (ω) and real ε_1 (ω) dielectric constants, the refractive index, reflectivity, extinction and energy loss for Ca_2GeSe_4 compound.

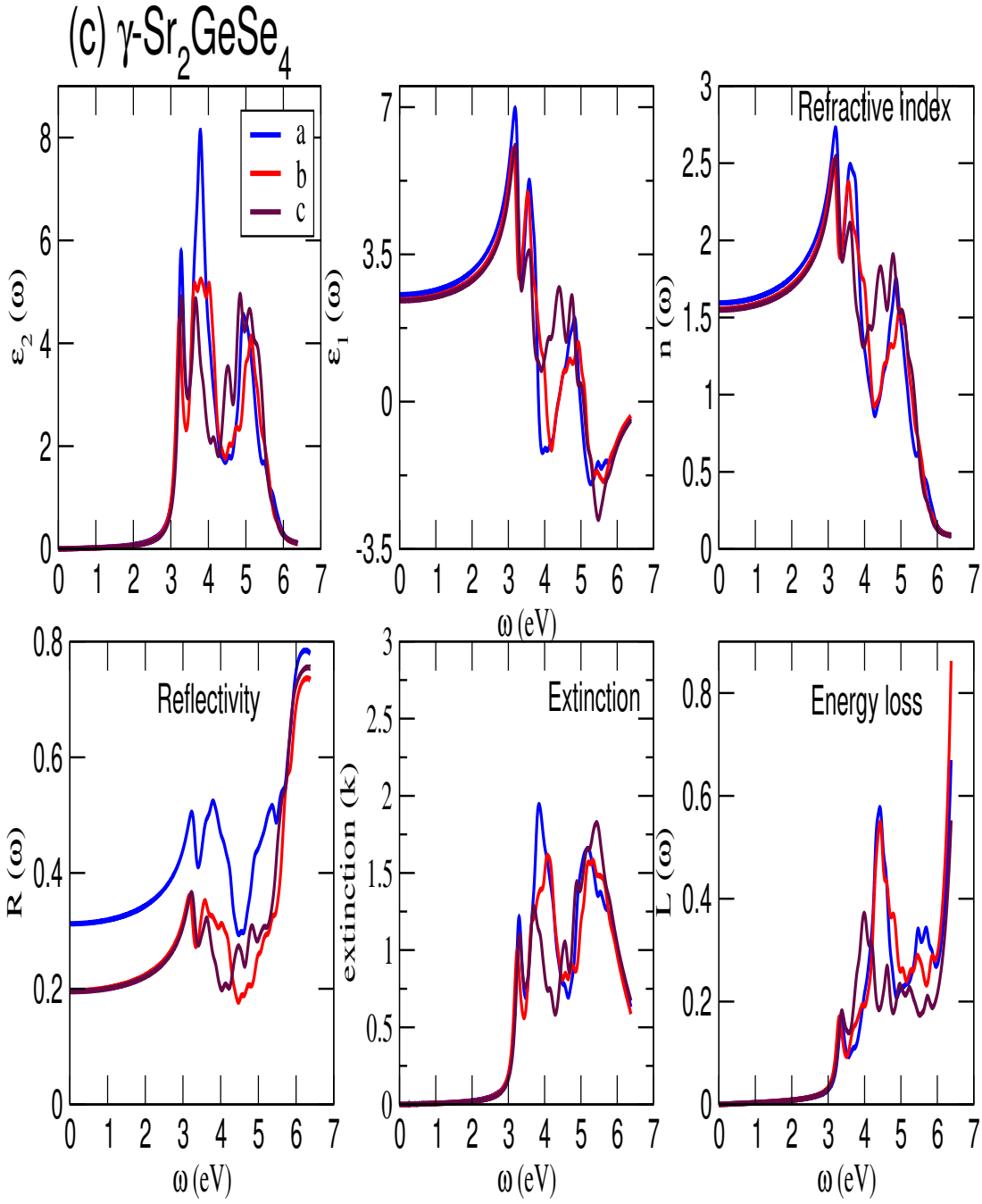

Figure 4.9: Calculated optical functions the imaginary ε_2 (ω) and real ε_1 (ω) dielectric constants, the refractive index, reflectivity, extinction and energy loss for γ-Sr_2GeSe_4 compound.

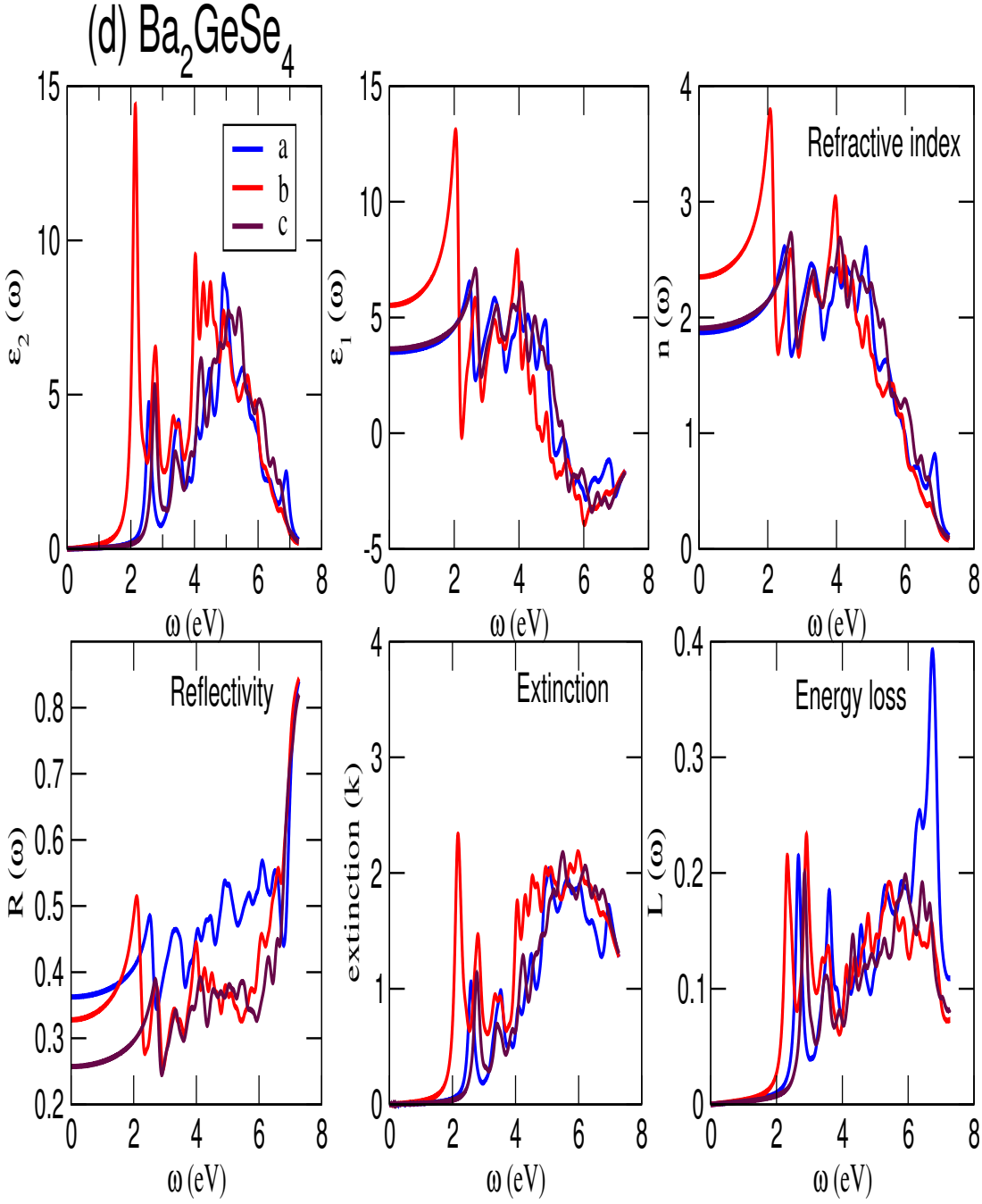

Figure 4.10: Calculated optical functions the imaginary ε_2 (ω) and real ε_1 (ω) dielectric constants, the refractive index, reflectivity, extinction and energy loss for Ba_2GeSe_4 compound.

decreases.

Refractive index $n(\omega)$ is directly connected to static real dielectric $\varepsilon_1(0)$ from the relation $n(\omega) = \sqrt{\varepsilon_1(0)}$ [158]. Wider band gap materials have a small refractive index values and vice versa as observed with our real dielectric calculation. The refractive index provides information about the optical thickness of material/path length. The calculated refractive index in the zero frequency limits $n(0)$ for A_2GeSe_4 (A = Mg, Ca, γ-Sr and Ba) are also listed in Table 4.5. From our calculation the monoclinic Ba_2GeSe_4 phase has the highest refractive index $n(0)$ of 1.88 and 2.33 along the $a-$ and $b-$ crystallograpic direction and orthorhombic Mg_2GeSe_4 with $n(0)$ of 1.92 along the $c-$ direction, owing to their characteristic of low absorption along this directions. Shown in Figure 4.7 - 4.10 refractive indices, the value of refractive index in the zero limit $n(0)$ increases with increase in photon energy (ω eV) up to the onset resonance peak which corresponds to the interband transition energy, and then proportionally decreases to zero. The reflectivity are shown on Figure 4.7 - 4.10 and the values at zero frequency $R(0)$ are depicted in Table 4.5. A_2GeSe_4 (A = Mg, Ca, γ-Sr and Ba) have $R(0)$ values ≤ 0.36. The values approach unity at zero frequency, indicating that these compounds behave like semiconductor.

Figure 4.7 - 4.10 show the relationship between the extinction coefficients and photon energy. In comparison with imaginary dielectric ε_2 (ω) the extinction (k) relates closely to each other, where the onset peaks represents the absorption behavior of the materials. The energy loss spectrum describes the amount of energy loss of fast moving electron in a material. It is associated with scattering due to collective oscillation of valence electrons. This mainly occurs at energy higher than the interband transition energy of a material, they are identified with peaks that are characterized with plasma resonance frequency (ω_p). Figure 4.7 - 4.10, shows the energy loss spectra, the corresponding energy loss are listed in Table 4.5 for A_2GeSe_4 compounds. The maximum resonance frequencies peaks seen beyond the interband transition energy are located between the energy 6.20 - 6.75 eV range for Mg_2GeSe_4, Ca_2GeSe_4, γ-Sr_2GeSe_4 and Ba_2GeSe_4 respectively.

Absorption coefficient (α (ω)) calculated from the real and imaginary dielectric constants is an important optical parameter with significant role of evaluating materials applications from their ability level of reflactance and dispertive absorption. Our calculated optical absorption spectra and their corresponding from the right Tauc plot for A_2GeSe_4 (A = Mg, Ca, γ-Sr and Ba) and their polarizabilities along the $a-$, $b-$ and $c-$

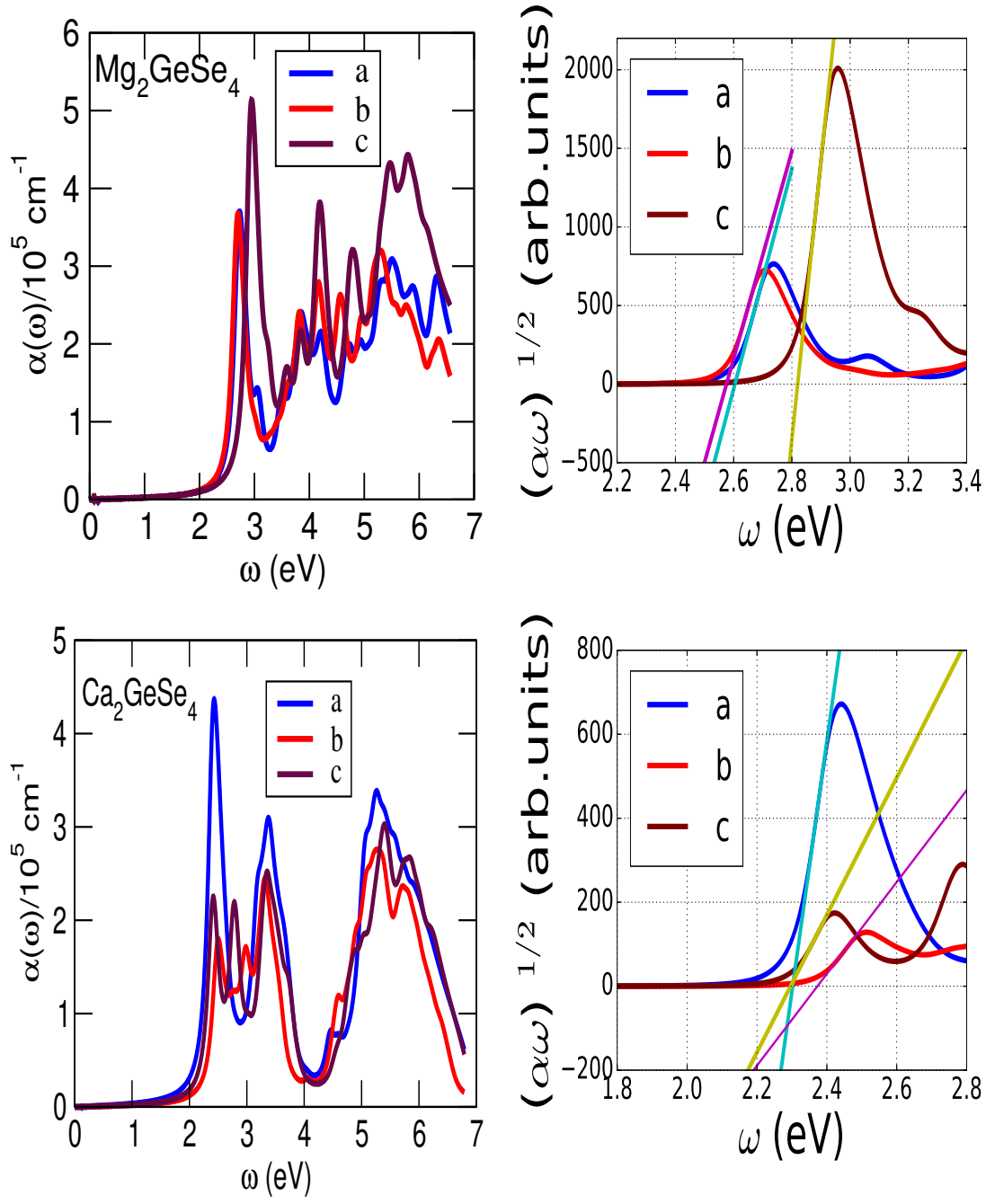

Figure 4.11: Calculated optical functions from left the absorption coefficient α (ω) and right the correspondig Tauc plot of the absorption coefficient α (ω) for A_2GeSe_4 (A = Mg and Ca) compounds respectively.

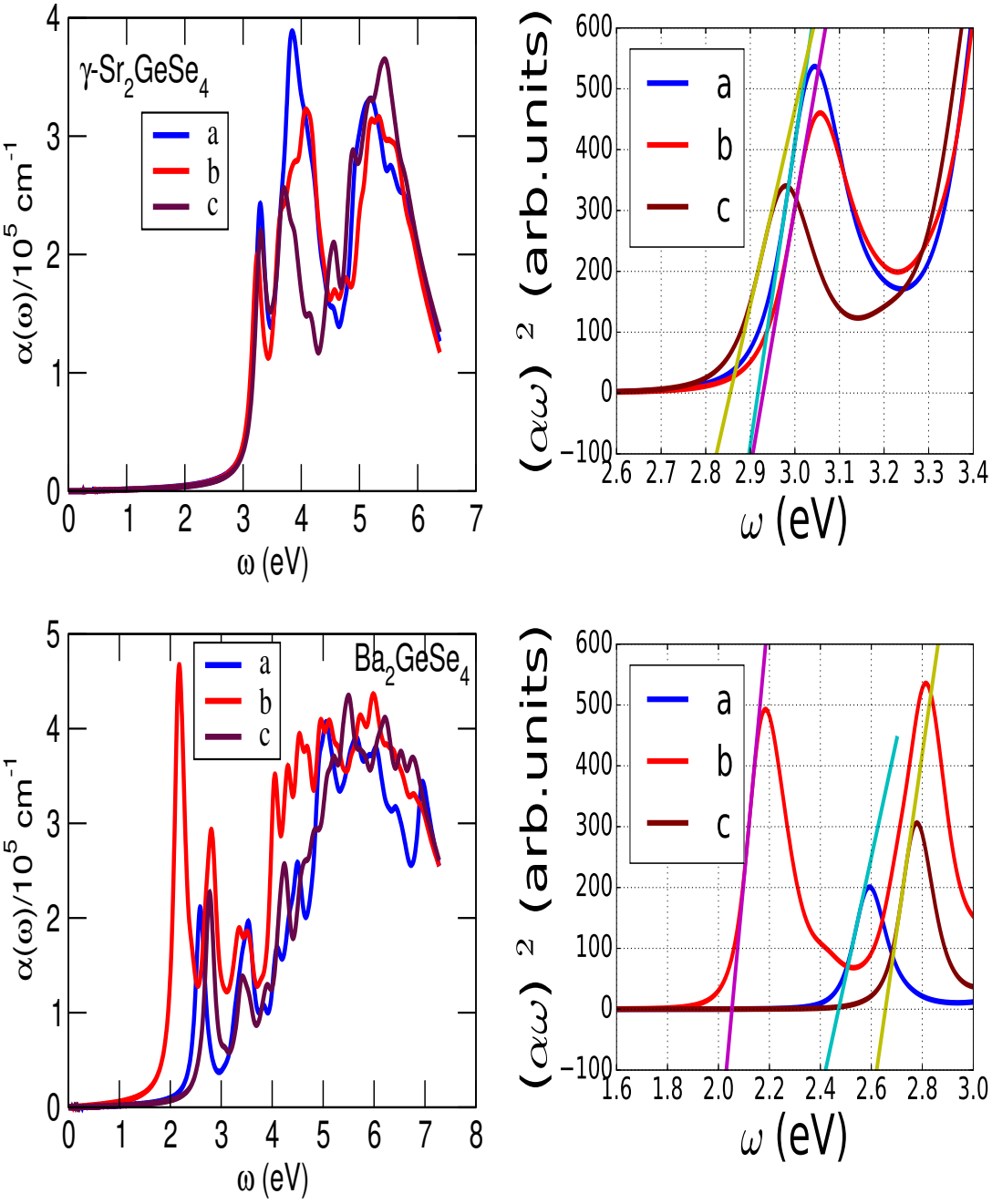

Figure 4.12: Calculated optical functions from left the absorption coefficient α (ω) and right the correspondig Tauc plot of the absorption coefficient α (ω) for A_2GeSe_4 (A = γ-Sr and Ba) compounds respectively.

Table 4.5: The calculated static real dielectric constant $\varepsilon_1(0)$, onset peak values of energy loss $L(\omega)$, static refractive index $n(0)$, static reflectivity $R(0)$ and extinction coefficient (k) along $a-$, $b-$ and $c-$ diagonal directions for A_2GeSe_4 (A = Mg, Ca, γ-Sr and Ba) compounds.

	ϵ_1 (0)			$L(\omega)$			n (0)		
Compound	$\varepsilon_1^a(0)$	$\varepsilon_1^b(0)$	$\varepsilon_1^c(0)$	$L^a(\omega)$	$L^b(\omega)$	$L^c(\omega)$	$n^a(0)$	$n^b(0)$	$n^c(0)$
Mg_2GeSe_4	2.80	2.80	3.57	0.42	0.47	0.31	1.65	1.65	1.92
Ca_2GeSe_4	2.91	2.20	2.41	0.58	0.17	0.26	1.71	1.48	1.57
γ-Sr_2GeSe_4	2.52	2.43	2.31	0.17	0.17	0.19	1.58	1.55	1.55
Ba_2GeSe_4	3.40	5.49	3.55	0.21	0.22	0.20	1.88	2.33	1.88

	$R(0)$			Extinction coefficient		
Compound	R^a (0)	R^b (0)	R^c (0)	$k^a(\omega)$	$k^b(\omega)$	$k^c(\omega)$
Mg_2GeSe_4	0.33	0.22	0.26	1.89	1.84	1.58
Ca_2GeSe_4	0.33	0.18	0.20	2.18	0.93	1.10
γ-Sr_2GeSe_4	0.31	0.19	0.19	1.21	1.08	1.08
Ba_2GeSe_4	0.36	0.33	0.26	1.03	2.30	1.13

directions are shown in Figure 4.11 and 4.12. We described the absorption edge using the Tauc plot of the optical dispersion. The Tauc method [174] determines absorption edge by linear extrapolation of $(\alpha h\nu)^{\frac{1}{n}}$ to zero from an equation $\alpha h\nu = K(h\nu - E_g)^n$. Where E_g is the gap, α is absorption, $h\nu$ the photon energy, K the proportionality constant and the exponent n takes values 2, $\frac{1}{2}$, $\frac{3}{2}$ and $\frac{1}{3}$ for direct, indirect, allowed and forbidden transitions, respectively. Our estimated onset absorption edge from Tauc plot in Figures 4.11 and 4.12 (right) for the A_2GeSe_4 (A = Mg, Ca, γ-Sr and Ba) compound are 2.58, 2.30, 2.86 and 2.05 eV respectively. Therefore, from our result of electronic structure and optical properties calculation generally these seleno-germanate A_2GeSe_4 (A = Mg, Ca, γ-Sr and Ba) compound have been observed with the following. (i) They have anisotropic behavior, direct and indirect transitions. (ii) Demonstrate broad edge of fundamental absorption between 2.05 - 2.93 eV which suggested that they are semiconductors with capability to absorb in the ultra-violet and visible region and these properties are promising for application in non-linear optics NLO, top layer absorbers in multi-junction solar cell and as a photocatalyst.

4.2 Photacatalytic properties

4.2.1 Surface structure

The suitability of semiconductor for photocatalytic application is identified through the viability of photocatalytic reaction on the surface of semiconductor not on bulk because eigenvalue of bulk calculations are not properly referenced to any absolute scale. These require the knowledge of photocatalytic band edge positions potential of semiconductor surface to predict the photocatalytic redox reactions. DFT provides means of theoretical band edge potential calculations. Theoretical semiconductor surface study is only possible with the construction of two-dimensional periodic supercell surface structure from bulk. In this work, the generalized gradient approximation GGA-PBEsol is used to study the 100, 101, 110 and 111 low indexes of A_2GeSe_4 (A = Mg, Ca, γ-Sr and Ba) surface facet orientations. The generalized gradient approximation (GGA) has been reported to yield results with accuracy in surface properties calculation [109, 175]. We use the slab approach, the (1×1)-supercell slab periodicity model bulk unit cell is used in this study. The constructed $Mg_2GeSe_4(101)$, $Ca_2GeSe_4(100)$, γ-$Sr_2GeSe_4(111)$ and $Ba_2GeSe_4(111)$ the most stable orientations with corresponding surface termination are shown in Figure 4.13.

4.2.2 Surface stability and surface energy

From the literature of A_2GeSe_4 compounds, there is no reported experimental or theoretical investigation of their surface structure and properties, in particular, no reported surface that exists in their crystallites are identified. Since there is no attempt to identified crystallite surface of A_2GeSe_4 and simulation provide this opportunity. Thus, this motivated us to carry out the surface study to predict among the constructed 100, 101, 110 and 111 low index facets the most thermodynamically favoured surface facet of A_2GeSe_4 (A = Mg, Ca, γ-Sr and Ba) compound. The thermodynamic stability of surface is determined by the surface energy (γ), which is defined by Equation 3.4.5 discussed in subsection 3.4.3. Surface energy is an excess energy associated with the surface [108]. Wulff shapes of A_2GeSe_4 were also drawn based on the calculated surface energies of the four low-index surfaces under study to confirm their appearance and stability. Wulff shape construction provides the crystal shapes under equilibrium condition that posses minimum surface energy [176, 177]. Once the stable surface orientation is

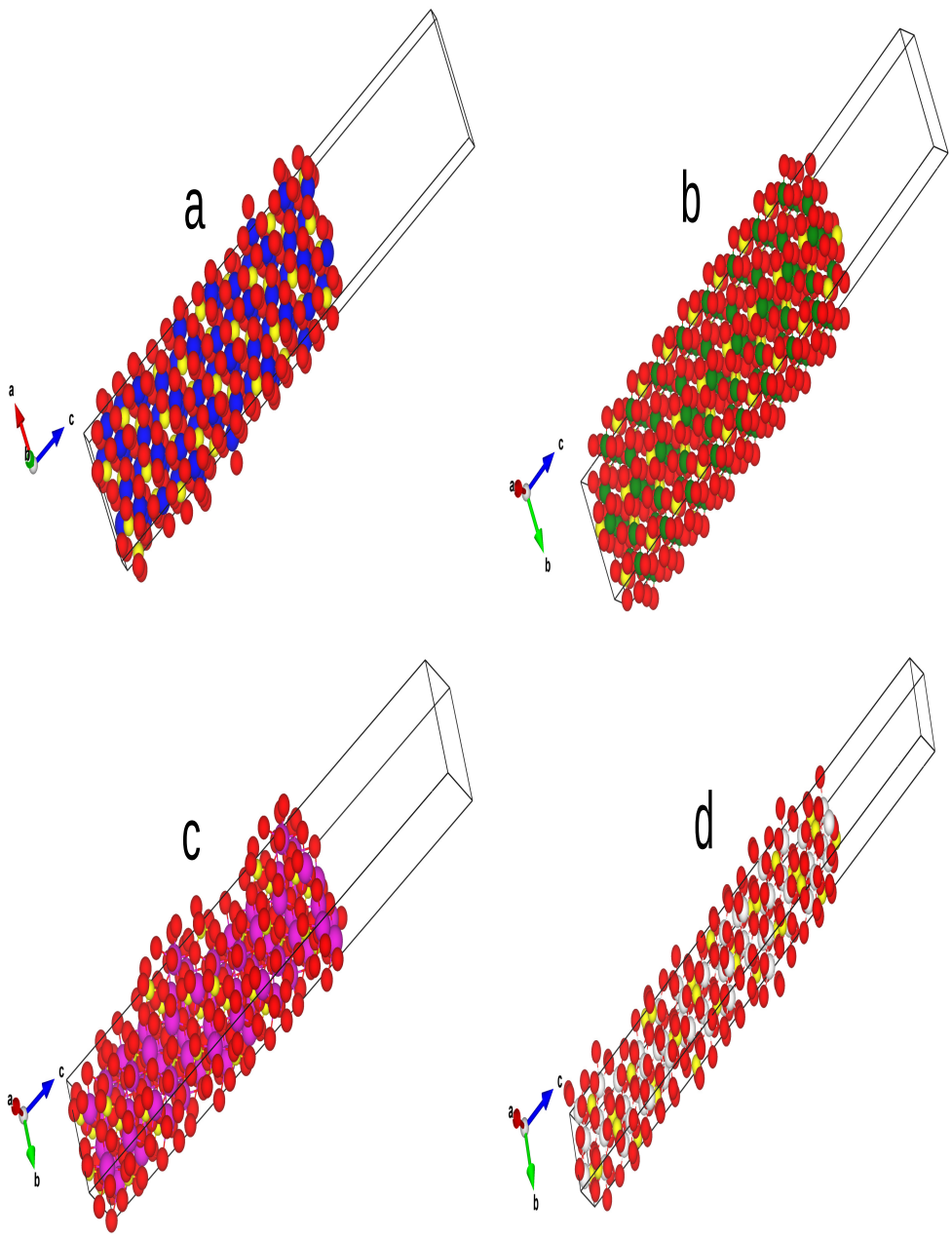

Figure 4.13: The structure of the most stable surface orientation (a) $Mg_2GeSe_4(101)$ Mg-Se termination, (b) $Ca_2GeSe_4(100)$ Ge-Se termination, (c) γ-$Sr_2GeSe_4(111)$ Sr-Se termination and (d) $Ba_2GeSe_4(111)$ Ba, Ge and Se termination, from the structure the atomic colour are Mg-blue, Ca-green, Sr-purple, Ba-white, Ge-yellow and Se-red respectively.

identified, we established other surface properties and their photocatalytic viabilities.

For the calculation of surface energy, surface relaxation or reconstruction and various convergence test are performed. Since surface energy is a function of slab thickness, surface energy fluctuates with the size of slab thickness. This effect is called the quantum size effect. We make the slab to be thick enough to get a converged surface energy. Therefore, to achieve this in order to get a reliable result, we conducted a convergence test of total slab energy as a function of slab thickness to get sufficient slab thickness. This method provides us with slab layers that are thick enough with minimum energy to model the realistic surface [178, 179], such that it's center mimics the crystal bulk. The slab thickness convergence tests are depicted in Figure 4.14. From our energy slab thickness convergence test Figure 4.14 for 100, 101, 110 and 111 facet orientations, the 9-layers slab thickness with 252 atoms are found to be thick enough to converge with lowest total slab energy for orthorhombic phase Mg_2GeSe_4, Ca_2GeSe_4 and γ-Sr_2GeSe_4 compounds with 28 atoms per unit cell in crystal bulk. Similarly, for monoclinic phase, Ba_2GeSe_4 with 14 atoms per bulk unit cell, a slab of 15-layers containing 210 atoms is found thick enough for each facet orientation to converged with lowest total slab energy.

Similarly, the approach used to determine the crystal (bulk) energy E_{bulk} in Equation 3.4.5 also has significant role in achieving surface energy convergence. Thus, for smooth surface energy convergence, E_{bulk} is extracted from the slope of linear fit of the total slab energy as a function slab thickness (N_s/N_b). This method is proposed by Fiorentini and Methfessel [180] to solve the problem of quantum size effect. Therefore, E_{bulk} are extracted from single calculation of periodic slab not from the unit cell calculation. Calculated bulk energy E_{bulk} from a linear fit of total slab energy versus slab thickness are shown in Figure 4.15. Our calculated bulk energy E_{bulk} for A_2GeSe_4 (A = Mg, Ca, γ-Sr and Ba) for each low index orientations from the linear fit of total slab energy are listed on linear fit Figure 4.15. Calculated linear fit bulk energy for 100, 101, 110 and 111 surface orientations for Mg_2GeSe_4 are -118.19, -118.18, -118.27 and -118.28 eV respectively, the energies are $\leq$ 0.19% greater compared to -118.41 eV calculated bulk unit cell energy. For Ca_2GeSe_4 the calculated energies are -131.56, -132.54, -132.52 and -132.57 eV for 100, 101, 110 and 111 orientations respectively and are greater by $\leq$ 1.22% compared to -133.16 eV bulk unit cell energy. Similarly, -132.36, -132.37, -132.46 and -132.37 eV, are calculated linear fit E_{bulk} for γ-Sr_2GeSe_4 100, 101, 110 and 111 orientations respectively and are $\leq$ 0.11% greater than -132.51 eV bulk unit cell energy, also for monolinic phase Ba_2GeSe_4 the calculated linear fit E_{bulk} are -67.99, -68.06,

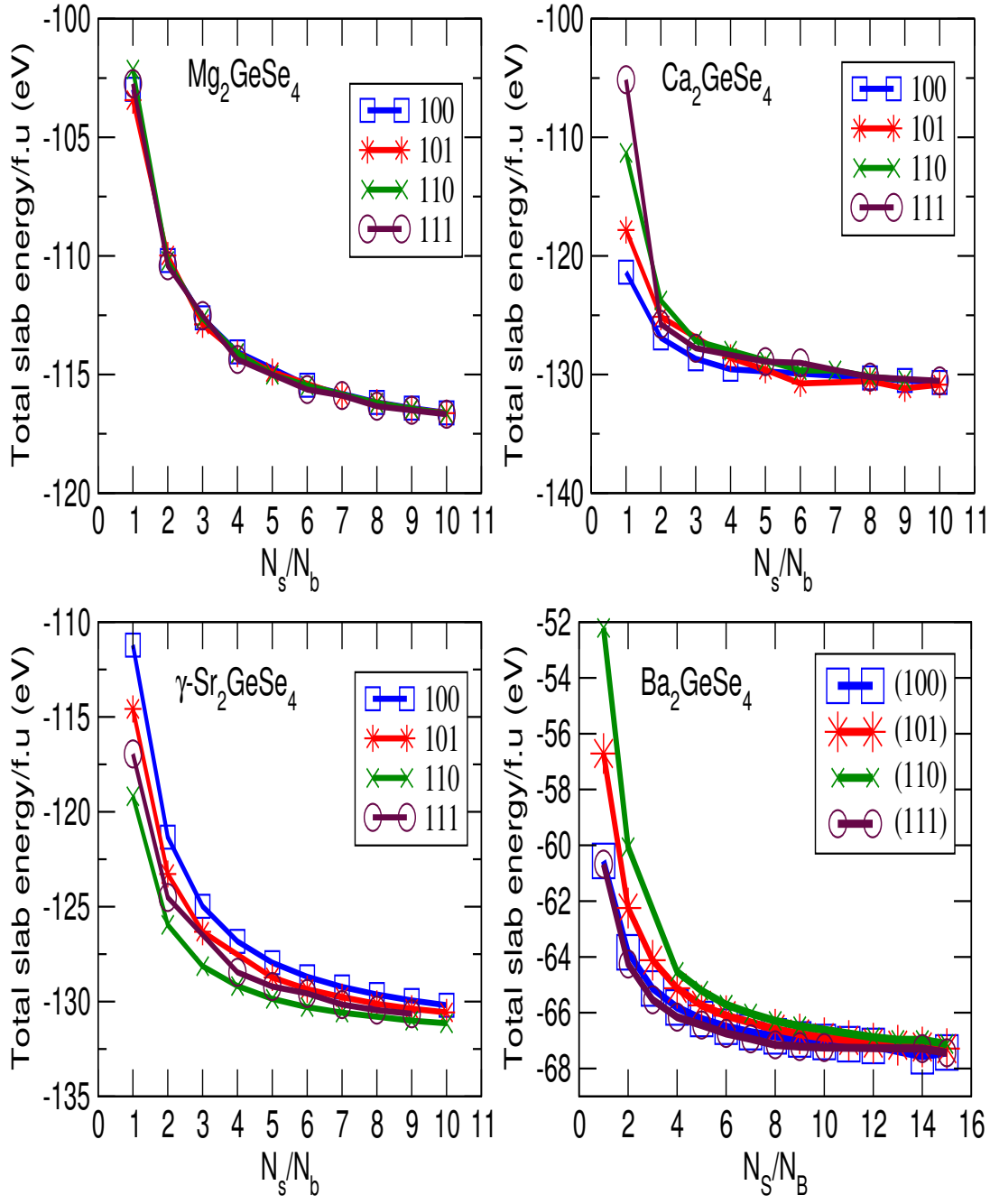

Figure 4.14: The convergence test of total slab energy as a function of slab thickness for A_2GeSe_4 (A = Mg, Ca, γ-Sr and Ba) compound.

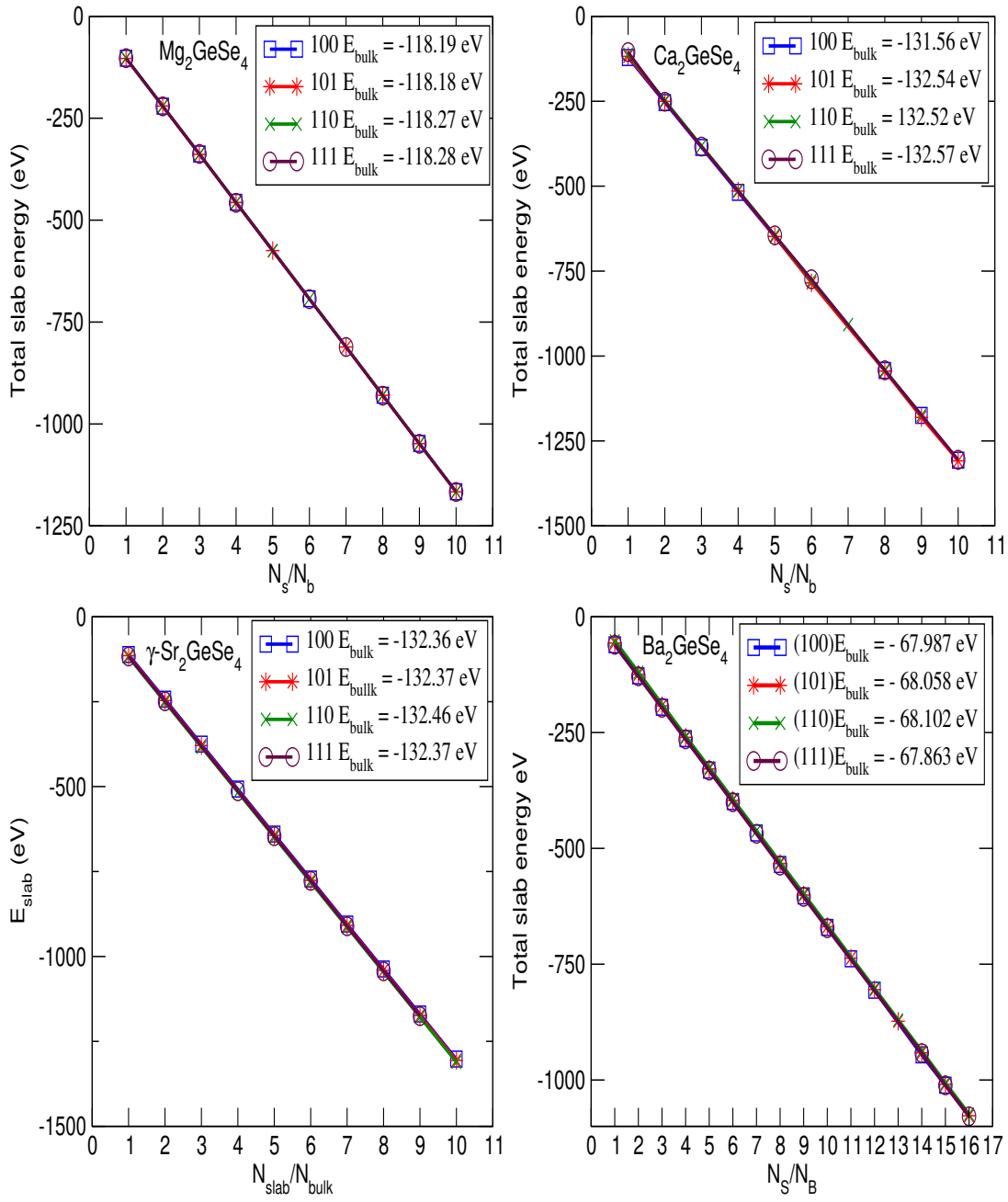

Figure 4.15: Calculated bulk energy E_{bulk} from the slope of linear fit of total slab energy versus slab thickness for A_2GeSe_4 (A = Mg, Ca, γ-Sr and Ba) compounds.

Table 4.6: (a) - (d) Calculated surface energy (J/m^2) of 100, 101, 110 and 111 surface orientation for A_2GeSe_4 (A = Mg, Ca, γ-Sr and Ba) compound respectively.

(a)Mg_2GeSe_4

Surface orientation	100	101	110	111
Surface energy (J/m^2)	1.53	1.23	1.26	1.29

(b)Ca_2GeSe_4

Surface orientation	100	101	110	111
Surface energy (J/m^2)	1.83	3.76	2.97	2.79

(c)γ-Sr_2GeSe_4

Surface orientation	100	101	110	111
Surface energy (J/m^2)	1.68	1.36	1.16	1.00

(d)Ba_2GeSe_4

Surface orientation	100	101	110	111
Surface energy (J/m^2)	1.40	1.78	2.28	0.75

-68.10 and -67.86 eV for 100, 101, 110 and 111 orientations respectively and they are $\leq$ 0.38% greater than -68.12 eV bulk unit cell energy. Although, the calculated linear fit E_{bulk} from periodic supercell slab compared to calculated bulk unit cell E_{bulk} differance is quite small, it's influence is significant for surface energy calculation and also confirm the reliability of our supercell slab calculations.

The full structural optimization for atomic positions are carried out on the converged 9-layers slab of 252 atoms for the orthorhombic A_2GeSe_4 (A = Mg, Ca and γ-Sr) and 15-layers slab of 210 atoms for monoclinic Ba_2GeSe_4 phases surfaces. From the optimized structures the vacuum convergence test are carried out to calculated vacuum size that is enough to saperate the slab layers from interacting and also for the subsequent calculation of the surface energy. Figure 4.16 shows total slab energy as a function of vacuum size. The vacuum size of 15 - 30 Å applied perpendicular to the periodic surface slab are found sufficient to separate periodic slab layers from interacting with each other for 100, 101, 110 and 111 surface orientations of A_2GeSe_4 compounds.

From each vacuum size with fixed 9 and 15 layers slab thickness for orthorhombic and monoclinic phases respectively, we calculated the surface energy using Equation 3.4.5 to also test for surface energy convergence as a function of vacuum size. Figure 4.17 shows the calculated surface energy as a function of vacuum size, as observed from this figures, the calculated surface energy are seen to converged between 20 - 30 Å vacuum size. The converged surface energy are listed in Table 4.6. Our calculated surface energy

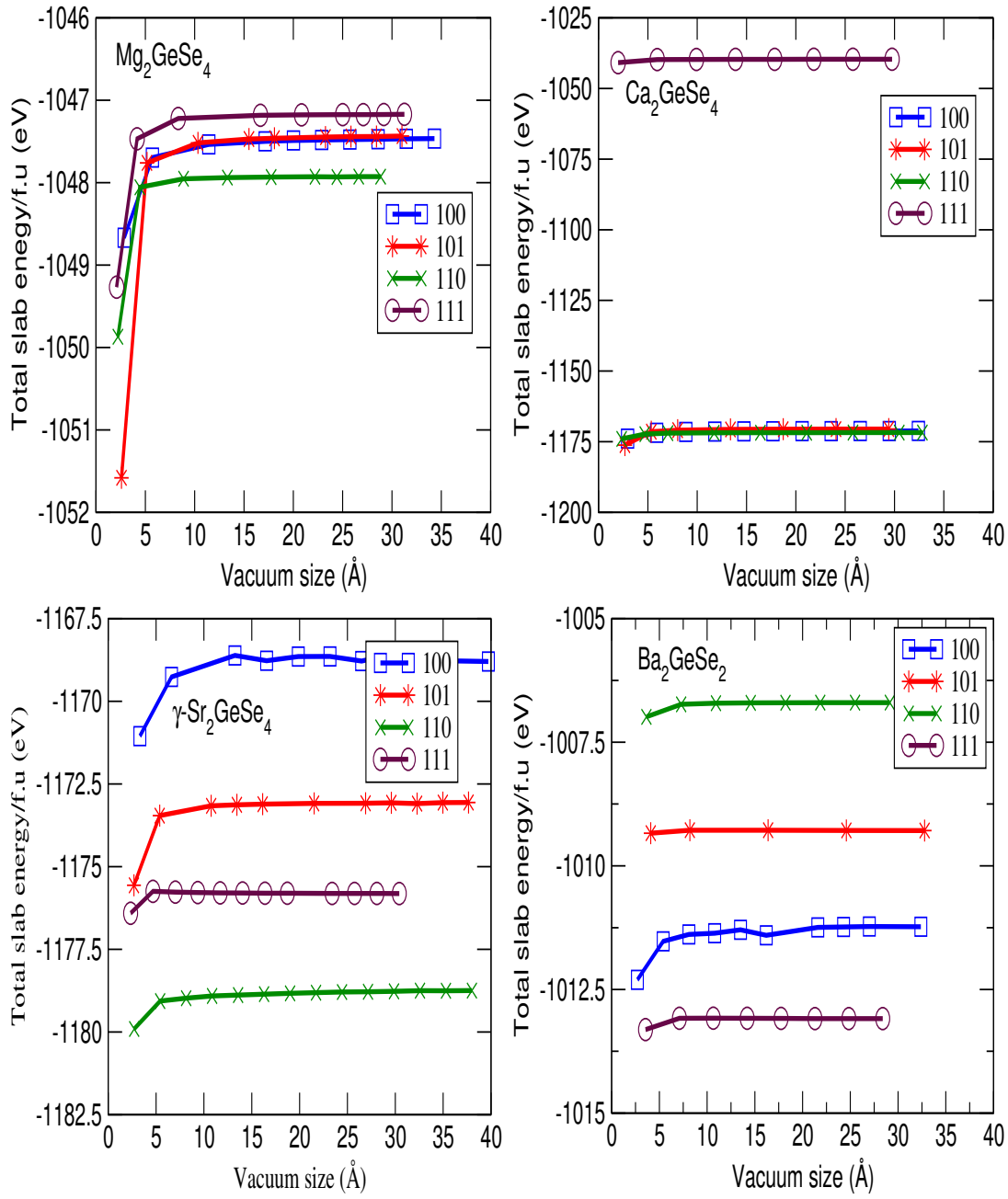

Figure 4.16: Vacuum size convergence test for variation of total slab energy on 9 slab-layer thickness for A_2GeSe_4 (A = Mg, Ca, γ-Sr) and 15 slab-layer thickness Ba_2GeSe_4 compound.

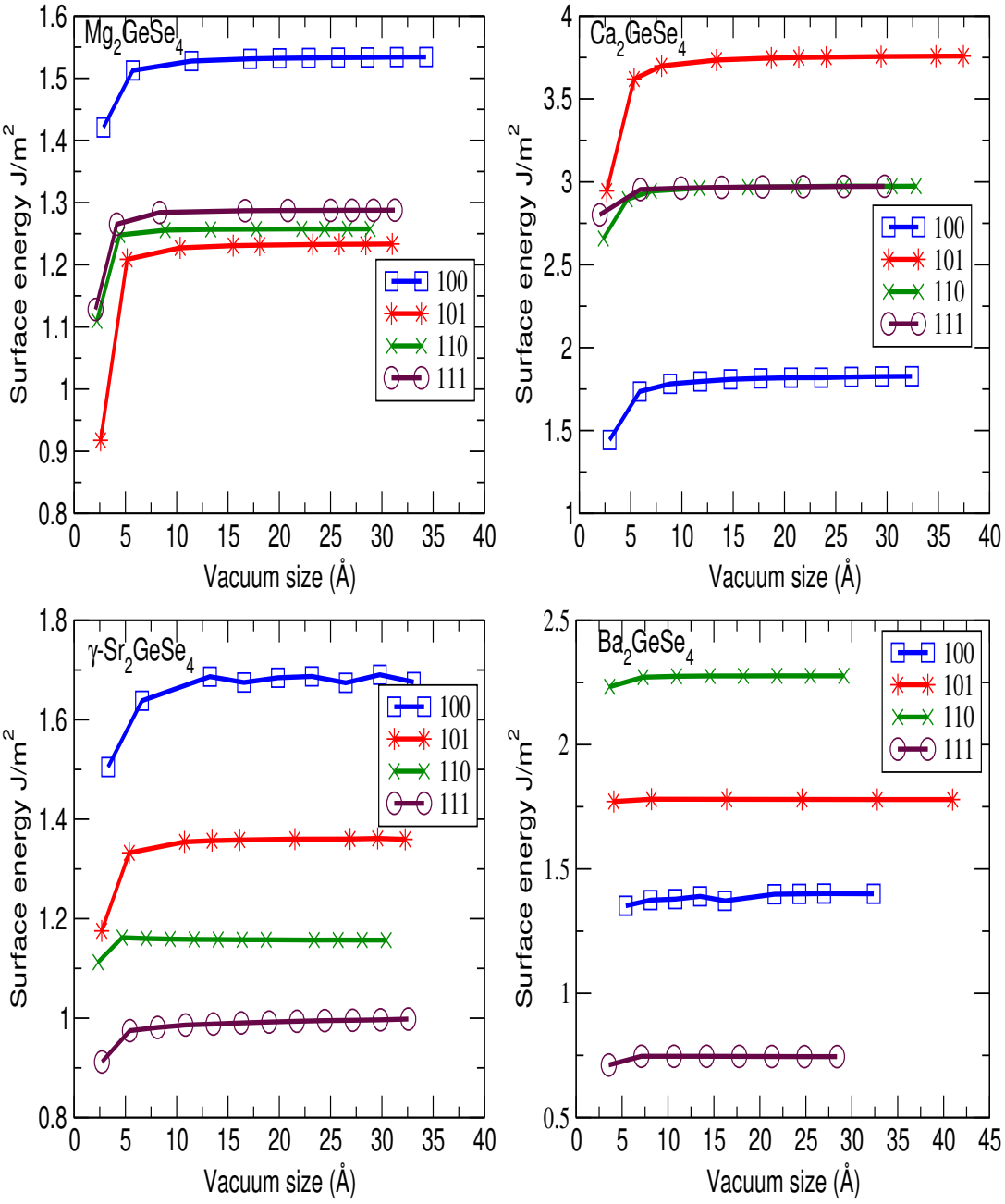

Figure 4.17: Surface energy convergence test for variation of vacuum size calculated on 9 slab-layer thickness for A_2GeSe_4 (A = Mg, Ca, γ-Sr) and 15 slab-layer thickness Ba_2GeSe_4 compound.

for Mg_2GeSe_4 100, 101, 110 and 111 orientations are 1.53, 1.23, 1.26 and 1.29 J/m^2 respectively, and for Ca_2GeSe_4 are 1.83, 3.76, 2.97 and 2.97 J/m^2 respectively. Similarly, the calculated surface energy for γ-Sr_2GeSe_4 and Ba_2GeSe_4 of 100, 101, 110 and 111 orientations are 1.68, 1.36, 1.16, 1.00 and 1.40, 1.78, 2.28, 0.75 J/m^2 respectively.

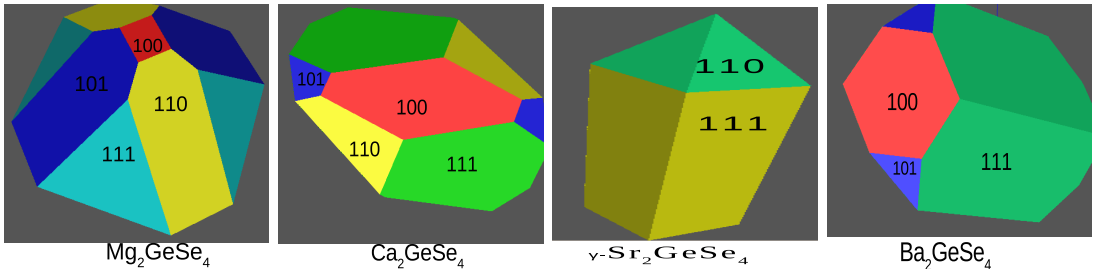

Figure 4.18: Wulff shapes constructed using the calculated surface energy of 100, 101, 110 and 111 surface orientations for A_2GeSe_4 (A = Mg, Ca, γ-Sr and Ba) compounds.

We constructed the Wulff shapes based on the calculated surface energies listed in Table 4.6, using the Edwin and Blendel [181] Wulffman crystal shape generator. The constructed Wulff shapes for A_2GeSe_4 (A = Mg, Ca, γ-Sr and Ba) compounds are shown in Figure 4.18. Wulff shapes predict the equilibrium shape of nanoparticle and identified the most stable orientation given the surface energy of the material, thermodynamically stable orientations all appear on Wulff shape [182]. From the Wulff shapes provided in Figure 4.18 the four orientations under study all appear on the Wulff shapes for Mg_2GeSe_4 and Ca_2GeSe_4, hence all the surfaces under study are thermodynamically stable with Mg_2GeSe_4(101) and Ca_2GeSe_4(100) surface orientation having larger surface area. Similarly, for γ-Sr_2GeSe_4 and Ba_2GeSe_4 only 110, 111 and 100, 101, 111 surface orientation respectively appear on the Wulff shape Figure 4.18, from the shape γ-Sr_2GeSe_4(111) and Ba_2GeSe_4(111) surface orientation are seen to occupy large surface area. Orientations with smaller surface energy are seen to have occupied the larger surface area on the Wulff shape. It is assumed that surface orientation with lower surface energy dominated the equilibrium Wulff shape. These surface orientations are the must energetically favoured and more stable surface orientations. From our calculated surface energies for A_2GeSe_4 (A = Mg, Ca, γ-Sr and Ba) surface orientations, it has been observed that Mg_2GeSe_4(101), Ca_2GeSe_4(100), γ-Sr_2GeSe_4(111) and Ba_2GeSe_4(111) orientations possess smaller calculated surface energy of 1.23, 1.83, 1.00, 0.75 J/m^2 respectively, and are seen occupied large surface are on Wulff shapes respectively, hence they are most stable and energetically favoured orientations.

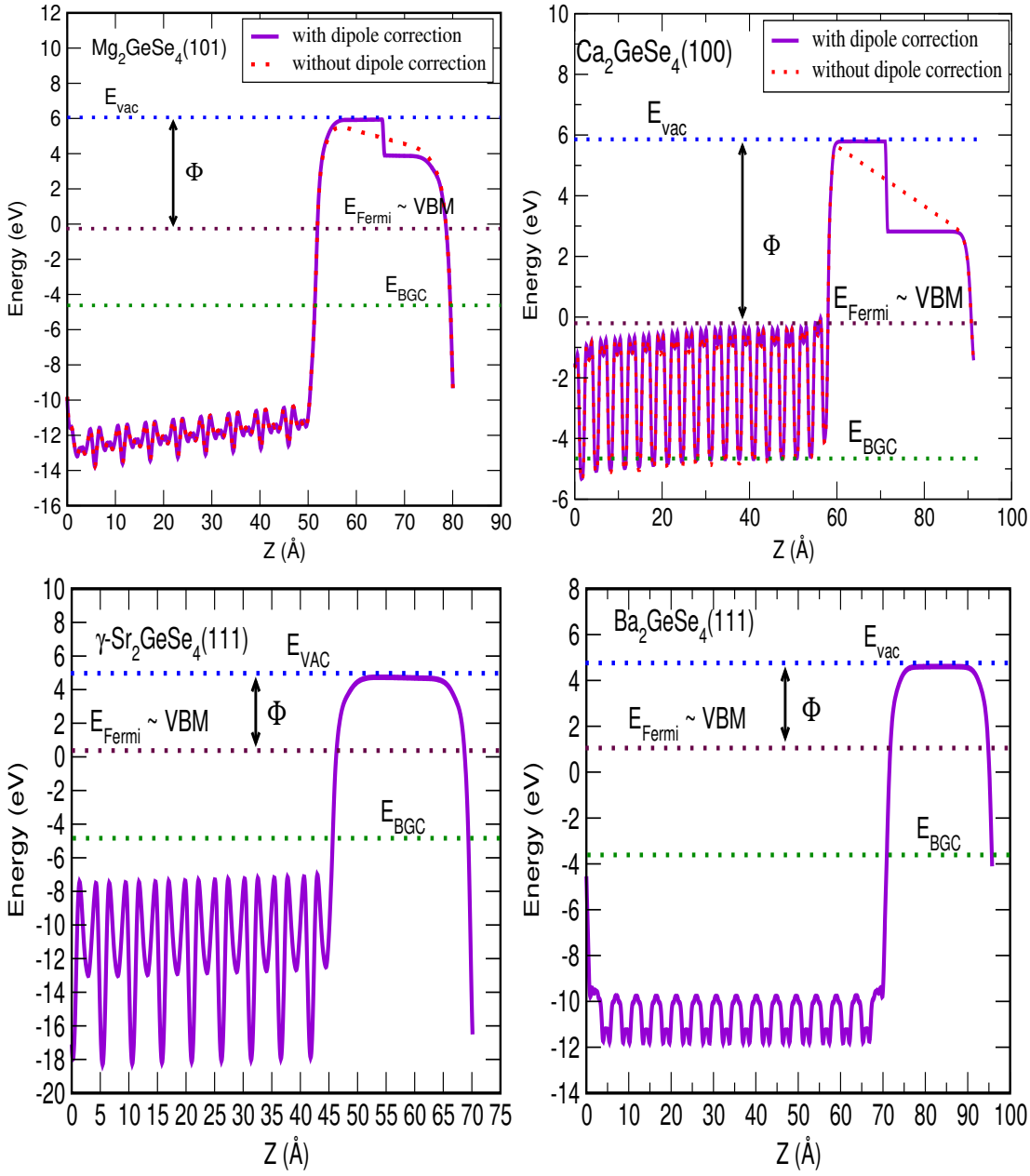

Figure 4.19: Calculated average electrostatic potential perpendicular to surface using PBEsol for $Mg_2GeSe_4(101)$, $Ca_2GeSe_4(100)$, γ-$Sr_2GeSe_4(111)$ and $Ba_2GeSe_4(111)$ surface orientation, reference Fermi energy, vacuum potential and band gap center are represented by Maroon, blue and green colours dotted line respectively. Red dotted curve on $Mg_2GeSe_4(101)$ and $Ca_2GeSe_4(100)$, show calculated average electrostatic potential without dipole correction.

4.2.3 Electrostatic potential, work function and band gap center

The calculation of average electrostatic potential perpendicular to periodic surface is very important and critical in determining the flat vacuum potential level and work function. All calculation of the average electrostatic potential perpendicular to periodic surface are performed on $Mg_2GeSe_4(101)$, $Ca_2GeSe_4(100)$, γ-$Sr_2GeSe_4(111)$ and $Ba_2GeSe_4(111)$, the most stable and energetically favourable surface orientation according to our calculation of surface energy and Wulff shape diagram. On the most stable surface the 9 and 15 layers periodic slab thick and vacuum size of 20 - 30 Å is used for the calculation of the average electrostatic potential. However, the periodic slab surface of $Mg_2GeSe_4(101)$, $Ca_2GeSe_4(100)$, γ-$Sr_2GeSe_4(111)$ and $Ba_2GeSe_4(111)$ are Tasker type 3 surface [108]. They are charged and have dipole moment created perpendicular to the surface. Similarly, the choice of plane-wave basis set used in this calculation imposess periodic boundary conditions on the electrostatic potential which creates artificial electrostatic potential in the vacuum region [109]. Therefore, to determine the flat vacuum potential we included the dipole correction to cancel the perpendicular dipole moment in the vacuum region [108, 109] in the average electrostatic calculation. For $Mg_2GeSe_4(101)$ and $Ca_2GeSe_4(100)$ are surfaces that have large internal dipole moment, therefore the electrostatic potential on either of the periodic surface layer differ. Thus calculated average electrostatic potential with dipole correction to cancel the large dipole moment in the vacuum region created a potential jump seen in Figure 4.19 [109, 110, 183]. Figure 4.19 shows the calculated average electrostatic potential (violet curve) for $Mg_2GeSe_4(101)$, $Ca_2GeSe_4(100)$, γ-$Sr_2GeSe_4(111)$, and $Ba_2GeSe_4(111)$ surface orientation with flat vacuum potential energy indicated by the top-blue dotted line.

Using the flat vacuum potential energy (E_{vac}), we evaluated the work function (Φ) using Equation 2.4.1 in combination of valence band minimum (VBM) approximated to Fermi energy ($E_{\mathrm{F}ermi} \approx \mathrm{V}BM$). The energy of band gap center (BGC) is also calculated using the method described in chapter 3 section 3.1. The vacuum potential energy, work function and band gap center are listed in Table 4.7 (a). It can be seen from Table 4.6 (a) the calculated work function for the orthorhombic phase $Mg_2GeSe_4(101)$, $Ca_2GeSe_4(100)$, γ-$Sr_2GeSe_4(111)$ of the most stable orientation are similar with only about 3% difference. This can be associated with their cohesive energy (E_{coh}) listed in Table 4.2 and their Fermi energy levels. The monoclinic phase $Ba_2GeSe_4(111)$ has the

Table 4.7: (a) and (b) Calculated from slab model the vacuum potential E_{vac}, work function Φ, band gap center BGC, band egdes E_{VBM} and E_{CBM} in eV respectively and surface energy γ in J/m^2 from the most stable surface and calculated E_{VBM} and E_{CBM} eV using the absolute Mulliken's electronegativity EN model for A_2GeSe_4 (A = Mg, Ca, γ-Sr and Ba) compound respectively.

(a)

Surface	E_{vac}	Φ	E_{BGC}	G_0W_0+BSE		HSE06		γ
				E_{VBM}	E_{CBM}	E_{VBM}	E_{CBM}	
Mg_2GeSe_4(101)	5.021	4.829	-4.727	-6.017	-3.437	-6.092	-3.362	1.23
Mg_2GeSe_4(110)	5.136	5.204	-5.190	-6.480	-3.90	-6.555	-3.825	1.26
Ca_2GeSe_4(100)	4.447	4.662	-4.644	-5.794	-3.494	-5.824	-3.464	1.83
γ-Sr_2GeSe_4(111)	4.867	4.688	-4.579	-6.009	-3.149	-5.984	-3.174	1.00
Ba_2GeSe_4(111)	4.761	3.841	-3.711	-4.736	-2.689	-5.041	-2.381	0.75

(b)

compound	bulk	
	E_{VBM}	E_{CBM}
Mg_2GeSe_4	1.972	-0.978
Ca_2GeSe_4	1.052	-1.474
γ-Sr_2GeSe_4	1.221	-1.869
Ba_2GeSe_4	1.164	-1.366

lowest recorded work function of 3.841 eV due to higher position of Fermi energy level.

4.2.4 Absolute band edge potentials

The absolute band edges are considered as highly surface dependent, it is important to consider more stable surface[184]. To our knowledge, there is no reported experimentally identified surface for Seleno-germanates A_2GeSe_4 (A = Mg, Ca, γ-Sr and Ba) compound. Therefore, the most stable surface orientation with smaller surface energy identified from our calculation is used for the evaluation of band edges. For the slab model, the band edge positions E_{VBM} and E_{CBM} are calculated using equation 3.1.1 and 3.1.2. The calculated G_0W_0+BSE and HSE06 energy gap E_g are used for the calculation E_{VBM} and E_{CBM}, because the G_0W_0+BSE calculation corrected the ionization potential [185]. The HSE06 band gap is additionally used for calculating E_{VBM} and E_{CBM} positions because HSE06 estimated band gap compared to G_0W_0+BSE are $\leq 5\%$ less. The E_{VBM} and E_{CBM} positions are also calculated using the empirical model of Mulliken's absolute electronegativity (EN) of atoms. The model is based on the assumption of absolute electronegativity (χ) as a geometrical mean of electronegativities of the constituent atoms [117, 186] using equation 3.1.3 and 3.1.4. In Table 4.7 (a) and (b) we show the calculated band edges E_{VBM} and E_{CBM} for A_2GeSe_4 (A = Mg, Ca, γ-Sr and Ba)

materials obtained from the slab model using the G_0W_0+BSE and HSE06 band gaps and EN model using G_0W_0+BSE respectively.

To evaluate the implication of our calculated band edges for these materials to water-splitting they are compared to the standard redox potential for water-splitting. Figure 4.20 shows the slab model band edges positions of A_2GeSe_4 (A = Mg, Ca, γ-Sr and Ba) calculated using G_0W_0-BGC approach compared to the standard hydrogen electrode (SHE) with respect to the redox potential for reduction -4.44/-4.03 eV (H^+/H_2) and oxidation -5.67/-5.26 eV (H_2O/O_2) of water in a vacuum scale at pH = 0 and 7 respectively [187], since the photacatalytic reaction are closely pH dependent [119] and redox potentials are calculated using E_{H^+/H_2} = -4.44 eV + pH×0.059 eV and E_{O_2/H_2O} = -5.67 eV + pH×0.059 eV for reduction and oxidation potentials respectively. For a semiconductor material to function as a photocatalyst, its band edge E_{VBM} and E_{CBM} positions has to be more negative and positive respectively than the redox potential SHE electrode.

The calculated band egde E_{VBM} and E_{CBM} are listed in Table 4.7, the values are compared to standard hydrogen electrode (SHE) at pH = 0 and pH = 7 as shown in Figure 4.20 respectively. The Mg_2GeSe_4(101), Mg_2GeSe_4(110), Ca_2GeSe_4(100) and γ-Sr_2GeSe_4(111) surfaces have E_{VBM}/E_{CBM} positions values of -6.017/-3.437, -6.480/-3.90, -5.794/-3.394 and -6.009/-3.149 eV respectively. It is seen that the E_{VBM} is more negative than the oxidation potential and E_{CBM} is more positive than the reduction potential compared to SHE redox potential measured on both pH = 0 and pH = 7 scale, respectively. The estimated reduction power which is the energy difference between the hydrogen reduction potential and the E_{CBM} energy are 1.00/0.58, 0.54/0.12, 0.95/0.53 and 1.29/0.87 for pH = 0/7 for Mg_2GeSe_4(101), Mg_2GeSe_4(110), Ca_2GeSe_4(100) and γ-Sr_2GeSe_4(101) respectively. While the difference between the oxidation potential and the E_{VBM} energy the so-called oxidation power for Mg_2GeSe_4(101), Mg_2GeSe_4(110), Ca_2GeSe_4(100) and γ-Sr_2GeSe_4(101) are 0.34/0.76, 0.81/1.22, 0.12/0.53 and 0.34/0.75 for pH = 0 and 7 respectively. Therefore, our result obtained based on vacuum calculations suggest that the orthorhombic Mg_2GeSe_4(101), Ca_2GeSe_4(100) and γ-Sr_2GeSe_4(111) surfaces are promising photocatalytic materials for unassisted water-splitting application. For the monoclinic Ba_2GeSe_4(111) surface, our slab model calculation shows that this compound have -4.976 and -2.446 eV E_{VBM} and E_{CBM} respectively. Compared with the redox potential Ba_2GeSe_4 have more positive E_{CBM} position than the reduction potential and can only be used for water reduction (H^+/H_2). To our very best

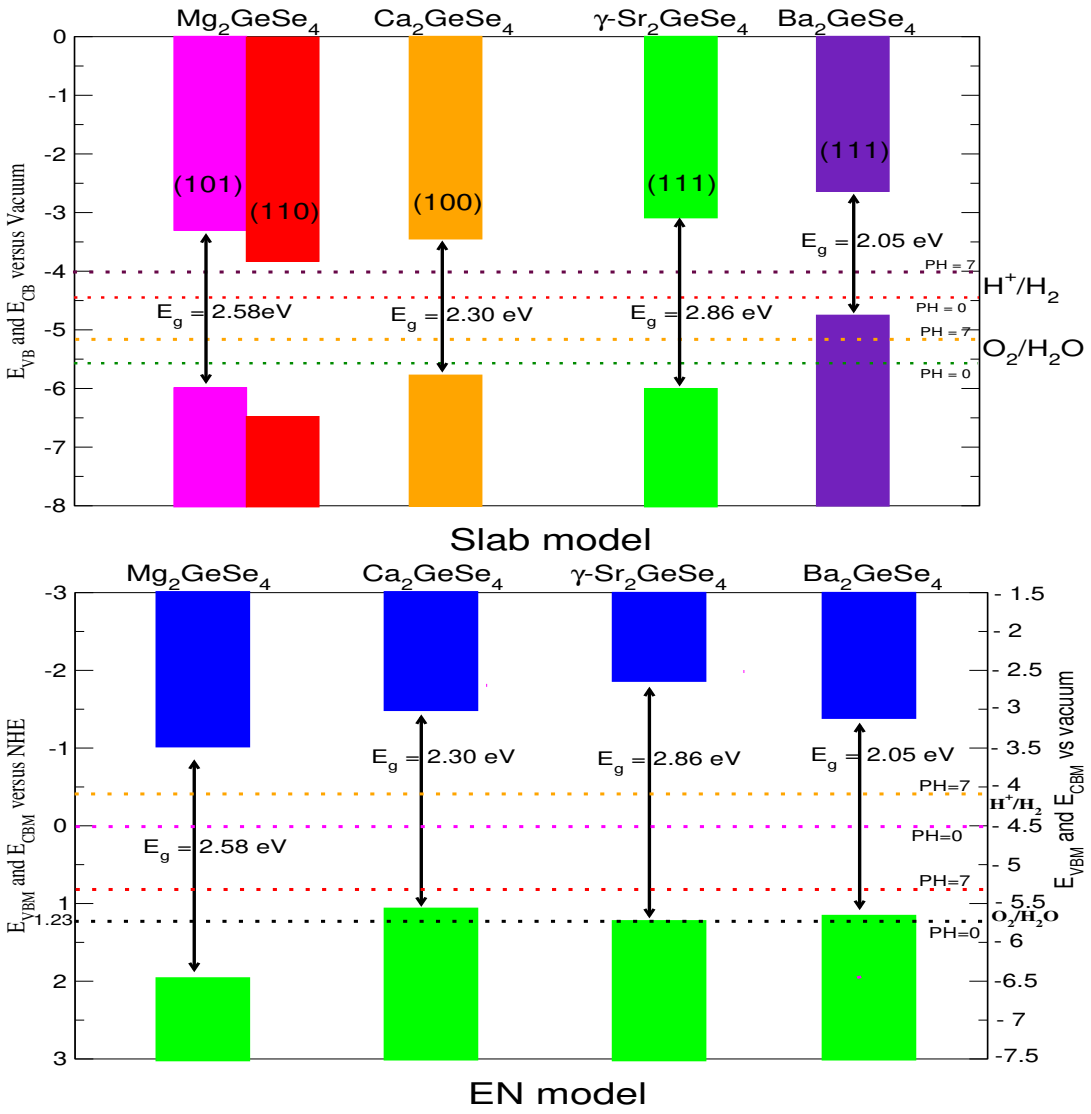

Figure 4.20: Calculated valence band maximum E_{VBM} and conduction band minimum E_{CBM} edge positions using G_0W_0 + BSE band gap versus redox potential of reduction H^+/H_2 and oxidation O_2/H_2O in the vacuum and normal hydrogen electrode (NHE) of water-splitting for A_2GeSe_4 (A = Mg, Ca, γ-Sr and Ba) compound obtained from the slab model and EN model respectively.

knowledge, there is no available experimental and theoretical data for E_{VBM} and E_{CBM} band edge for comparison. Our calculated band edge positions using G_0W_0+BSE and HSE06 compared to redox potential from slab model confirmed that A_2GeSe_4 (A = Mg, Ca, γ-Sr) compound have E_{VBM} and E_{CBM} position suitable for overall water-splitting for O_2 and H_2 evolution and Ba_2GeSe_4 has only suitable E_{CBM} for water reduction.

Table 4.7 (b) shows the calculated band edge E_{VBM} and E_{CBM} position using the absolute Mulliken's electronegativity (EN) model by employing the G_0W_0+BSE band gap. The calculated conduction and valence band edge E_{CBM}/E_{VBM} are -0.978/1.972, -1.474/1.056, -1.869/1.221 and -1.366/1.164 eV versus (NHE) for A_2GeSe_4 (A = Mg, Ca, γ-Sr and Ba) respectively. The E_{VBM} and E_{CBM} are compared to the (NHE) redox potential the absolute vacuum scale ($E_{AVS} = 0$) of reduction potential H^+/H_2O (0.0 eV) and oxidation potential O_2/H_2O (1.23 eV) and vacuum potential for pH = 0 and 7 respectively. Figure 4.20 shows the E_{CBM}/E_{VBM} position calculated using EN model are compared to the redox potential of NHE and vacuum for pH = 0 and 7, at pH = 0 it is seen that Mg_2GeSe_4 compound can straddle the redox potential of water, while A_2GeSe_4 (A = Ca, γ-Sr and Ba) possess only reduction potential of water. Similarly, E_{CBM}/E_{VBM} position compared to the redox potential of NHE and vacuum at pH = 7 shows that A_2GeSe_4 (A = Mg, Ca, γ-Sr and Ba) both can straddle potential of water. Therefore, according to EN model A_2GeSe_4 (A = Mg, Ca, γ-Sr and Ba) compounds have redox potential positions for overall water splitting into O_2 and H_2 evolutions at pH = 7. Due to limited experimental and other theoretical data for this compounds, from the basis of our analysis of both the slab model and EN model calculated valence band maximum and conduction band minimum compared with redox potential of normal hydrogen and vacuum electrode for pH = 7 can serve as guide for photocatalytic promising application of A_2GeSe_4 (A = Mg, Ca, γ-Sr and Ba) compounds.

4.2.5 Bader charge analysis

The Bader charge density analysis at the surface of A_2GeSe_4 was carried out to investigate the charge depletion and accumulation at the topmost surface layer of A_2GeSe_4 (A = Mg, Ca, γ-Sr and Ba) compound. Charge density analysis was carried out using VESTA [188], with the help of equation of charge density difference of system and it's fragment given as $\Delta\rho = \rho_{ABC} - \sum \rho_i^{fragment}$, where ρ_{ABC} is total charge density of

A_2GeSe_4 and $\rho_i^{fragment}$ is the charge density of individual isolated A, Ge and Se atoms of the system. Charge density distribution on A_2GeSe_4(A = Mg, Ca, γ-Sr, Ba) surfaces are identical, Figure 4.21 shows the charge density distribution on isosurface of A_2GeSe_4(A = Mg, Ca, γ-Sr, Ba) surface. The A, Ge, and Se atoms are represented by purple, green and red colour respectively. From the top isosurface layer the yellow colour is the charge distribution/accumulation, the cyan colour is the charge depletion due to the top layer surface termination atoms. Charge depletion are seen around the A and Ge atoms, indicating that the A and Ge atoms contribute charges to share with other atoms. Similary, the charge accumulation are observed around the Se atom which indicate that Se atom is covalently bonded with other atom on the surface. The charge accumulation in yellow coloured seen at the top isosurface in Bader charge analysis of the system is reported to be responsible in enhancing the PEC and photocatalytic activities of materials, by likely decreasing the charge recombination and easy charge transfer to adsorbates [189, 190]. From the charge analysis for these A_2GeSe_4 compounds, which demonstrates charge density depletion at isosurfaces; and analysis of their band edge positions, one can conclude that these compounds may be suitable for phocatalytic applications.

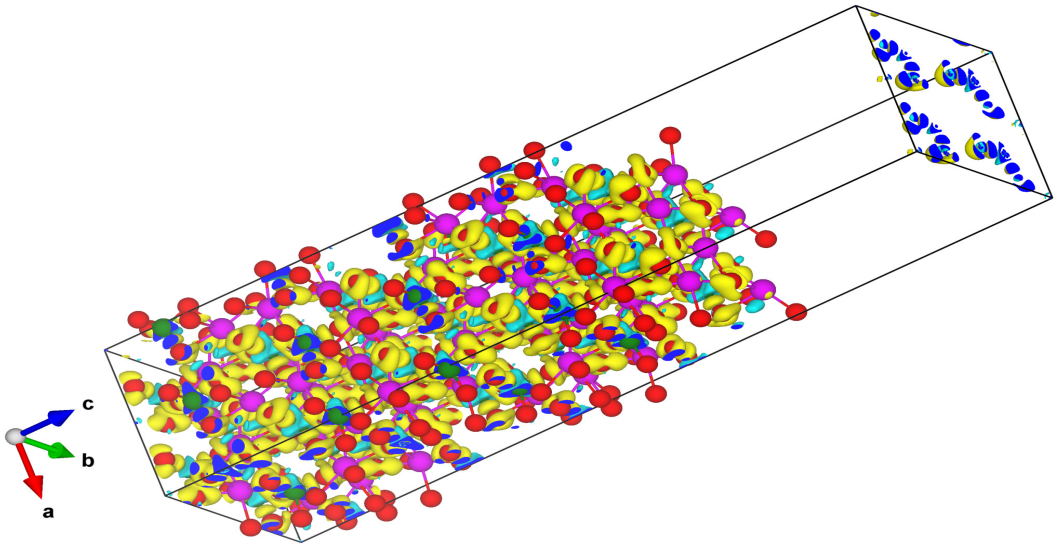

Figure 4.21: The calculated charge density distribution plot of A_2GeSe_4 surface. The purple, green and red colours represent A, Ge, and Se atoms respectively. At the top isosurface, the cyan and yellow colours denote depletion and accumulation of charge density.

4.2.6 Surface electronic structure

We calculated electronic density of states (EDOS) of bulk A_2GeSe_4 (A = Mg, Ca, γ-Sr and Ba), their more stable surface $Mg_2GeSe_4(101)$, $Ca_2GeSe_4(100)$, γ-$Sr_2GeSe_4(101)$ and $Ba_2GeSe_4(101)$ are considered. Figure 4.22 and 4.23 shows (from the left) bulk EDOS and (from the right) surface electronic density of state for comparison. The characteristic features of the calculated EDOS for both bulk and surface are quite similar, the surface EDOS are more dense and pronounced with additional peaks compared to bulk. For Mg_2GeSe_4 and its (101) surface, Ca_2GeSe_4 and its (100) surface their top valence bands are dominated by contribution from p-orbital of Se atom and contribution of p-orbital of Se and s-orbital of Ge atoms are seen to dominate their conduction bands. Similarly, for γ-Sr_2GeSe_4 and its (111) surface, Ba_2GeSe_4 and its (111) surface their valence band are dominated by contribution of p-orbital of Se atom, while their bottom conduction bands are seen to be dominated by p-orbital of Se, s-orbital of Ge, d-orbital of Sr and Ba atoms respectively. Significant difference seen between the calculated bulk and surface EDOS is the formation of TDOS and PDOS of p-orbital of Se atom surface state located around the zero Fermi-level. This is due to creation of surface state; which indicate that this surfaces state could act as trapping center to achieve a good electric performance and reactivity [190].

Also observed from Figure 4.22 and 4.23 is the difference between band gap described by the calculated EDOS of bulk and that of surface states, there is significant band gap reduction in surface state. According to our calculation $Mg_2GeSe_4(101)$ surface is described as metal with no band gap between VBM and CBM, while $Ca_2GeSe_4(100)$ surface has a very narrow band gap. Similarly, for γ-$Sr_2GeSe_4(111)$ and $Ba_2GeSe_4(111)$ surfaces are semiconductors with small difference between their band gaps and that of the bulk compounds. These band gap reduction in surface electronic structures are due to conduction band minimum shifting toward valence band and may be attributed to surface termination and effect of charge disproportionations at topmost surface layer [191]. The band gap reduction and existance of surface electronic state around the Fermi energy are some of the features of electronic properties of surface state and is a common characteristic observed with an extended two-dimensional (2D) systems [153, 191, 192, 193] Finally, from our investigation of photocatalytic properties of selenogermanate A_2GeSe_4 (A = Mg, Ca, γ-Sr and Ba) compound. We have seen from the analysis of band edge positions compared with redox potential of standard hydrogen

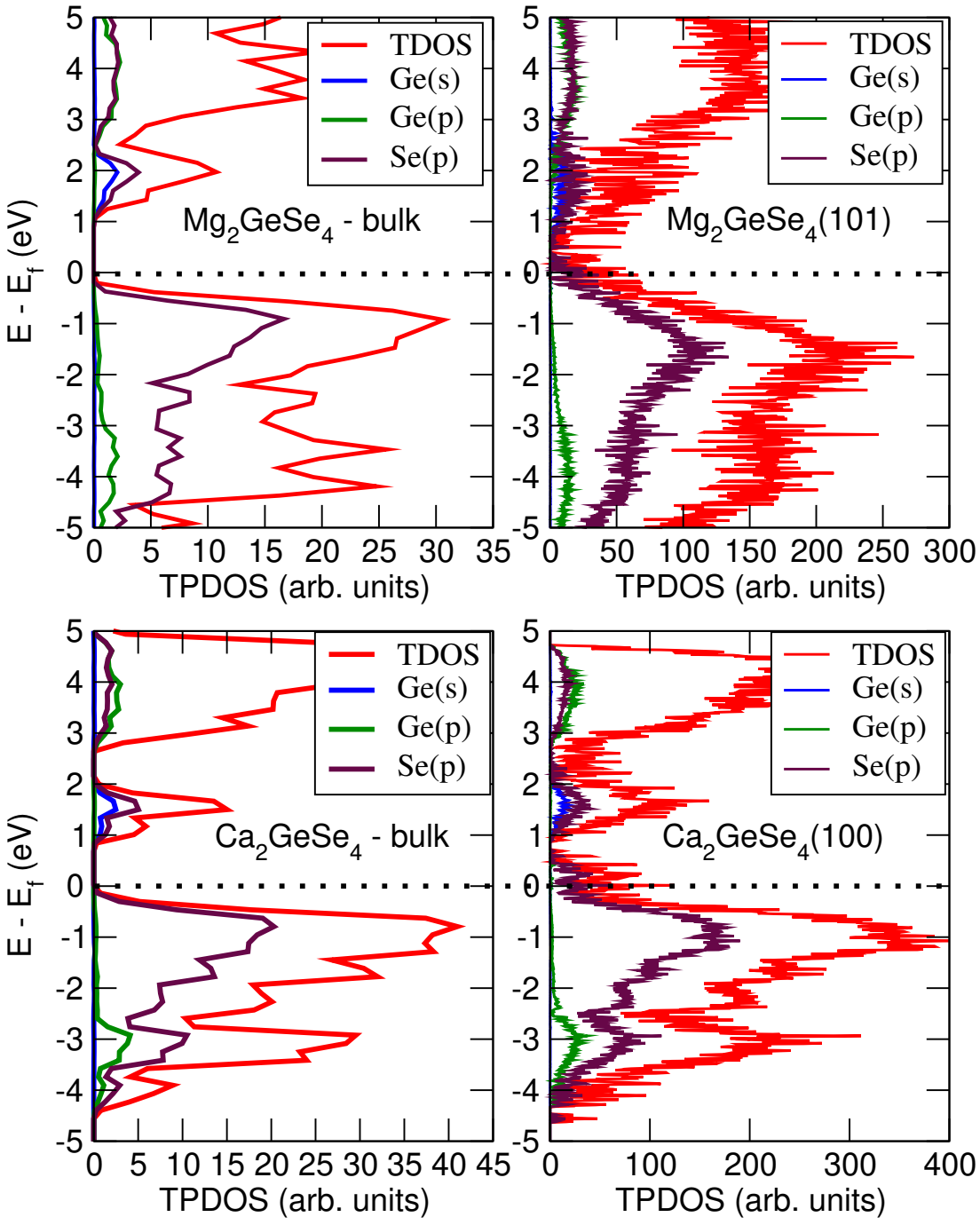

Figure 4.22: Calculated electronic density of state (EDOS) using PBEsol of bulk A_2GeSe_4 (A = Mg and Ca) compounds and their surfaces compared.

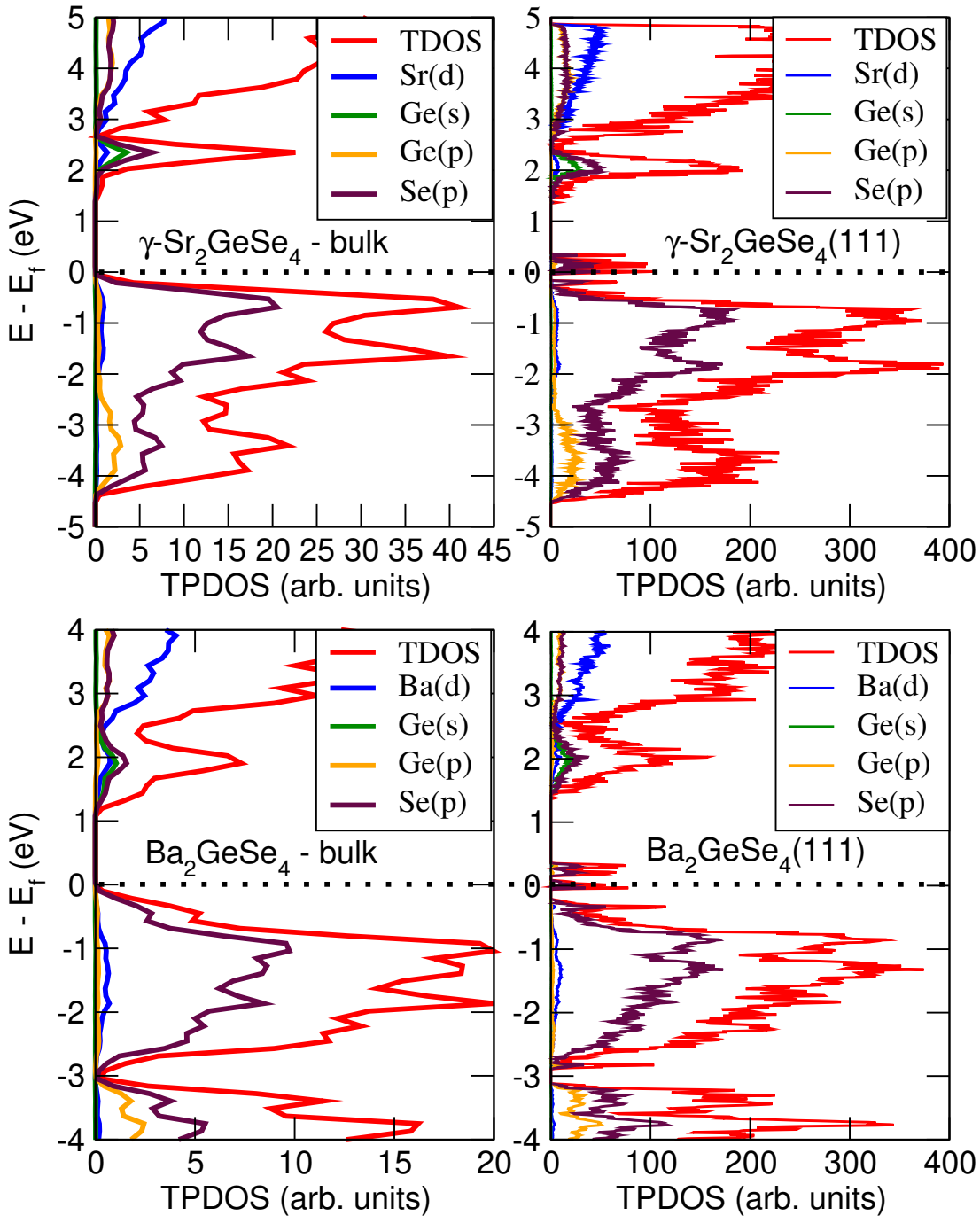

Figure 4.23: Calculated electronic density of state (EDOS) using PBEsol of bulk A_2GeSe_4 (A = γ-Sr and Ba) compounds and their surfaces compared.

electrode, Bader density charge analysis, surface electronic properties and possessing of broad edge of fundamental absorption between 2.05 - 2.86 eV of A_2GeSe_4 (A = Mg, Ca, γ-Sr and Ba) compounds satisfying condition to function as a promising candidate for application in photocatalytic overall water splitting.

5

Summary and future work

5.1 Summary

In this work, we have investigated the structural, mechanical, dynamical, electronic, optical and photocatalytic properties of seleno-germanates A_2GeSe_4 (A = Mg, Ca, γ-Sr and Ba) compound using the first principles calculations. In the first part of this thesis, the density functional theory and many perturbation theory is used to study the ground-state properties and the optical properties of bulk A_2GeSe_4 (A = Mg, Ca, γ-Sr and Ba) compounds. This is to gain an understanding of their stability and suitable applications. In the second part, we study using GGA (PBEsol) the periodic supercell slab of 100, 101, 110 and 111 low index surface orientation of A_2GeSe_4 (A = Mg, Ca, γ-Sr and Ba) compound to investigate the average electrostatic potential, vacuum potential, surface stability, surface energy, charge density distribution, surface electronic properties, valence and conduction band edge positions in order to established a useful informations for photocatalytic application.

The calculated structural parameters from PBE and PBEsol i.e. lattice parameter and the equilibrium volume are comparable to experimental data. The elastic constants satisfy the Born stability criterion for orthorhombic and monoclinic compounds confirming the A_2GeSe_4 compounds mechanical stability. Vibrational properties are calculated using PBEsol for A_2GeSe_4 along the high symmetry kpoints. From the calculated phonon dispersion curves there is no negative frequencies seen which further confirmed the dynamical stability of A_2GeSe_4 compounds. Band structure, the total and projected

density of state (TPDOS) calculation is performed with PBEsol, semi-local modified Becke-Johnson potential, to investigate the electronic properties. The band structure calculated using PBEsol and MBJ are compared. From the band structure analysis, PBEsol underestimated the band gap due to the absence of derived discontinuity and MBJ opens the gaps of studied compounds. From the projected density of state (PDOS) the valence band maximum of A_2GeSe_4 compounds are dominated by contribution of Se(p) states, the conduction band minimum of Mg_2GeSe_4 and Ca_2GeSe_4 is dominated by Se(p) and Ge(s) state, while for γ-Sr_2GeSe_4 and Ba_2GeSe_4 the conduction band minimum is dominated by Sr(d), Se(p) states and hybridization of Ba(d), Ge(s) and Se(p) states respectively. Our calculated electronic structure results suggested that Mg_2GeSe_4 is an indirect band gap, the calculated band gap with modified Becke-Johnson (MBJ), hybrid functional the Heyd-Scuseria-Ernzerhof (HSE06), and quasiparticle G_0W_0+BSE are 11.8%, 26% and 24% greater respectively compared to 2.02 eV measured experimentally. There is no experimental reported gap for Ca_2GeSe_4, γ-Sr_2GeSe_4 and Ba_2GeSe_4, our calculated electronic property i.e. band gaps from hybrid functional MBJ and HSE06 for Ca_2GeSe_4 are 9.0%, 1.7%, γ-Sr_2GeSe_4 are 13.4%, 3.0% and Ba_2GeSe_4 are 5.4%, 10.2% compared to average quasiparticle G_0W_0+BSE band gap respectively.

BSE approximation is successfully applied to determine the optical parameters such as imaginary and real dielectric constants, refractive index, reflectivity, extinction coefficient and energy loss and are analysed. Optical absorption spectra of A_2GeSe_4 results respectively show a significant optical polarization anisotropy in the visible region. Tauc method is employed to evaluate the band gaps from the BSE absorption. Our calculation shows that Mg_2GeSe_4 has 2.60, 2.58, 2.82, Ca_2GeSe_4 has 2.30, 2.37, 2.30, γ-Sr_2GeSe_4 has 2.92, 2.93, 2.86 and Ba_2GeSe_4 has 2.47, 2.05, and 2.66 eV measured band gaps in $a-$, $b-$ and $c-$ direction respectively. The reported optical anisotropy and our calculated BSE band gaps of values between 2.05 - 2.93 eV suggest that A_2GeSe_4 are semiconductors that have the potential to absorb light in the ultraviolet and visible region and can have the promising applications as non-linear optics, photovoltaic (multi-junction solar cell) and photocatalytic materials.

The position of band edges, the valence band maximum E_{VBM} and conduction band minimum E_{CBM} are compared to redox potentials of water, surface properties i.e. average electrostatic potential, vacuum potential, work function, surface energy, charge density distribution and surface electronic property of materials play a significant role in identifying the photocatalytic active materials. Using PBEsol periodic calculation

we carried out detailed studies of photocatalytic properties of A_2GeSe_4 (A = Mg, Ca, γ-Sr and Ba) compound. The periodic supercell slab method was employed to study the 100, 101, 110 and 111 low index surface orientations properties. The band edge E_{VBM} and E_{CBM} positions are calculated using slab model and absolute Mulliken's electronegativity EN model

For the slab model, convergence test of slab thickness and vacuum size are first carried out to identify sufficient slab thickness and vacuum size of 100, 101, 110 and 111 periodic. From the convergence test 9-layer thick periodic surface for orthorhombic A_2GeSe_4 (A = Mg, Ca and γ-Sr) phase, 15-layer periodic surface for monoclinic Ba_2GeSe_4 and 20 - 30 Å vacuum size for both are found sufficient for the calculation. The calculated surface energies for the low index surfaces mention above are for: Mg_2GeSe_4 are 1.53, 1.23, 1.26, 1.29, Ca_2GeSe_4 are 1.83, 3.76, 2.97, 2.79, γ-Sr_2GeSe_4 are 1.68, 1.36, 1.16, 1.00 and Ba_2GeSe_4 are 1.40, 1.78, 2.28 and 0.75 J/m^2 respectively. Our surface energy calculation and Wulff shape plots confirmed Mg_2GeSe_4(101), Ca_2GeSe_4(100), γ-Sr_2GeSe_4(111) and Ba_2GeSe_4(111) surface orientations have smaller surface energy and large surface area. Gibbs concluded that quantity of matter will attain shape with minimal surface energy, thus surface orientation with smaller surface energy will only appear on the Wulff shape and should be considered the most stable surface.

On the more stable surface orientation, average electrostatic potential is calculated and hence vacuum potential energy (E_{vac}) , work function (Φ) and BGC are determined. For slab model we calculated band edge E_{VBM} and E_{CBM} positions using quasiparticle G_0W_0+BSE band gap that is calculated from bulk materials, in combination of the band gap center (BGC). Our calculated band edge position E_{VBM}/E_{CBM} for Mg_2GeSe_4(101), Mg_2GeSe_4(110), Ca_2GeSe_4(100), γ-Sr_2GeSe_4(111) and Ba_2GeSe_4(111) are -6.017/-.437, -6.480/-3.90 -5.794/-3.494, 6.009/-3.149, -4.736/-2.689 eV respectively. This calculated E_{VBM} and E_{CBM} positions are compared to the standard hydrogen electrode (SHE) redox potential. The results show that the orthorhombic A_2GeSe_4 (A = Mg, Ca, γ-Sr) phase has more negative E_{VBM} position than the redox oxidation potential (O_2/H_2) and the E_{CBM} position is more positive than the redox reduction potential (H^+/H_2) both at pH = 0 and 7 respectively. The estimated oxidation and reduction power of Mg_2GeSe_4(101), Mg_2GeSe_4(110), Ca_2GeSe_4(100) and γ-Sr_2GeSe_4(111) are 0.34/0.88, 0.81/1.33, 0.12/0.64, 0.34/0.86 and 1.00/0.59, 0.54/0.13, 0.95/0.54, 1.29/0.88 eV both at pH = 0/7, respectively. Comparison of band edge to the redox potential reveals that A_2GeSe_4 (A = Mg, Ca, γ-Sr) compound are promising photocatalytic materials for the

unassisted overall water-splitting application. For the monoclinic Ba_2GeSe_4 phase, our calculated E_{CBM} position is more positive than the redox reduction potential (H^+/H_2) both at pH = 0 and 7 hence has the reduction redox potential of water. Therefore, according to the slab model calculation Ba_2GeSe_4 can only reduce water but cannot oxidize water, to achieve overall water splitting reaction Ba_2GeSe_4 require external bias potential.

Finally, using the absolute Mulliken's negativity the so-called EN model based on geometrical mean of electronegativity of the constituent atoms of A_2GeSe_4 (A = Mg, Ca, γ-Sr and Ba), we also calculated the valence band maximum E_{VBM} and conduction band minimum E_{CBM}. The band edge positions the E_{VBM} and E_{CBM} are calculated using the calculated bulk quasiparticle G_0W_0+BSE band gap. The calculated E_{VBM} and E_{CBM} positions using EN model for A_2GeSe_4 (A = Mg, Ca, γ-Sr and Ba) are 1.972, 1.056, 1.221, 1.164 and -0.978, -1.474, -1.869 and -1.366 eV respectively. According to our EN model calculation, E_{VBM} and E_{CBM} positions compared to the redox potentials of water versus the normal hydrogen electrode (NHE) reveal that A_2Ge_4 (A = Mg, Ca, γ-Sr and Ba) can straddle the redox potential of water at pH = 7. In comparison, both the slab model and EN model calculated band edge positions show that A_2Ge_4 (A = Mg, Ca, γ-Sr and Ba) that have the potentials to straddle the redox potential for overall water splitting at pH = 7. Due to limited experimental and other theoretical calculated data for this compounds, we are the first to carry out an investigation on the ground state, excited state and photocatalytic properties of A_2Ge_4 (A = Mg, Ca, γ-Sr and Ba) compound. We expect our findings will serve as a contribution to knowledge and open stage for further studies on these compounds.

5.2 Future Work

1. The orthorhombic Ca_2GeSe_4 is a hypothetical compound the ground state properties calculated using PBE and PBEsol reveal that Ca_2GeSe_4 is mechanically and dynamically stable. The calculated cohesive and formation energy suggested that this compound can be formed. Therefore, to compare our calculated ground-state properties require the experimental data.

2. Both slab and EN model calculated band edge position reveals that Ba_2GeSe_4 can only reduce water at pH = 0 or pH = 7 respectively. Therefore, further study is

required on this compound. We suggest that for Ba_2GeSe_4 compound to function for overall water-splitting it requires an external bias. This requires dopping Ba_2GeSe_4 compound with suitable atom or should be combined with another semiconductor that has suitable oxidation potential the so-called heterojunction or Z-scheme. The process which is computationally demanding.

References

[1] Abdu Barde and Daniel P Joubert. Investigation of structural, mechanical, dynamic, electronic and optical properties of seleno-germanates A2GeSe4 (A = Mg, Ca and γ-Sr) from First principles. *Materials Today Communications*, page 100785, 2019.

[2] Hassan Bevrani, Arindam Ghosh, and Gerard Ledwich. Renewable energy sources and frequency regulation: survey and new perspectives. *IET Renewable Power Generation*, 4(5):438–457, 2010.

[3] Hannah E Murdock, Duncan Gibb, Thomas André, Fabiani Appavou, Adam Brown, Bärbel Epp, Bozhil Kondev, Angus McCrone, Evan Musolino, Lea Ranalder, et al. Renewables 2019 Global Status Report. 2019.

[4] Hans-Joachim Lewerenz and Laurie Peter. *Photoelectrochemical water splitting: materials, processes and architectures*. Royal Society of Chemistry, 2013.

[5] Nathan S Lewis and Daniel G Nocera. Powering the planet: Chemical challenges in solar energy utilization. *Proceedings of the National Academy of Sciences*, 103(43):15729–15735, 2006.

[6] Lan Yuan, Chuang Han, Min-Quan Yang, and Yi-Jun Xu. Photocatalytic water splitting for solar hydrogen generation: fundamentals and recent advancements. *International Reviews in Physical Chemistry*, 35(1):1–36, 2016.

[7] Kazuhiko Maeda and Kazunari Domen. Photocatalytic water splitting: Recent progress and future challenges. *The Journal of Physical Chemistry Letters*, 1(18):2655–2661, 2010.

[8] You Xu, Yi Huang, and Bin Zhang. Rational design of semiconductor-based photocatalysts for advanced photocatalytic hydrogen production: The case of cadmium chalcogenides. *Inorganic Chemistry Frontiers*, 3(5):591–615, 2016.

[9] Juan Li, Min Zhang, Qiuye Li, and Jianjun Yang. Enhanced visible light activity on direct contact Z-scheme g-C3N4-TiO2 photocatalyst. *Applied Surface Science*, 391:184–193, 2017.

[10] Yinyi Ma, Xiao Jiang, Rongke Sun, Jianlong Yang, Xiaolin Jiang, Zhanqi Liu, Mingzheng Xie, Erqing Xie, and Weihua Han. Z-scheme Bi2O2. 33/Bi2S3 heterojunction nanostructures for photocatalytic overall water splitting. *Chemical Engineering Journal*, page 123020, 2019.

[11] Srabanti Ghosh. *Visible-Light-Active Photocatalysis: Nanostructured Catalyst Design, Mechanisms, and Applications*. John Wiley & Sons, 2018.

[12] Akira Fujishima and Kenichi Honda. Electrochemical photolysis of water at a semiconductor electrode. *Nature*, 238(5358):37–38, 1972.

[13] Xiaobo Chen, Shaohua Shen, Liejin Guo, and Samuel S Mao. Semiconductor-based photocatalytic hydrogen generation. *Chemical Reviews*, 110(11):6503–6570, 2010.

[14] Kazuhito Hashimoto, Hiroshi Irie, and Akira Fujishima. TiO2 photocatalysis: A historical overview and future prospects. *Japanese Journal of Applied Physics*, 44(12R):8269, 2005.

[15] Rakshit Ameta and Suresh C Ameta. *Photocatalysis: Principles and applications*. CRC Press, 2016.

[16] Rui Liu, Yongjing Lin, Lien-Yang Chou, Stafford W Sheehan, Wangshu He, Fan Zhang, Harvey JM Hou, and Dunwei Wang. Water splitting by tungsten oxide prepared by atomic layer deposition and decorated with an oxygen-evolving catalyst. *Angewandte Chemie International Edition*, 50(2):499–502, 2011.

[17] Kazuhiro Sayama, Atsushi Nomura, Takeo Arai, Tsuyoshi Sugita, Ryu Abe, Masatoshi Yanagida, Takashi O I, Yasukazu Iwasaki, Yoshimoto Abe, and Hideki Sugihara. Photoelectrochemical decomposition of water into H2 and O2 on porous BiVO4 thin-film electrodes under visible light and significant effect of Ag ion treatment. *The Journal of Physical Chemistry B*, 110(23):11352–11360, 2006.

[18] Ilkay Cesar, Andreas Kay, Jose A Gonzalez Martinez, and Michael Grätzel. Translucent thin film Fe2O3 photoanodes for efficient water splitting by sunlight: nanostructure-directing effect of si-doping. *Journal of the American Chemical Society*, 128(14):4582–4583, 2006.

[19] Aron Walsh, Yanfa Yan, Muhammad N Huda, Mowafak M Al-Jassim, and Su-Huai Wei. Band edge electronic structure of BiVO4: elucidating the role of the Bi-s and V-d orbitals. *Chemistry of Materials*, 21(3):547–551, 2009.

[20] Andebet Gedamu Tamirat, John Rick, Amare Aregahegn Dubale, Wei-Nien Su, and Bing-Joe Hwang. Using hematite for photoelectrochemical water splitting: A review of current progress and challenges. *Nanoscale Horizons*, 1(4):243–267, 2016.

[21] Helmut Tributsch. Electrochemical solar cells based on layer-type transition metal compounds: Performance of electrode material. *Solar Energy Materials*, 1(3-4):257–269, 1979.

[22] G Kline, K Kam, D Canfield, and B A Parkinson. Efficient and stable photoelectrochemical cells constructed with WSe2 and MoSe2 photoanodes. *Solar Energy Materials*, 4(3):301–308, 1981.

[23] Chandra Chowdhury, Sharmistha Karmakar, and Ayan Datta. Monolayer group iv–vi monochalcogenides: Low-dimensional materials for photocatalytic water splitting. *The Journal of Physical Chemistry C*, 121(14):7615–7624, 2017.

[24] Xingshuai Lv, Wei Wei, Qilong Sun, Fengping Li, Baibiao Huang, and Ying Dai. Two-dimensional germanium monochalcogenides for photocatalytic water splitting with high carrier mobility. *Applied Catalysis B: Environmental*, 217:275–284, 2017.

[25] Lin Ju, Ying Dai, Wei Wei, Mengmeng Li, and Baibiao Huang. DFT investigation on two-dimensional GeS/WS2 van der waals heterostructure for direct Z-scheme photocatalytic overall water splitting. *Applied Surface Science*, 434:365–374, 2018.

[26] Zhenyu Zhang, Jian Zhang, Tao Wu, Xianhui Bu, and Pingyun Feng. Three-dimensional open framework built from Cu-s icosahedral clusters and its photocatalytic property. *Journal of the American Chemical Society*, 130(46):15238–15239, 2008.

[27] Michelle D Regulacio and Ming-Yong Han. Multinary i-iii-vi2 and i2-ii-iv-vi4 semiconductor nanostructures for photocatalytic applications. *Accounts of Chemical Research*, 49(3):511–519, 2016.

[28] Man-Man Chen, Huai-Guo Xue, and Sheng-Ping Guo. Multinary metal chalcogenides with tetrahedral structures for second-order nonlinear optical, photocatalytic, and photovoltaic applications. *Coordination Chemistry Reviews*, 368:115–133, 2018.

[29] Dengwei Jing, Maochang Liu, Qinyun Chen, and Liejin Guo. Efficient photocatalytic hydrogen production under visible light over a novel W-based ternary chalcogenide photocatalyst prepared by a hydrothermal process. *International Journal of Hydrogen Energy*, 35(16):8521–8527, 2010.

[30] Molin Zhou, Ke Xiao, Xingxing Jiang, Hongwei Huang, Zheshuai Lin, Jiyong Yao, and Yicheng Wu. Visible-light-responsive chalcogenide photocatalyst Ba2ZnSe3: Crystal and electronic structure, thermal, optical, and photocatalytic activity. *Inorganic Chemistry*, 55(24):12783–12790, 2016.

[31] Molin Zhou, Xin Jiang, Xingxing Jiang, Ke Xiao, Yangwu Guo, Hongwei Huang, Zheshuai Lin, Jiyong Yao, Chen-Ho Tung, Li-Zhu Wu, et al. BaAu2S2: A Au-based intrinsic photocatalyst for high-performance visible-light photocatalysis. *Inorganic Chemistry*, 56(9):5173–5181, 2017.

[32] Stefanie Dehnen and Maike Melullis. A coordination chemistry approach towards ternary m/14/16 anions. *Coordination Chemistry Reviews*, 251(9-10):1259–1280, 2007.

[33] Pingyun Feng, Xianhui Bu, and Nanfeng Zheng. The interface chemistry between chalcogenide clusters and open framework chalcogenides. *Accounts of Chemical Research*, 38(4):293–303, 2005.

[34] Eugen Ruzin, Stephan Jakobi, and Stefanie Dehnen. Syntheses, structures and reactivity of novel hydrates of ortho-sulfidostannte salts. *Zeitschrift für Anorganische und Allgemeine Chemie*, 634(6-7):995–1001, 2008.

[35] R Pocha, M Tampier, R-D Hoffmann, B D Mosel, R Pöttgen, and Dirk Johrendt. Crystal structures and properties of the thiostannates Eu2SnS4 and Sr2SnS4 and

the selenogermanate γ-Sr2GeSe4. *Zeitschrift für Anorganische und Allgemeine Chemie*, 629(7-8):1379–1384, 2003.

[36] Abdeljalil Assoud, Navid Soheilnia, and Holger Kleinke. From yellow to black: New semiconducting Ba chalcogeno-germanates. *Zeitschrift für Naturforschung B*, 59(9):975–979, 2004.

[37] Kui Wu, Shilie Pan, and Zhihua Yang. Ba2GeS4 and Mg2SnS4: Synthesis, structures, optical properties and electronic structures. *RSC Advances*, 5(42):33646–33652, 2015.

[38] Kui Wu, Xin Su, Zhihua Yang, and Shilie Pan. An investigation of new infrared nonlinear optical material: BaCdSnSe4, and three new related centrosymmetric compounds: Ba2SnSe4, Mg2GeSe4, and Ba2Ge2S6. *Dalton Transactions*, 44(46):19856–19864, 2015.

[39] Jonathan W Lekse, Meghann A Moreau, Katie L McNerny, Jeongho Yeon, P Shiv Halasyamani, and Jennifer A Aitken. Second-harmonic generation and crystal structure of the diamond-like semiconductors Li2CdGeS4 and Li2CdSnS4. *Inorganic Chemistry*, 48(16):7516–7518, 2009.

[40] Michael Schaefer, Ralph Staehler, Wolff-Ragnar Kiebach, Christian Naether, and Wolfgang Bensch. Four new thioantimonates (iii) with the general formula [TM (tren)] Sb4S7 (TM = Mn, Fe, Co, Zn) with the transition metal as part of a thioantimonate (iii) network synthesized under solvothermal conditions and tuning of the optical band gap by the transition metal cation. *Zeitschrift für Anorganische und Allgemeine Chemie*, 630(12):1816–1822, 2004.

[41] Zhiqun Lin, Meidan Ye, and Mengye Wang. *Multifunctional Photocatalytic Materials for Energy*. Woodhead Publishing, 2018.

[42] Amy L Linsebigler, Guangquan Lu, and John T Yates Jr. Photocatalysis on TiO2 surfaces: Principles, mechanisms, and selected results. *Chemical Reviews*, 95(3):735–758, 1995.

[43] Heinz Gerischer. Photocatalysis in aqueous solution with small TiO2 particles and the dependence of the quantum yield on particle size and light intensity. *Electrochimica Acta*, 40(10):1277–1281, 1995.

[44] Pankaj Chowdhury, Ghodsieh Malekshoar, and Ajay K Ray. Dye-sensitized photocatalytic water splitting and sacrificial hydrogen generation: Current status and future prospects. *Inorganics*, 5(2):34, 2017.

[45] Akihiko Kudo and Yugo Miseki. Heterogeneous photocatalyst materials for water splitting. *Chemical Society Reviews*, 38(1):253–278, 2009.

[46] William S Sheldrick and Michael Wachhold. Chalcogenidometalates of the heavier group 14 and 15 elements. *Coordination Chemistry Reviews*, 176(1):211–322, 1998.

[47] Eugen Ruzin, Christian Zimmermann, Pierre Hillebrecht, and Stefanie Dehnen. Syntheses and structures of solvated tetrasodiumtetrachalcogenostannates [Na4 (en) 4][Sne4](en= 1, 2-diaminoethane; e= Te, Se), and their reactions toward further ternary or quaternary chalcogenometallates [Mn (en) 3] 2 [Sn2Te6]· 4H2O or [Na10 (H2O) 34][Mn4 (μ4-Se)(SnSe4) 4]. *Zeitschrift für Anorganische und Allgemeine Chemie*, 633(5-6):820–829, 2007.

[48] R L Bedard, S T Wilson, L D Vail, JM Bennett, and E M Flanigen. The next generation: synthesis, characterization, and structure of metal sulfide-based microporous solids. In *Studies in Surface Science and Catalysis*, volume 49, pages 375–387. Elsevier, 1989.

[49] Bernt Krebs. Thio-and seleno-compounds of main group elementsnovel inorganic oligomers and polymers. *Angewandte Chemie International Edition in English*, 22(2):113–134, 1983.

[50] K Susa and H Steinfink. Ternary sulfide compounds AB2S4: The crystal structures of GePb2S4 and SnBa2S4. *Journal of Solid State Chemistry*, 3(1):75–82, 1971.

[51] A-M Lamarche, G Lamarche, C Church, J C Woolley, I Ph Swainson, and T M Holden. Neutron diffraction study of magnetic phases in polycrystalline Mn2SiS4. *Journal of Magnetism and Magnetic materials*, 137(3):305–312, 1994.

[52] Mariette Hellenbrandt. The inorganic crystal structure database (ICSD)present and future. *Crystallography Reviews*, 10(1):17–22, 2004.

[53] G Rocktäschel, W Ritter, and Armin Weiss. Ternäre Chalkogenide mit Elementen der4. Hauptgruppe und Olivinstruktur. *Zeitschrift für Naturforschung B*, 19(10):958–958, 1964.

[54] Efthimios Kaxiras. *Atomic and electronic structure of solids*. Cambridge University Press, 2003.

[55] Pierre Hohenberg and Walter Kohn. Inhomogeneous electron gas. *Physical Review*, 136(3B):B864, 1964.

[56] Walter Kohn and Lu Jeu Sham. Self-consistent equations including exchange and correlation effects. *Physical Review*, 140(4A):A1133, 1965.

[57] Richard M Martin. *Electronic structure: Basic theory and practical methods*. Cambridge University Press, 2004.

[58] Max Born and Robert Oppenheimer. Zur quantentheorie der molekeln. *Annalen der Physik*, 389(20):457–484, 1927.

[59] John C Inkson. *Many-body theory of solids: An introduction*. Springer Science & Business Media, 2012.

[60] Llewellyn H Thomas. The calculation of atomic fields. In *Mathematical Proceedings of the Cambridge Philosophical Society*, volume 23, pages 542–548. Cambridge University Press, 1927.

[61] Enrico Fermi. A statistical method for determining some properties of the atom and their application to the theory of the periodic system of the elements. *Journal of Physics*, 48(1-2):73–79, 1928.

[62] Paul A M Dirac. Note on exchange phenomena in the thomas atom. In *Mathematical Proceedings of the Cambridge Philosophical Society*, volume 26, pages 376–385. Cambridge University Press, 1930.

[63] Jorge Kohanoff. *Electronic structure calculations for solids and molecules: theory and computational methods*. Cambridge University Press, 2006.

[64] Mel Levy. Universal variational functionals of electron densities, first-order density matrices, and natural spin-orbitals and solution of the v-representability problem. *Proceedings of the National Academy of Sciences*, 76(12):6062–6065, 1979.

[65] Elliott H Lieb. Density Functionals for coulomb systems. In *Inequalities*, pages 269–303. Springer, 2002.

[66] John P Perdew and Karla Schmidt. Jacobs ladder of Density Functional Approximations for the exchange-correlation energy. In *AIP Conference Proceedings*, volume 577, pages 1–20. AIP, 2001.

[67] John P Perdew, Adrienn Ruzsinszky, Jianmin Tao, Viktor N Staroverov, Gustavo E Scuseria, and Gábor I Csonka. Prescription for the design and selection of Density Functional Approximations: More constraint satisfaction with fewer fits. *The Journal of Chemical Physics*, 123(6):062201, 2005.

[68] David C Langreth and M J Mehl. Beyond the Local-Density Approximation in calculations of Ground-state electronic properties. *Physical Review B*, 28(4):1809, 1983.

[69] John P Perdew, Kieron Burke, and Matthias Ernzerhof. Generalized Gradient Approximation made simple. *Physical Review Letters*, 77(18):3865, 1996.

[70] John P Perdew, Adrienn Ruzsinszky, Gábor I Csonka, Oleg A Vydrov, Gustavo E Scuseria, Lucian A Constantin, Xiaolan Zhou, and Kieron Burke. Restoring the Density-Gradient expansion for exchange in solids and surfaces. *Physical Review Letters*, 100(13):136406, 2008.

[71] John P Perdew and Yue Wang. Accurate and simple analytic representation of the electron-gas correlation energy. *Physical Review B*, 45(23):13244, 1992.

[72] John P Perdew, Stefan Kurth, Aleš Zupan, and Peter Blaha. Accurate Density Functional with correct formal properties: A step beyond the Generalized Gradient Approximation. *Physical Review Letters*, 82(12):2544, 1999.

[73] Jianmin Tao, John P Perdew, Viktor N Staroverov, and Gustavo E Scuseria. Climbing the Density Functional ladder: Nonempirical Meta–Generalized Gradient Approximation designed for molecules and solids. *Physical Review Letters*, 91(14):146401, 2003.

[74] Jürgen Gräfenstein, Dmitry Izotov, and Dieter Cremer. Avoiding singularity problems associated with Meta-GGA (Generalized Gradient Approximation) exchange and correlation functionals containing the kinetic energy density. *The Journal of Chemical Physics*, 127(21):214103, 2007.

[75] Yan Zhao and Donald G Truhlar. A new Local Density Functional for main-group thermochemistry, transition metal bonding, thermochemical kinetics, and noncovalent interactions. *The Journal of Chemical Physics*, 125(19):194101, 2006.

[76] Fabien Tran and Peter Blaha. Accurate band gaps of semiconductors and insulators with a semilocal exchange-correlation potential. *Physical Review Letters*, 102(22):226401, 2009.

[77] Axel D Becke. A new mixing of Hartree–Fock and Local Density-Functional theories. *The Journal of Chemical Physics*, 98(2):1372–1377, 1993.

[78] Stefano Baroni and Eda Tuncel. Exact-exchange extension of the Local-Spin-Density Approximation in atoms: Calculation of total energies and electron affinities. *The Journal of Chemical Physics*, 79(12):6140–6144, 1983.

[79] Andreas Görling and Mel Levy. Hybrid schemes combining the Hartree–Fock method and Density-Functional Theory: Underlying formalism and properties of correlation functionals. *The Journal of Chemical Physics*, 106(7):2675–2680, 1997.

[80] Philip J Stephens, F J Devlin, C F N Chabalowski, and Michael J Frisch. Ab initio calculation of vibrational absorption and circular dichroism spectra using Density Functional force fields. *The Journal of Physical Chemistry*, 98(45):11623–11627, 1994.

[81] Carlo Adamo and Vincenzo Barone. Toward reliable Density Functional methods without adjustable parameters: The PBE0 model. *The Journal of Chemical Physics*, 110(13):6158–6170, 1999.

[82] Jochen Heyd, Gustavo E Scuseria, and Matthias Ernzerhof. Hybrid Functionals based on a screened coulomb potential. *The Journal of Chemical Physics*, 118(18):8207–8215, 2003.

[83] Georg Kresse and Jürgen Furthmüller. Efficiency of Ab-initio total energy calculations for metals and semiconductors using a plane-wave basis set. *Computational Materials Science*, 6(1):15–50, 1996.

[84] Georg Kresse and Jürgen Hafner. Ab initio molecular dynamics for liquid metals. *Physical Review B*, 47(1):558, 1993.

[85] N W Ashcroft and N D Mermin. Solid State Physics Saunders College Publishing. *Fort Worth*, 1976.

[86] Mike C Payne, Michael P Teter, Douglas C Allan, T A Arias, and ad J D Joannopoulos. Iterative minimization techniques for Ab initio total-energy calculations: Molecular Dynamics and Conjugate Gradients. *Reviews of Modern Physics*, 64(4):1045, 1992.

[87] Jürgen Hafner. Ab-Initio simulations of materials using VASP: Density-Functional Theory and beyond. *Journal of Computational Chemistry*, 29(13):2044–2078, 2008.

[88] James C Phillips and Leonard Kleinman. New method for calculating wave functions in crystals and molecules. *Physical Review*, 116(2):287, 1959.

[89] D R Hamann, M Schlüter, and C Chiang. Norm-Conserving Pseudopotentials. *Physical Review Letters*, 43(20):1494, 1979.

[90] Norman Troullier and José Luís Martins. Efficient Pseudopotentials for plane-wave calculations. *Physical Review B*, 43(3):1993, 1991.

[91] David Vanderbilt. Soft self-consistent Pseudopotentials in a generalized eigenvalue formalism. *Physical Review B*, 41(11):7892, 1990.

[92] E G Moroni, G Kresse, J Hafner, and J Furthmüller. Ultrasoft Pseudopotentials applied to magnetic Fe, Co, and Ni: From atoms to solids. *Physical Review B*, 56(24):15629, 1997.

[93] Robert O Jones and Olle Gunnarsson. The Density Functional formalism, its applications and prospects. *Reviews of Modern Physics*, 61(3):689, 1989.

[94] Ferdi Aryasetiawan and Olle Gunnarsson. The GW method. *Reports on Progress in Physics*, 61(3):237, 1998.

[95] M Shishkin and G Kresse. Implementation and performance of the frequency-dependent GW method within the PAW framework. *Physical Review B*, 74(3):035101, 2006.

[96] Mark S Hybertsen and Steven G Louie. Electron correlation in semiconductors and insulators: Band gaps and quasiparticle energies. *Physical Review B*, 34(8):5390, 1986.

[97] Lars Hedin. New method for calculating the one-particle Green's Function with application to the electron-gas problem. *Physical Review*, 139(3A):A796, 1965.

[98] Christoph Friedrich and Arno Schindlmayr. Many-Body Perturbation Theory: The GW Approximation. *NIC Series*, 31:335, 2006.

[99] Jozef T Devreese and Fons Brosens. *Electron correlations in solids, molecules, and atoms*, volume 81. Springer Science & Business Media, 2012.

[100] Wilfried G Aulbur, Lars Jönsson, and John W Wilkins. Quasiparticle calculations in solids. *Solid State Physics*, 54:1–218, 2000.

[101] A L Fetter. J D Walecka Quantum Theory of Many-Particles Systems, 1971.

[102] Giovanni Onida, Lucia Reining, and Angel Rubio. Electronic excitations: Density-Functional versus Many-Body Greens-Function Approaches. *Reviews of Modern Physics*, 74(2):601, 2002.

[103] Lucia Reining. 10 Linear response and more: The Bethe-Salpeter Equation. *Quantum Materials: Experiments and Theory*.

[104] M J Van Setten, R Gremaud, G Brocks, B Dam, G Kresse, and G A De Wijs. Optical response of the sodium alanate system: GW0-BSE calculations and thin film measurements. *Physical Review B*, 83(3):035422, 2011.

[105] F K Schulte. On the theory of the work function. *Zeitschrift für Physik B Condensed Matter*, 27(4):303–307, 1977.

[106] Josef Hölzl, Franz K Schulte, and Heribert Wagner. *Solid Surface Physics*, volume 85. Springer, 2006.

[107] ND Lang and W Kohn. Theory of metal surfaces: Work function. *Physical Review B*, 3(4):1215, 1971.

[108] PW Tasker. The stability of ionic crystal surfaces. *Journal of Physics C: Solid State Physics*, 12(22):4977, 1979.

[109] Lennart Bengtsson. Dipole correction for surface supercell calculations. *Physical Review B*, 59(19):12301, 1999.

[110] Jörg Neugebauer and Matthias Scheffler. Adsorbate-substrate and adsorbate-adsorbate interactions of Na and K adlayers on Al (111). *Physical Review B*, 46(24):16067, 1992.

[111] Richard F W Bader. Atoms in molecules. *Accounts of Chemical Research*, 18(1):9–15, 1985.

[112] Georg Kresse and Jürgen Furthmüller. Efficient iterative schemes for Ab Initio total-energy calculations using a plane-wave basis set. *Physical Review B*, 54(16):11169, 1996.

[113] Peter E Blöchl. Projector Augmented-Wave method. *Physical Review B*, 50(24):17953, 1994.

[114] Georg Kresse and Daniel Joubert. From Ultrasoft Pseudopotentials to the Projector Augmented-Wave method. *Physical Review B*, 59(3):1758, 1999.

[115] Setyawan Wahyu and Stefano Curtarolo. High-throughput electronic band structure calculations: Challenges and tools. *Computational Materials Science*, 49(2):299–312, 2010.

[116] Maytal Caspary Toroker, Dalal K Kanan, Nima Alidoust, Leah Y Isseroff, Peilin Liao, and Emily A Carter. First principles scheme to evaluate band edge positions in potential transition metal oxide photocatalysts and photoelectrodes. *Physical Chemistry Chemical Physics*, 13(37):16644–16654, 2011.

[117] Robert S Mulliken. A new electroaffinity scale; together with data on valence states and on valence ionization potentials and electron affinities. *The Journal of Chemical Physics*, 2(11):782–793, 1934.

[118] M A Butler and D S Ginley. Prediction of flatband potentials at semiconductor-electrolyte interfaces from atomic electronegativities. *Journal of the Electrochemical Society*, 125(2):228–232, 1978.

[119] Yong Xu and Martin A A Schoonen. The absolute energy positions of conduction and valence bands of selected semiconducting minerals. *American Mineralogist*, 85(3-4):543–556, 2000.

[120] S M Hosseini, Tayebeh Movlarooy, and Ahmad Kompany. First-Principle calculations of the cohesive energy and the electronic properties of PbTiO3. *Physica B: Condensed Matter*, 391(2):316–321, 2007.

[121] C T Zhou, B Xiao, J Feng, JC Chen, R Zhou, JD Xing, and YF Li. The stability and elastic constants of X2Ni3Si (X = Ti, Mo and W): The novel ternary metal silicides. *Physica B: Condensed Matter*, 404(12-13):1701–1704, 2009.

[122] Håkan W Hugosson, Pavel Korzhavyi, Ulf Jansson, Börje Johansson, and Olle Eriksson. Phase stabilities and structural relaxations in substoichiometric TiC 1-X. *Physical Review B*, 63(16):165116, 2001.

[123] Yong-Hua Duan, Yong Sun, Ming-Jun Peng, and Zhong-Zheng Guo. First Principles investigation of the binary intermetallics in Pb–Mg–Al alloy: stability, elastic properties and electronic structure. *Solid State Sciences*, 13(2):455–459, 2011.

[124] Mohammed Suleiman Hussein Suleiman. *A theoretical Investigation of Structural, Electronic and Optical Properties of some Group 10, 11 and 12 Transition-Metal Nitrides*. PhD Thesis, 2014.

[125] Eunja Kim and Changfeng Chen. Calculation of bulk modulus for highly anisotropic materials. *Physics Letters A*, 326(5-6):442–448, 2004.

[126] Pascal Vinet, James H Rose, John Ferrante, and John R Smith. Universal features of the equation of state of solids. *Journal of Physics: Condensed Matter*, 1(11):1941, 1989.

[127] Pascal Vinet, John R Smith, John Ferrante, and James H Rose. Temperature effects on the universal equation of state of solids. *Physical Review B*, 35(4):1945, 1987.

[128] Francis Birch. Finite elastic strain of cubic crystals. *Physical Review*, 71(11):809, 1947.

[129] Raymond Jeanloz. Universal equation of state. *Physical Review B*, 38(1):805, 1988.

[130] Mahmud Abdulsalam. *A Theoretical Investigation of the Structural, Electronic and Optical Properties of Transition Metal Chalcogenides*. PhD Thesis, 2015.

[131] Max Born. On the stability of crystal lattices. i. In *Mathematical Proceedings of the Cambridge Philosophical Society*, volume 36, pages 160–172. Cambridge University Press, 1940.

[132] Félix Mouhat and François-Xavier Coudert. Necessary and sufficient elastic stability conditions in various crystal systems. *Physical Review B*, 90(22):224104, 2014.

[133] Hillard Bell Huntington. The Elastic Constants of Crystals. In *Solid State Physics*, volume 7, pages 213–351. Elsevier, 1958.

[134] Max Born and Kun Huang. *Dynamical Theory of Crystal Lattices*. Clarendon Press, 1954.

[135] Zhi-jian Wu, Er-jun Zhao, Hong-ping Xiang, Xian-feng Hao, Xiao-juan Liu, and Jian Meng. Crystal structures and elastic properties of superhard IrN2 and IrN3 from First Principles. *Physical Review B*, 76(5):054115, 2007.

[136] W Voigt. A determination of the elastic constants for beta-quartz lehrbuch de kristallphysik. *Terubner Leipzig*, 40:2856–2860, 1928.

[137] András Reuß. Berechnung der fließgrenze von mischkristallen auf grund der plastizitätsbedingung für einkristalle. *ZAMM-Journal of Applied Mathematics and Mechanics/Zeitschrift für Angewandte Mathematik und Mechanik*, 9(1):49–58, 1929.

[138] Richard Hill. The elastic behaviour of a crystalline aggregate. *Proceedings of the Physical Society. Section A*, 65(5):349, 1952.

[139] P Ravindran, Lars Fast, P A_ Korzhavyi, B Johansson, J Wills, and O Eriksson. Density Functional Theory for calculation of elastic properties of orthorhombic crystals: Application to TiSi2. *Journal of Applied Physics*, 84(9):4891–4904, 1998.

[140] Damien Connétable and Olivier Thomas. First-Principles study of the structural, electronic, vibrational, and elastic properties of orthorhombic NiSi. *Physical Review B*, 79(9):094101, 2009.

[141] D H Chung and W R Buessem. The elastic anisotropy of crystals. *Journal of Applied Physics*, 38(5):2010–2012, 1967.

[142] Clarence Zener. *Elasticity and anelasticity of metals*. University of Chicago Press, 1948.

[143] Shivakumar I Ranganathan and Martin Ostoja-Starzewski. Universal elastic anisotropy index. *Physical Review Letters*, 101(5):055504, 2008.

[144] G Kresse, J Furthmüller, and J Hafner. Ab initio force constant approach to phonon dispersion relations of diamond and graphite. *EPL (Europhysics Letters)*, 32(9):729, 1995.

[145] Atsushi Togo and Isao Tanaka. First principles phonon calculations in materials science. *Scripta Materialia*, 108:1–5, 2015.

[146] Atsushi Togo. Phonopy v. 1.8. 5. *Avaliable: http://phonopy. sourceforge. net*, 2009.

[147] Leah Isseroff Bendavid and Emily A Carter. First-Principles predictions of the structure, stability, and photocatalytic potential of Cu2O surfaces. *The Journal of Physical Chemistry B*, 117(49):15750–15760, 2013.

[148] Suklyun Hong and MH Yoo. Surface energy anisotropy of fept nanoparticles. *Journal of Applied Physics*, 97(8):084315, 2005.

[149] E Ringe, Richard P Van Duyne, and LD Marks. Wulff construction for alloy nanoparticles. *Nano Letters*, 11(8):3399–3403, 2011.

[150] Simone Piccinin, Spiros Zafeiratos, Catherine Stampfl, Thomas W Hansen, Michael Hävecker, Detre Teschner, Valerii I Bukhtiyarov, Frank Girgsdies, Axel Knop-Gericke, Robert Schlögl, et al. Alloy catalyst in a reactive environment: The example of Ag-Cu particles for ethylene epoxidation. *Physical Review Letters*, 104(3):035503, 2010.

[151] David Sholl and Janice A Steckel. *Density Functional Theory: A practical introduction*. John Wiley & Sons, 2011.

[152] Léon Van Hove. The occurrence of singularities in the elastic frequency distribution of a crystal. *Physical Review*, 89(6):1189, 1953.

[153] Hendrik J Monkhorst. Hartree-Fock Density of States for extended systems. *Physical Review B*, 20(4):1504, 1979.

[154] W Hanke and LJ Sham. Many-particle effects in the optical spectrum of a semiconductor. *Physical Review B*, 21(10):4656, 1980.

[155] Edwin E Salpeter and Hans Albrecht Bethe. A relativistic equation for bound-state problems. *Physical Review*, 84(6):1232, 1951.

[156] Michael M Broido and John G Taylor. Bethe-Salpeter Equation. *Journal of Mathematical Physics*, 10(1):184–209, 1969.

[157] John Bechhoefer. Kramers–Kronig, Bode, and the meaning of zero. *American Journal of Physics*, 79(10):1053–1059, 2011.

[158] Mark Fox. Optical properties of solids, 2002.

[159] F D Murnaghan. The compressibility of media under extreme pressures. *Proceedings of the National Academy of Sciences of the United States of America*, 30(9):244, 1944.

[160] H Gercek. Poisson's ratio values for rocks. *International Journal of Rock Mechanics and Mining Sciences*, 44(1):1–13, 2007.

[161] Augustus Edward Hough Love. *A treatise on the mathematical theory of elasticity*. Cambridge University Press, 2013.

[162] S F Pugh. Xcii. Relations between the elastic moduli and the plastic properties of polycrystalline pure metals. *The London, Edinburgh, and Dublin Philosophical Magazine and Journal of Science*, 45(367):823–843, 1954.

[163] John M Ziman. *Electrons and phonons: The theory of transport phenomena in solids*. Oxford University Press, 2001.

[164] Atsushi Togo, Laurent Chaput, Isao Tanaka, and Gilles Hug. First-principles phonon calculations of thermal expansion in Ti3SiC2, Ti3AlC2, and Ti3GeC2. *Physical Review B*, 81(17):174301, 2010.

[165] John P Perdew and Mel Levy. Physical content of the exact Kohn-Sham orbital energies: Band gaps and derivative discontinuities. *Physical Review Letters*, 51(20):1884, 1983.

[166] Lu J Sham and Michael Schlüter. Density-Functional Theory of the energy gap. *Physical Review Letters*, 51(20):1888, 1983.

[167] Wilfried G Aulbur, Martin Städele, and Andreas Görling. Exact-exchange-based quasiparticle calculations. *Physical Review B*, 62(11):7121, 2000.

[168] Andrzej Fleszar. LDA, GW, and exact-exchange Kohn-Sham scheme calculations of the electronic structure of sp semiconductors. *Physical Review B*, 64(24):245204, 2001.

[169] Bengt Holm and Ulf von Barth. Fully self-consistent GW self-energy of the electron gas. *Physical Review B*, 57(4):2108, 1998.

[170] Wolf-Dieter Schöne and Adolfo G Eguiluz. Self-consistent calculations of quasiparticle states in metals and semiconductors. *Physical Review Letters*, 81(8):1662, 1998.

[171] Jochen Heyd and Gustavo E Scuseria. Efficient Hybrid Density Functional calculations in solids: Assessment of the Heyd–Scuseria–Ernzerhof screened coulomb hybrid functional. *The Journal of Chemical Physics*, 121(3):1187–1192, 2004.

[172] Claudia Ambrosch-Draxl and Jorge O Sofo. Linear optical properties of solids within the full-potential linearized augmented planewave method. *Computer Physics Communications*, 175(1):1–14, 2006.

[173] David R Penn. Wave-number-dependent dielectric function of semiconductors. *Physical Review*, 128(5):2093, 1962.

[174] J Tauc, Radu Grigorovici, and Anina Vancu. Optical properties and electronic structure of amorphous germanium. *Physica Status Solidi (B)*, 15(2):627–637, 1966.

[175] D M Bird, L J Clarke, R D King-Smith, M C Payne, I Stich, and A P Sutton. First principles calculation of the structure and energy of Si (113). *Physical Review Letters*, 69(26):3785, 1992.

[176] Robert W Balluffi, Sam Allen, and W Craig Carter. *Kinetics of materials*. John Wiley & Sons, 2005.

[177] Richard Tran, Zihan Xu, Balachandran Radhakrishnan, Donald Winston, Wenhao Sun, Kristin A Persson, and Shyue Ping Ong. Surface energies of elemental crystals. *Scientific Data*, 3:160080, 2016.

[178] K M Ho and K P Bohnen. Investigation of multilayer relaxation on Al (110) with the use of self-consistent total-energy calculations. *Physical Review B*, 32(6):3446, 1985.

[179] A Kiejna, J Peisert, and P Scharoch. Quantum-size effect in thin Al (110) slabs. *Surface science*, 432(1-2):54–60, 1999.

[180] Vincenzo Fiorentini and Michael Methfessel. Extracting convergent surface energies from slab calculations. *Journal of Physics: Condensed Matter*, 8(36):6525, 1996.

[181] R Edwin García and John Blendell. Equilibrium Wulff Shape Generator. 2012.

[182] Andrew R Roosen, Ryan P McCormack, and W Craig Carter. Wulffman: A tool for the calculation and display of crystal shapes. *Computational Materials Science*, 11(1):16–26, 1998.

[183] Yi-Fa Qin and Shao-Qing Wang. Ab-initio study of the role of Mg2Si and Al2CuMg phases in electrochemical corrosion of Al alloys. *Journal of The Electrochemical Society*, 162(9):C503–C508, 2015.

[184] Zhi-Hao Cui and Hong Jiang. Theoretical investigation of Ta2O5, TaON, and Ta3N5: electronic band structures and absolute band edges. *The Journal of Physical Chemistry C*, 121(6):3241–3251, 2017.

[185] Hong Jiang. Electronic band structures of molybdenum and tungsten dichalcogenides by the GW Approach. *The Journal of Physical Chemistry C*, 116(14):7664–7671, 2012.

[186] Arthur H Nethercot Jr. Prediction of fermi energies and photoelectric thresholds based on electronegativity concepts. *Physical Review Letters*, 33(18):1088, 1974.

[187] Arthur J Nozik. Photoelectrochemistry: applications to solar energy conversion. *Annual Review of Physical Chemistry*, 29(1):189–222, 1978.

[188] Koichi Momma and Fujio Izumi. VESTA3 for three-dimensional visualization of crystal, volumetric and morphology data. *Journal of Applied Crystallography*, 44(6):1272–1276, 2011.

[189] Joseph Simfukwe, Refilwe Edwin Mapasha, Artur Braun, and Mmantsae Diale. Density Functional theory study of Cu doped {0001} and {0112} Surfaces of hematite for water splitting. 2018.

[190] Georgios A Tritsaris, Brad D Malone, and Efthimios Kaxiras. Structural stability and electronic properties of low-index surfaces of SnS. *Journal of Applied Physics*, 115(17):173702, 2014.

[191] Verónica Vildosola, Francisco Güller, and Ana María Llois. Mechanism to generate a two-dimensional electron gas at the surface of the charge-ordered semiconductor BaBiO3. *Physical Review Letters*, 110(20):206805, 2013.

[192] Yuhua Duan. Electronic properties and stabilities of bulk and low-index surfaces of SnO in comparison with SnO2: A First-Principles Density Functional Approach with an empirical correction of van der waals interactions. *Physical Review B*, 77(4):045332, 2008.

[193] Atashi B Mukhopadhyay, Javier F Sanz, and Charles B Musgrave. First-principles calculations of structural and electronic properties of monoclinic hafnia surfaces. *Physical Review B*, 73(11):115330, 2006.